Structural Friction Anisotropy on the Nanometer Scale

Inauguraldissertation

zur

Erlangung der Würde eines Doktors der Philosophie
vorgelegt der
Philosophisch-Naturwissenschaftlichen Fakultät
der Universität Basel
von

Gregor Fessler

aus Hitzkirch, LU

UNI
BASEL

Basel, 2013

Genehmigt von der Philosophisch-Naturwissenschaftlichen Fakultät

auf Antrag von:

Prof. Dr. Ernst Meyer
Prof. Dr. Martino Poggio

Basel, den 15. Oktober 2013

Prof. Dr. Jörg Schibler
Dekan

creative commons

Namensnennung-Keine kommerzielle Nutzung-Keine Bearbeitung 2.5 Schweiz

---

Sie dürfen:

das Werk vervielfältigen, verbreiten und öffentlich zugänglich machen

Zu den folgenden Bedingungen:

Namensnennung. Sie müssen den Namen des Autors/Rechteinhabers in der von ihm festgelegten Weise nennen (wodurch aber nicht der Eindruck entstehen darf, Sie oder die Nutzung des Werkes durch Sie würden entlohnt).

Keine kommerzielle Nutzung. Dieses Werk darf nicht für kommerzielle Zwecke verwendet werden.

Keine Bearbeitung. Dieses Werk darf nicht bearbeitet oder in anderer Weise verändert werden.

- Im Falle einer Verbreitung müssen Sie anderen die Lizenzbedingungen, unter welche dieses Werk fällt, mitteilen. Am Einfachsten ist es, einen Link auf diese Seite einzubinden.

- Jede der vorgenannten Bedingungen kann aufgehoben werden, sofern Sie die Einwilligung des Rechteinhabers dazu erhalten.
- Diese Lizenz lässt die Urheberpersönlichkeitsrechte unberührt.

Die gesetzlichen Schranken des Urheberrechts bleiben hiervon unberührt.

Die Commons Deed ist eine Zusammenfassung des Lizenzvertrags in allgemeinverständlicher Sprache: http://creativecommons.org/licenses/by-nc-nd/2.5/ch/legalcode.de

Haftungsausschluss:
Die Commons Deed ist kein Lizenzvertrag. Sie ist lediglich ein Referenztext, der den zugrundeliegenden Lizenzvertrag übersichtlich und in allgemeinverständlicher Sprache wiedergibt. Die Deed selbst entfaltet keine juristische Wirkung und erscheint im eigentlichen Lizenzvertrag nicht. Creative Commons ist keine Rechtsanwaltsgesellschaft und leistet keine Rechtsberatung. Die Weitergabe und Verlinkung des Commons Deeds führt zu keinem Mandatsverhältnis.

Quelle: http://creativecommons.org/licenses/by-nc-nd/2.5/ch/ Datum: 3.4.2009

Contents

List of Abbreviations

AD	Analog Digital / Digital Analog
AFM	Atomic Force Microscopy
a.u.	Arbitrary Units
BA	Benzylammonium (Molecule)
BNL	Benzylammonium Crystal
bwd	Backward
CAD	Computer-Aided Design
DFT	Density Functional Theory
DMT	Derjaguin-Muller-Toporov
exp	Experiment
FEM	Finite Element Method
FET	Field-Effect Transistor
Fig.	Figure
FM	Frequency Modulated
FPGA	Field Programmable Gate Array
fwd	Forward
FWHM	Full Width at Half Maximum
GND	Ground
HOPG	Highly Ordered Pyrolytic Graphite
HV	High Voltage
IC	Integrated Circuit
IR	Infra-Red
IV converter	Current to Voltage Converter
JKR	Johnson-Kendall-Roberts
KPFM	Kelvin Probe Force Microscopy
nc	Non-contact
NEMS	Nanoelectromechanical System

p-chamber	Preparation Chamber
PLL	Phase-Locked Loop
PT	Prandtl-Tomlinson
QPD	Quadrant Photo Diode
SAM	Self Assembeling Monolayer
sim	Simulation
SLD	Superlum Diode
SPM	Scanning Probe Microscope
STM	Scanning Tunneling Microscopy
TSM	Transversal Shear Microscopy
TSP	Titanium Sublimation Pump
UHV	Ultra-High Vacuum

Abstract

The ability to understand and control friction on an atomic scale is becoming increasingly important, not only considering the increasingly small scale of mechanical systems that are being developed, but also in respect of furthering the fundamental understanding of friction. In this thesis, the friction anisotropy at the atomic level was investigated. This investigation demanded special requirements from the experimental setup, and accordingly, in section 2, a detailed description of a newly developed scanning probe microscope incorporating new electronics and a significantly developed ultra-high vacuum system is given. In particular, with this newly developed microscope, it is possible to use a specially designed sample holder which rotates the sample in situ, enabling the measurement of friction forces along arbitrary directions of the sample surface.

Measurements on NaCl(100), a well known surface in the field of nanotribology, were compared with *Prandtl-Tomlinson* (PT) simulations. Beside the anisotropy investigations, some newly discovered features along the [100] and [110] directions are presented. Three main conclusions can be drawn from these results: the tip path is influencing the average friction force, friction is reduced by 27% on one ionic species (whether it is Na^+ or Cl^- is depending on the tip), and the tip asymmetry is leading to a shift of forward and backward friction force maps along the slow scan direction. In previous studies, the tip-sample interaction in the PT model was well described by a sinusoidal potential. This potential, however, fails to sufficiently describe the present results. New simulations were conducted and are presented, which are based on an ab initio calculated potential using density functional theory, and reproduce the main features of the experimental results well.

Investigations on the organic surface of a benzylammonium crystal have shown that the molecular orientation is influencing friction and producing a friction contrast on a molecular scale. While the experimental results clearly show that the corrugation potential is influenced by the molecular orientation, adequate simulations reproducing this phenomena require a potential which includes the relaxation of the surface and tip in contact. In addition, anisotropy measurements show a strong increase of friction along the [100] orientation.

Friction measurements on patterned pristine and hydrogenated graphene initially revealed a contrast between these two surfaces which are initially covered by a contamination layer. In the course of continuous scanning, a mechanical cleaning occurs. The stability of the contamination layer under mechanical treatment is related to the extent of hydrogenation of the subjacent graphene, the hydrogenated regions require a more intense treatment for cleaning. It is found that on the cleaned surface, friction reduces to approximately a quarter of its value, and, after this mechanical treatment, the friction contrast between graphene and hydrogenated graphene completely disappears. It is concluded therefore that despite the strong effect of the hydrogenation to the electronic properties of graphene, it is not degrading its properties as a lubricant.

> *In the beginning the Universe was created. This has made a lot of people very angry and been widely regarded as a bad move.*
>
> Douglas Adams

Chapter 1

Nanotribology

Tribology, the science of interacting surfaces in relative motion, is a very old scientific topic. The first reported quantitative investigations go back to Leonardo da Vinci who measured static friction of different materials sliding on an inclined plane. His findings were, that friction is depending on the applied normal load but independent of the apparent area of contact [1, 2]. Later, *Guillaume Amonton*, *Leonhard Euler* and *Charles Augustin Coulomb* made important contributions, which lead to the two Amontons' laws and the Coulomb law, concluding that the friction coefficient is proportional to the ratio of friction force to normal force (1^{st} Amontons' law)

$$\mu = F_l/F_n, \tag{1.1}$$

friction is independent of the apparent contact area (2^{nd} Amontons' law), and that kinetic friction is independent of the sliding velocity (Coulomb's law) [3, 4].

On a microscopic scale, however, the situation is described differently. The apparent contact area is in the microscopic view consisting of rough surfaces with asperities that are forming the real contacts. *Bowden* and *Tabor* introduced a new concept, where friction is proportional to the real area of contact $F_l = \sigma A_r$, the proportionality factor σ is called shear strength [5]. The applied normal load is compressing these asperities which is described as $A_r = F_n/p^*$, p^* is called the yield pressure. The result is the same linear relation of friction and normal force as described in eq. (1.1) with $\mu = \sigma/p^*$. Regarding only a single asperity, the elastic deformation can be described by continuum mechanics. A sphere which is pressed against a flat surface can be described using different elasticity models resulting in a relation of $A_r \propto F_n^{2/3}$ which was also seen in experiments [6, 7]. Different descriptions such as the *Hertz* model [8], the *Johnson-Kendall-Roberts* (JKR) [9], the *Derjaguin-Muller-Toporov* (DMT) [10] or *Maugis–Dugdale* model [11] apply to different material combinations.

1.1 The Tomlinson Model

Long before the tools were invented to investigate friction on the nanometer scale, the *Prandtl-Tomlinson* (PT) model was developed [12], describing a single asperity sliding over a surface. In a one dimensional approach, the tip-surface potential $V(x)$ describes the interaction of the asperity with the surface. The asperity is coupled with a spring with the stiffness k to the support, dragging it along the surface. In the quasistatic limit of low velocities, the total energy of the system at the position x is given by

$$V_{tot}(x,t) = V(x) + \frac{1}{2}k(vt - x)^2. \tag{1.2}$$

In the quasi static case, the tip is always at the local energy minimum. We can track the tip movement by following the local minimas which are at

$$\frac{\partial V_{tot}}{\partial x} = \frac{\partial V(x)}{\partial x} + k(vt - x) = 0, \tag{1.3}$$

under the condition that $\frac{\partial^2 V_{tot}}{\partial x^2} > 0$.

Using for example the sinusoidal potential $V(x) = \frac{E_0}{2}\cos(\frac{2\pi x}{a})$ with the periodicity of the surface's lattice a and the amplitude E_0, the tip path can be calculated analytically. The critical position where the tip jumps x^* is reached, when the second derivative is zero $\frac{\partial^2 V_{tot}}{\partial x^2} = 0$ [13], resulting in

$$x^* = \frac{a}{2\pi}\arccos(-\frac{1}{\eta}), \quad \eta = \frac{2\pi^2 E_0}{ka^2}. \tag{1.4}$$

The lateral force is then

$$F^* = \frac{ka}{2\pi}\sqrt{\eta^2 - 1}. \tag{1.5}$$

η describes the relation of the strength of interaction between tip and surface with the stiffness of the system. Therefore the value of η decides if the tip is sliding smoothly over the surface in a superlubric regime ($\eta < 1$) or if there is a stick slip movement ($\eta > 1$) where the tip jumps from one stability position into another [14].

In order to apply this model to generate friction maps as they are measured by means of *friction force microscopy* (FFM), these formalism is extended to a two dimensional system and then, the tip motion can be described with the Langevin equation [15–17]

$$m\frac{d^2x}{dt^2} + m\gamma\frac{dx}{dt} + \frac{\partial V_{tot}(\overrightarrow{r}_{tip}, \overrightarrow{r}_{sup})}{\partial x} = \xi(t), \tag{1.6}$$

$$V_{tot}(\overrightarrow{r}_{tip}, \overrightarrow{r}_{sup}) = V(\overrightarrow{r}_{tip}) + \frac{1}{2}k(|\overrightarrow{r}_{tip} - \overrightarrow{r}_{sup}|)^2, \tag{1.7}$$

where m is the mass of the tip, γ the damping coefficient, ξ a Gaussian distributed random noise representing the Brownian motion at finite temperatures and $\overrightarrow{r}_{tip}$ the tip position and $\overrightarrow{r}_{sup}$ the cantilever support position. The Gaussian noise ξ is generated using the Ermak's algorithm [18, 19].

1.2 Measurements of Friction Anisotropy

Despite the difficulties to measure the friction along different orientations, various articles presented the measurement of friction anisotropy. Different ways for calibrating the lateral forces for FFM exist, but only the direction perpendicular to the lever axis can properly be calibrated and at the same time ensure the separation of normal and lateral forces. As a consequence, the angle dependent measurement of friction can not be performed by just scanning along different directions, but the two coordinate systems of the lever and sample have to be rotated relative to each other. In the experiment, this can be done by rotating the sample or the lever with the optical detection system which is not very convenient. Another approach was presented in the work of *M. Dienwiebel et al.* [20], where a so called 'tribolever' was used [21] which is able to separate the forces in all 3 directions of the Cartesian coordinate system. Measurements on HOPG clearly showed a strong increase of friction at 0° and 60° which can be explained with the commensurable sliding of a graphite flake at the tip apex resulting in large friction. Calculations in the framework of the PT model [22] confirmed this very clearly. Another origin of anisotropic friction can be found in the periodicity of the sliding plane. A Al-Ni-Co quasicrystal is built such, that one sliding direction offers a periodic crystal structure, an aperiodic one when sliding along 90° off the periodic orientation [23, 24]. Sliding along the periodic direction results in large friction values. A totally different origin of friction anisotropy was attributed to the findings on alkali halides. Measurements along [100] and [110] orientations on the (001) plane showed reduced friction along the [110] direction [25], where ions of the same kind are aligned along the scan direction and therefore the energy barrier which the tip needs to overcome for a slip is expected to be smaller compared to the [100] orientation. This was qualitatively confirmed by numeric and analytic calculations on the base of the PT model using a sinusoidal potential [26, 27].
Measurements on *self assembling monolayers* (SAMs) were reported to show different frictional behavior depending on the tilt orientation of the molecules [28, 29]. Very good results were achieved by the direct comparison of friction forces on various domains with different tilt orientations, in the friction map the contrast between different domains is clearly seen. Using a newly presented technics called *transversal shear microscopy* (TSM), the torsional signal is measured when scanning along the cantilever axis [30, 31]. Measuring both, the TSM signal and the topography, *Campione et al.* claim to be able to reconstruct the friction along both lever axis. The measurements on β-alanine are showing a slight anisotropy using this method [32] originating form the molecular structure of the crystal. On the atomic scale, a contrast due to molecular orientation [33] or the surface structure of dolomite and calcite [34] can be measured. The anisotropic effects on this scale request new descriptions for the interaction between the tip and surface in order to explain the findings on the base of the PT model.

1.3 Force Calibration

The normal and torsional spring constants c_N and c_T of a rectangular cantilever can be calculated as

$$c_N = \frac{Ewt^3}{4l^3}, c_T = \frac{Gwt^3}{3h^2l}, \tag{1.8}$$

with the cantilever dimensions (length l, width w, thickness t, and tip height h), the Young's modulus E and shear modulus G [1,35]. With about 2 μm, the thickness of the cantilever is the smallest of the geometrical values which it is difficult to determine accurately by microscopic measurements. Because the spring constants are proportional to t^3, accurate values are crucial for the determination of c_N and c_T. A simple method to get an accurate value of t is by the measurement of the fundamental flexural resonance frequency using the formula [36]

$$t = \frac{2\sqrt{12}\pi}{1.875^2}\sqrt{\frac{\rho}{E}} f_0 l^2. \tag{1.9}$$

Another approach is also known as the *Cleveland method* [37], where an additional mass is attached to the tip. Knowing the effective mass of the cantilever m^*, the mass M of the added object, the spring constant can be calculated by measuring the shift of the resonance frequency. If the stiffness is not measured in *ultra-high vacuum* (UHV), the viscous medium should also be accounted for. The *Sader method* [38,39] allows the calculation using the length and width of the cantilever, the resonance frequency (f_N, f_T) and corresponding quality factor (Q_N, Q_T) as well as the fluid density ρ and viscosity η of the medium according to

$$c_N = 0.1906\rho w^2 l Q_N f_N^2 \Gamma_i^N(f_N, \eta), \qquad c_T = 0.1592\rho w^4 l Q_T f_T^2 \Gamma_i^T(f_T, \eta), \tag{1.10}$$

with the imaginary part of the known hydrodynamic function $\Gamma(f, \eta)$ [40].
The forces in normal F_N and lateral F_L direction can be calculated from the measured deflection signals V_N and V_L using

$$F_N = c_N S V_N, \qquad F_L = \frac{3}{2} c_T \frac{h}{l} S V_L. \tag{1.11}$$

The sensitivity of the photodiode S describes the conversion rate of the measured voltage to a deflection with the unit of meters and can be extracted from the slope of a force distance curve.

> *It's an ingenious solution to a problem that should never have existed in the first place.*
>
> James May

Chapter 2

Experimental Setup

Many different types of *atomic force microscopes* (AFM) appeared on the market since it was invented as a successor of the *scanning tunneling microscope* (STM) and probably as many were developed as prototypes. The principle is simple, a sharp probe attached to a spring is scanned over a sample surface while a detection system is measuring the force between them, though the ways of doing so are manifold. Depending on the field of application of the microscope, different techniques are preferably chosen. For the scanner it is for example important to know on what range it will be used, and what scan speeds are demanded. The range of forces to be measured, the materials investigated, measurement techniques that are used, and the environment of the measurement are important aspects for the selection of the probe and the type of force detection. If the microscope should be able to scan large areas of 100 μm and more, the scanner should have a very linear response and often flexure based systems are chosen. A piezo tube scanner on the other hand has an intrinsic curvature and hysteresis effects. For the use on small scan areas and moderate scan speeds it is suited and has the advantage to be very light and compact which is crucial for the microscope that will be introduced here.

Since the invention of the STM, the development of computers made it much easier to perform measurements and visualize the results. In the early eighties, line scans were cut out of carton and glued next to each other to get a three dimensional representation of the surface, which was then photographed for publication, as it was done for example when the first time the 7 x 7 reconstruction of silicon was measured in real space [41]. Nowadays, the computer is not only recording and visualizing the data, it also provides the interface for the operator and it is controlling the whole scan process and processing the signals with the use of *field programmable gate arrays* (FPGA). This enabled the development of sophisticated methods for manipulation at the nano scale, detecting smaller forces and different measurands beside the force, pushing the force microscopy to new scales and applications.

2.0.1 Status of the Existing System - 3*rd* Generation AFM

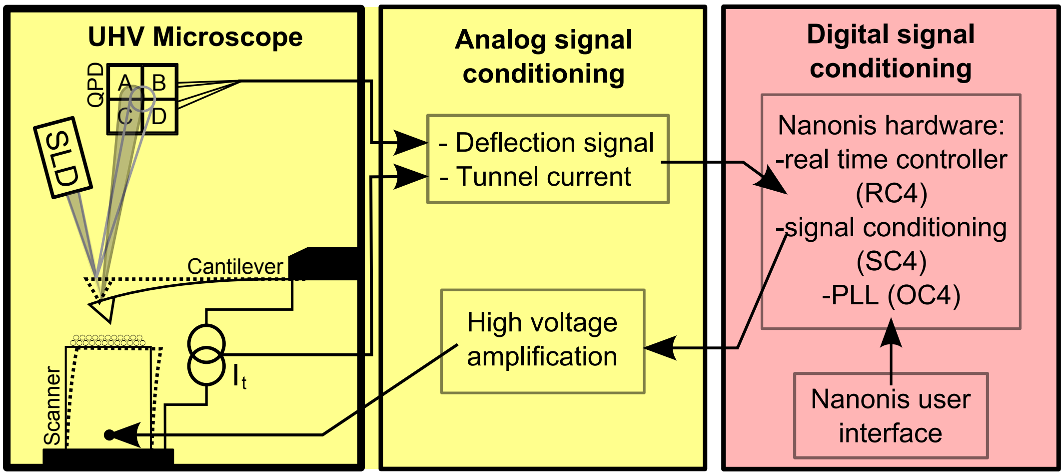

Figure 2.1. Scheme of the AFM and the electronics which is divided in the analog and digital stage. The yellow marked microscope and analog electronics are homemade, the commercially available Nanonis electronics is marked red.

In Fig. 2.1, a scheme of the *scanning probe microscope* (SPM) system is presented. The operator is controlling the microscope with the user interface on a computer where the measurements are visualized and saved. A Nanonis system [42] is used which has a LabVIEW based interface on the computer connected to the real time controller, which executes the commands from the user for controlling the scan process. Typically, a *phase-locked loop* (PLL) is connected to the real time controller for doing *frequency modulated* (FM) measurements and the signal conditioning unit for the *analog digital* (AD) and *digital analog* (DA) conversion. This marks the border to the analog stage of the electronics. The electronics for analog signal processing is developed together with the in-house electronic workshop. On one hand, there is the high voltage electronics amplifying the signals of the signal conditioning box for controlling the scanner as well as the motion of the slider and mirrors. On the other hand the measurement signals have to be processed and amplified, which is partially done in UHV but most of the electronics is located directly after the signals leave the UHV-chamber. Finally, there is of course the microscope inside the UHV-chamber with the probe and the optical beam deflection system and the scanner, which moves the sample relative to the tip in our design. Most of the parts of the microscope were made by the in-house workshop.

The basis for the new microscope that will be presented in section 2.1, is an already modified version of the UHV microscope described by *L. Howald* in 1993 [43]. On the base of this microscope, the company Omicron [44] which is now part of Oxford Instruments, made their room temperature SPM which was sold many times. The microscope can be seen in Fig. 2.2. The mirror motors changed from the original design in the citation and some changes in the wiring were made to make it possible to do *Kelvin probe force microscopy* (KPFM). A big improvement was the replacement of the laser diode in UHV by a single mode fiber, introducing the light of a *superlum diode* (SLD) form outside the vacuum chamber to the microscope (similar

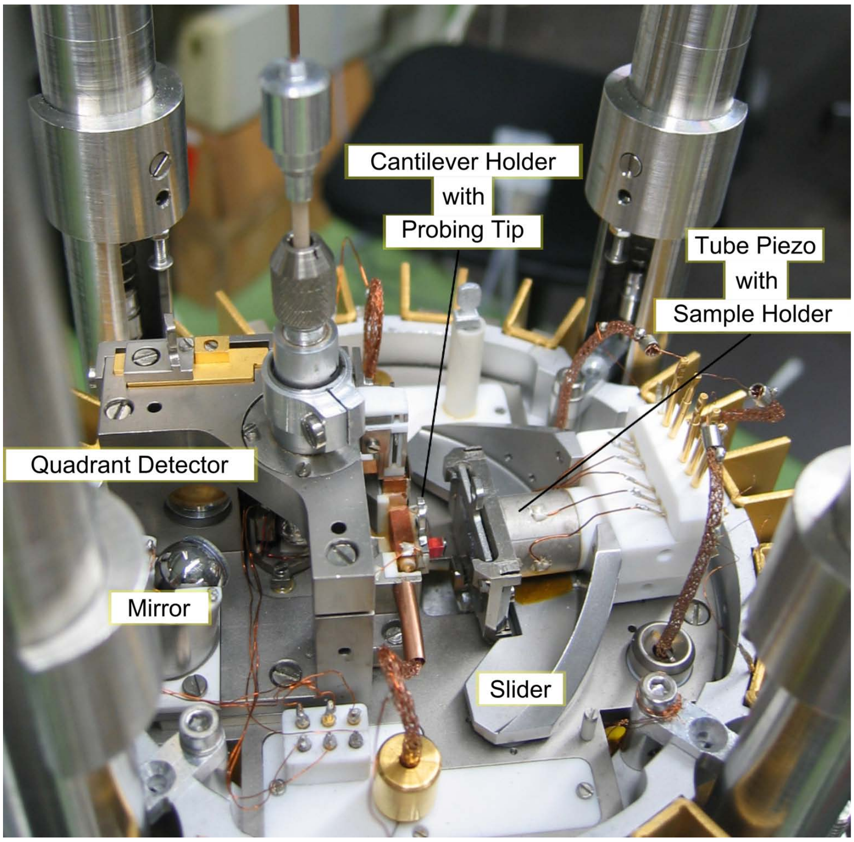

Figure 2.2. The predecessor microscope, a modified Omicron room temperature AFM/STM. High signal to noise ratio and very good thermal stability are probably the two most important qualities of this microscope.

as reported elsewhere [45]). This provides a more stable light intensity and increases the signal to noise ratio. The non coherent light of the SLD also avoids interference with reflected light from the sample surface. The second main change was the *current to voltage* (IV) conversion and preamplification of the signals right at the *quadrant photo diode* (QPD), increasing the bandwidth to about 3 MHz enabling to work with higher harmonic resonances of the cantilever. Various publications are proof of the great abilities of this microscope [46–51].
In the following, this microscope will be called the 'old microscope'.

2.0.2 Demands for the New Microscope

The new microscope is mainly assigned for high resolution measurements on flat surfaces resolving single atoms or molecules. This defines the main requirements of the new microscope: a good signal to noise ratio of the detection system, little mechanical vibrations, and the thermal drift needs to be small which becomes more important the longer a measurement is lasting. The new microscope should basically perform at least as good as the old one but have smaller drift rates, it should be easier to operate and maintain and offer additional functionality. The focus for the new microscope was set to the following points:

- Improved mechanical and thermal stability
- Easier and more reliable operation
- Modular setup for faster and easier maintenance
- Improved wiring
- Additional functionality
  - Additional electrical contacts
  - Second fiber and optics for optical excitation of the surface
  - Extended scan range

One special focus was the thermal stability. With the old microscope, it was shown that it is possible to do three dimensional force mapping at room temperature [49]. The main challenge is the compensation of drift over periods of several hours which is only possible if drift rates are stable and small. With the old microscope, this was only possible if the weather and air temperatures in Basel were very stable and no one entered the laboratory for some days. The new microscope should make it easier to do such long term measurements. Improving the mechanical stability is addressing vibrations. The old microscope has a pronounced eigenresonance around 300 Hz which should be avoided in the new microscope. The wiring of the old microscope was upgraded to do KPFM. Unfortunately it had to be done such, that the electrical connection between tip and sample became long, forming a loop which acts as an antenna. This induces such a large 50 Hz noise in the tunnel current signal that it is not possible to do STM anymore. This problem should be avoided in the new microscope. On the other hand, changes of the wiring can also help reducing the noise and reduce the heat transfer through the wires to the microscope platform. For the measurements presented in this thesis, the most important upgrade were additional electrical contacts at the scanner contacting the sample. Here, it was used to run the sample rotator described in section 2.1.5, but it can also be used to apply additional voltages or a current to a sample.

2.1 Room Temperature UHV AFM/STM

After the 1^{st} version built by L. Howald, the 2^{nd} that was described in section 2.0.1 from E. Meyer's group in Basel and a 3^{rd} that is used now in Saarbrücken, the here presented room temperature UHV AFM/STM is the 4^{th} edition of this type developed in Basel. After a detailed description of the new microscope, it will be compared with the 2^{nd} edition because this is probably the best device of the first three and it is in Basel at hand.

The microscope in the final state, when all the measurements in this thesis were done, is shown in Fig. 2.3. Compared with the 2^{nd} version in Fig. 2.2, the most obvious change is the horizontal way, the fiber is coming into the optics for focusing the beam of the SLD. The new orientation gives the fiber and optics a much less exposed position and prevents damage of the fiber or a detuning of the focus while

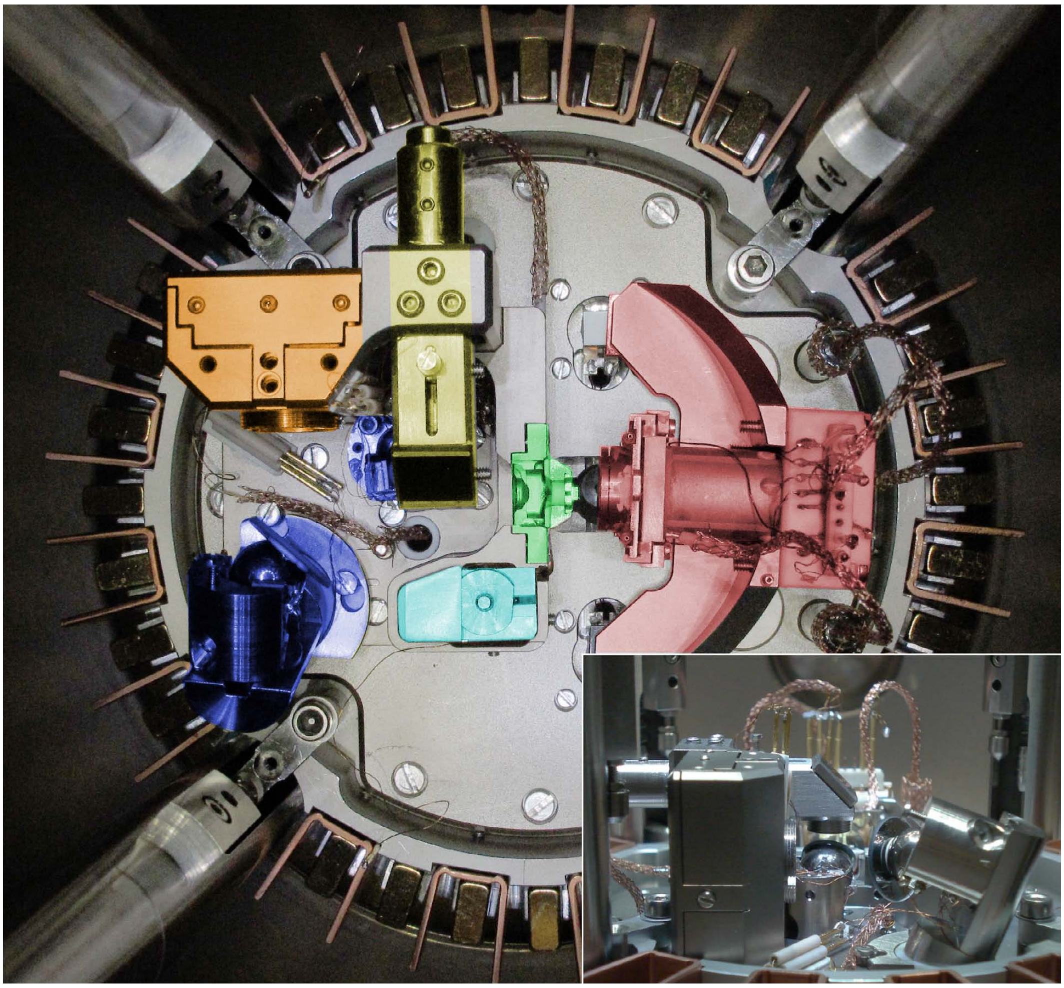

Figure 2.3. The new UHV room temperature AFM/STM from the top and in the inset a side view. The slider with the tube scanner and sample holder is colored red, the fiber optics yellow, the mirrors blue, the QPD orange, and the STM switch pale blue.

working with the wobble stick. This is indeed a problem in the old design that has always to be accounted for to prevent very long maintenance works. In the new design, the optical part is much better visible and the mirrors can even be reached with the wobble stick in case they are stuck at a certain position, without the danger of damaging the fiber.

Further changes were done at the AFM/STM switch, the mirrors, slider and its motors, tip mount, QPD housing, wiring, the microscope platform, and the electronics. All the demands for the new microscope were addressed with the changes but the additional fiber and optics for the excitation of the sample surface was not implemented jet, though the microscope is designed and ready for the upgrade. The detailed description of the new microscope, the new wiring and electronics is presented in the following subsections.

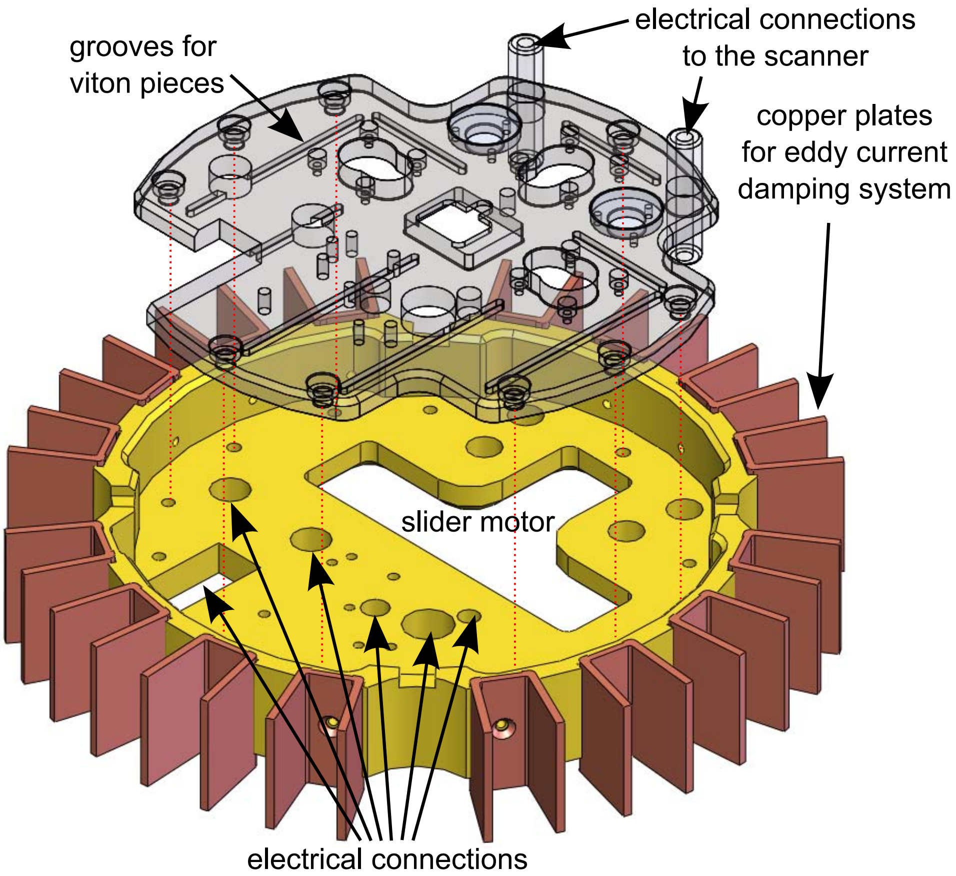

Figure 2.4. CAD image of the microscopes main body, which is made of two titanium pieces which are separated with viton stripes located in the grooves of the inner part. Screws at the border of the plates are fixing these two pieces building up some strain on the viton pieces. The copper plates surrounding the main body are part of the eddy current damping system.

2.1.1 Microscope Platform

The microscopes main body was totally redesigned but the outer dimensions were left identical, in order to integrate it in the existing eddy current damping system. In Fig. 2.4, a *computer-aided design* (CAD) image of the microscope platform is shown. It is made of titanium because it should be light to increase the effectivity of the damping system, and non ferromagnetic. If a ferromagnetic material is used, the magnets of the eddy current damping system will automatically pull the suspended microscope to the magnets and block it. Even a thin nickel layer on the copper plates, as it is often used as a barrier layer for gold coatings of copper, will show this result.

In the old design, the body has a pronounced eigenresonance at around 300 Hz, which is seen as noise in the measurement signals. The sandwich structure with the viton pieces should damp this eigenresonance. Numerical simulations using *finite element methods* (FEM) indicate that the resonance frequency of the platform is slightly shifted to higher frequencies compared with the platform without the inner part. Another beneficial effect of the separation with viton pieces is the smaller

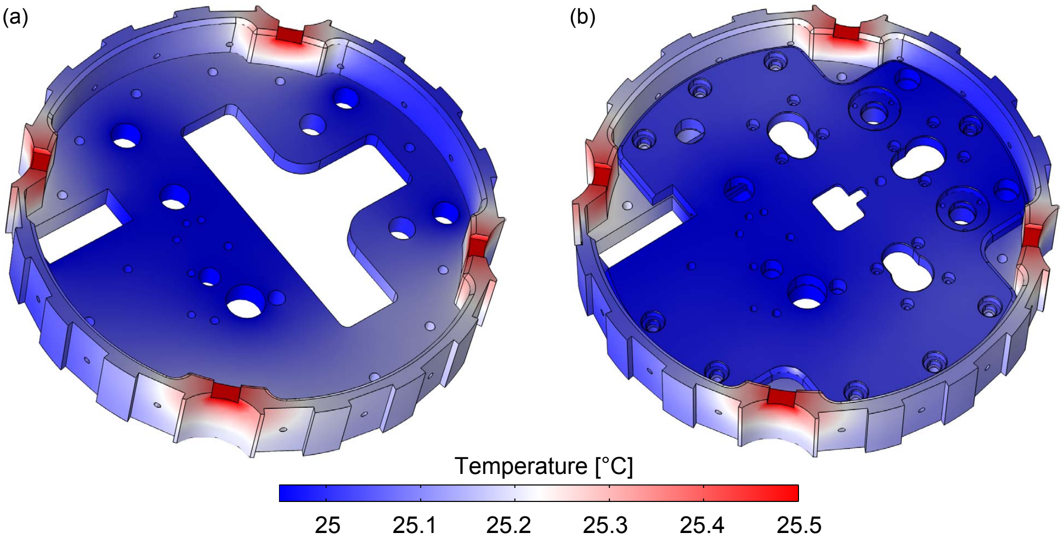

Figure 2.5. FEM calculated temperature distribution of the microscope with a heat bath at the positions of the spring attachments. In (a) only the outer part was considered, in (b) the result of the complete main body with the viton pieces separating the two parts is shown.

thermal contact between these two plates. In order to reduce thermal drift in the measurement, as little variation of temperature in the microscope as possible should be reached. Beside the radiative thermal contact with the surrounding from black-body radiation or light coming into the chamber, and the heat produced in the microscope itself, there is only a direct thermal contact over the electrical connections and the springs which are the suspension of the microscope. The springs are connecting the UHV chamber to the outer part of the microscope body, so the heat is first transferred there. Concerning the radiative heat transfer, the inner part with the optical block and the slider attached, is partially shielded by the outer part. In this sense, the outer part of the microscope body can also be considered as a thermal buffer. FEM simulations performed with the software COMSOL have shown that the inner platform is thermally more stable compared to a setup without the sandwich structure. For these simulations, the attachment points of the springs at the platform were set 0.55°C higher than the points where the electrical connections are connected with the microscope. The result of a steady state analysis is seen in Fig. 2.5. Another beneficial effect of the new body is the bigger total mass which also reduces the temperature variations.

2.1.2 Optical Sensing Block

The light of the optical detection system is emitted from one of the two available superlum diodes with the wavelengths of 678.5 nm and 830.6 nm (Superlum Ireland, SLD-261-MP2-DIL-SM-PD-FC/APC and SLD-381-MP-DIL-SM-PD-FC/APC with AC-PILOT-4-Driver). In the old microscope, only a 678.5 nm SLD is used but since the QPD that is used is a Hamamatsu S5980, which has the best spectral sensitivity in the range of 900 and 1000 nm, it is favorable to use the longer wavelength. Also, when the optical actuation of the surface will be implemented, it may be an

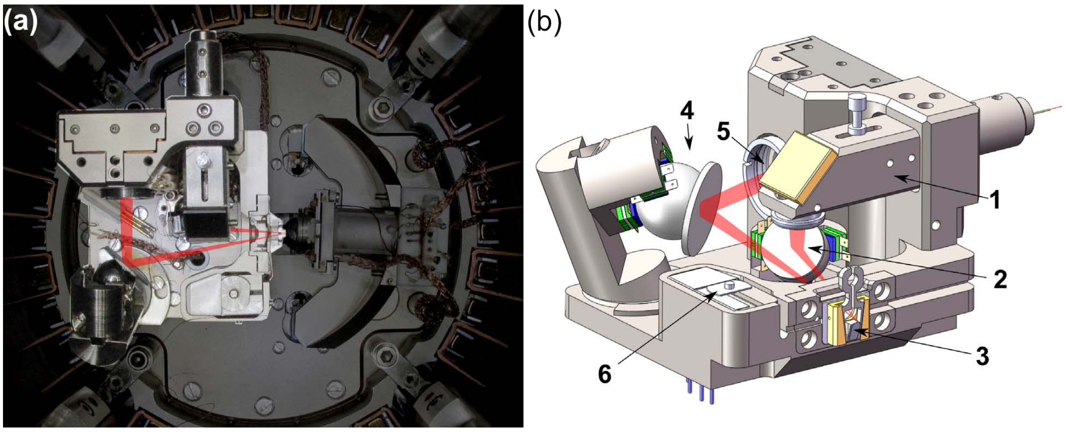

Figure 2.6. In (a) the optical sensing block is highlighted with the optical path drawn in red. In (b) the CAD representation of the optical detection system is shown with the attachment and optics for the fiber 1, the first mirror 2, the cantilever 3, the second mirror 4 and the hidden QPD 5. The STM switch 6 needs to be close to the tip.

advantage to have photons with lower energy, coming from the detection system. The red diode has a maximum light power of 2 mW with a bandwidth (FWHM) of 9.1 nm, the *infra-red* (IR) diode goes up to 3 mW with a bandwidth of 17.9 nm. The light of the diodes is coupled in to a single mode fiber which is ending in a FP/APC connector. The two diodes are in a box mounted on a big, passive cooling element and the FP/APC connector is plugged into a mating sleeve in the housing. One end of the single mode fiber (AMS Technologies AG, CB15959 single mode fiber) with a mode field diameter of 4.3 μm is connected there, while the other side is glued into a DN 16 CF flange separating the ambient and UHV sides, and finally ending at the optics for focusing the beam onto the cantilever. The optical path from the end of the fiber to the QPD can be followed in Fig. 2.6. The beam is first collaminated and then focused in the optics (Fig. 2.6(b)1) and then reflected on the first mirror (Fig. 2.6(b)2) which enables the precise positioning of the focused spot on the backside of the cantilever (Fig. 2.6(b)3). The beam is then going to the second mirror (Fig. 2.6(b)4) which has the task of centering the beam after passing another lens on the QPD (Fig. 2.6(b)5). In Fig. 2.7 the parts that are involved in the optical system are shown in more detail. The end of the single mode fiber was glued into a macor cylinder after removing the gold coating with nitro-hydrochloric acid to cleave the fiber, the macor piece was then glued into a titan envelope (see Fig. 2.7(a)). This end is fixed (but it can be adjusted) with two headless screws at the fiber optics body which is fixed to the main body of the optics. In a first lens with a diameter of 6.25 mm and a focal length of 10 mm, the incoming beam of diverging rays leaving the fiber is parallelized. The lens is mounted in a tube that can be moved back and forth to tune the correct position of the lens. The mirror between lens 1 and 2 reflects the light down to the lens 2 which has the same diameter as the first, but a focal length of 25 mm. This lens is fixed at a cylinder with a fine thread and can be tuned to optimize the focus on the lever, which can have a considerable effect on the noise level [52]. With this optics, the ideal opening angle of the beam which was calculated to be $\frac{D}{f} = \frac{1}{18}$ [53] with D the

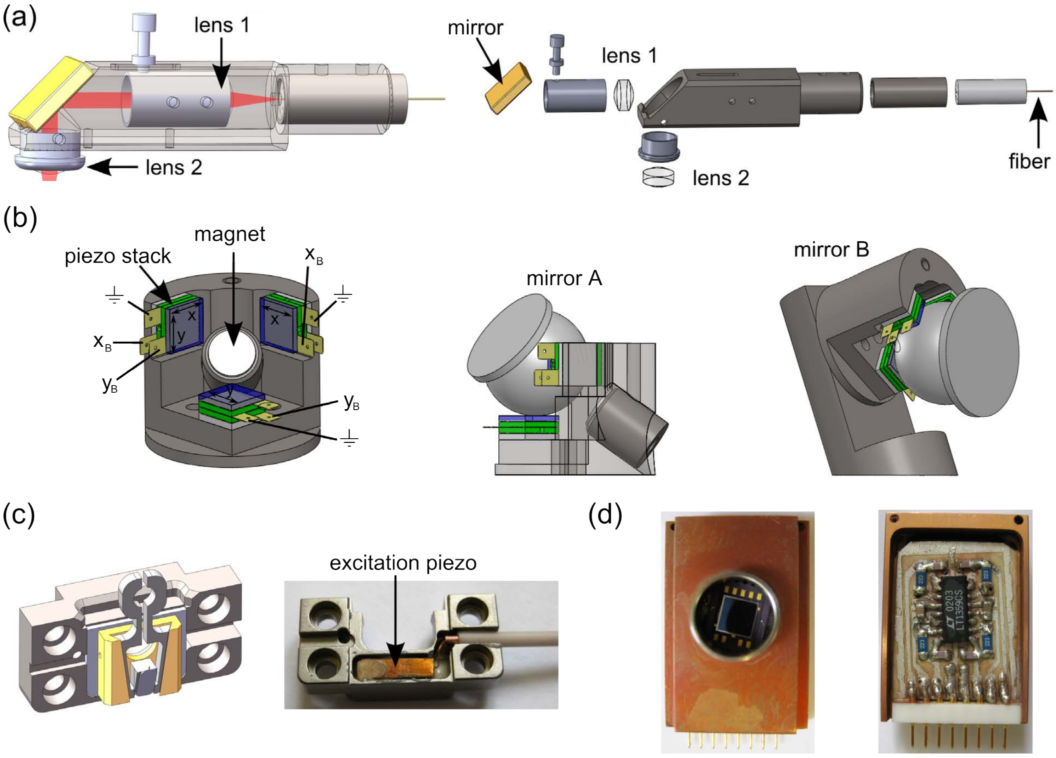

Figure 2.7. The fiber optics in (a) with the exploded assembly drawing on the right side. The two mirrors are shown in (b) with the wiring scheme of mirror B. (c) is the mounting of the cantilever with the piezo actuator for exciting the cantilever. The housing of the QPD and the electronics on its back side is seen in (d).

diameter of the parallelized beam and f the focal length of the focusing lens, can be approached very well. With $f = 25$ mm, the ideal collaminated beam diameter is $D = \frac{25\text{ mm}}{18} \approx 1.39$ mm. The spot size on the cantilever is approximately 20 μm in diameter. The setup with two lenses improves the ability to adjust the focus and opening angle compared to the optics in the old microscope with only one lens.

The mirror motors are an improved version of the ones developed by L. Howald for the first version [54]. The first mirror (mirror A) in the microscope is a slightly modified one from Omicron, the second one (mirror B) is very similar, but home-made. The probably most obvious difference is the mounting of the mirror B in Fig. 2.7(b). This was done because the mirrors work best when they are operated in the orientation when the cylinder with the magnet is about perpendicular to the mirror surface. The mirror plane of mirror B is with 18 mm diameter bigger than mirror A (12 mm) because variations in the position of the glued cantilever have a relatively big effect on the spot position on mirror B and also the spot size is bigger on mirror B. To control the movement in horizontal (x) and vertical (y) direction of the mirrors, 3 electrical lines are required, a *ground* (GND) and the cables to drive x and y. The mirror body is connected to GND but it is electrically separated from the microscope platform by a ceramic plate. This was done to avoid any substantial currents through the ground of the microscope platform. On the other hand, it is necessary to have the ground of the *high voltage* (HV) electronics steering the motors

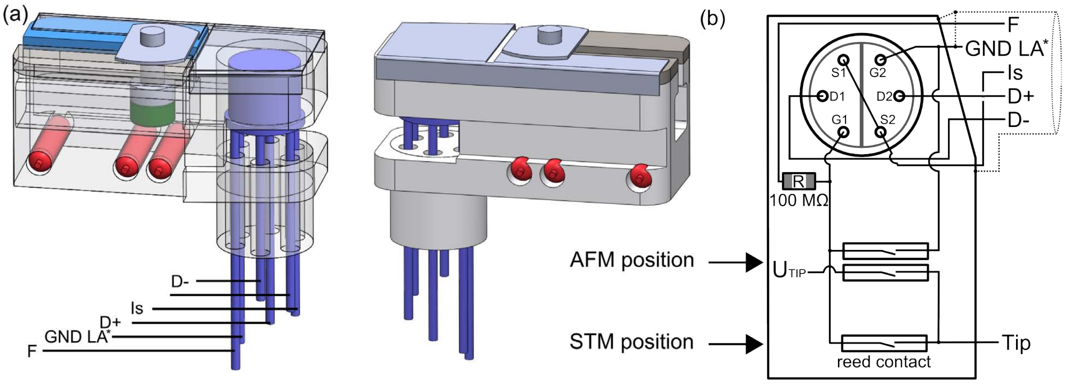

Figure 2.8. In (a) the STM switch with the preamplifier is shown. On the left side the main body and the top cover are transparent to give the insight in the device. The metallic stamp for switching between the two positions has a magnet (green) at the end, closing the reed contact (red) near it. A scheme of the switch is shown in (b).

twisted around the x and y cables to reduce the picked up noise on the lines. The connectors are redesigned to be more compact and to have the connectors of the two mirrors spatially separated. The connectors could also be shielded for future. The whole design should be less vulnerable for picking up noise which is moving the mirrors and therefore coupling directly to the beam deflection signal.

The cantilever holder with the excitation piezo is an easily replaceable module in the new microscope (Fig. 2.7(c)). The electrical connection is shielded very carefully all the way from the feedthrough to the piezo. On the left side of the cantilever holder is a groove for the electrical connection of the tip bias and tunnel current line.

In Fig. 2.7(d), the housing of the QPD is seen. The back side is shown without the copper cover plate revealing the electronics on the back side of the QPD for the in situ IV conversion increasing the bandwidth to 3 MHz (described in detail in section 2.2.1).

2.1.3 STM Preamplifier and UHV Switch

The AFM/STM switch has two settings: In the AFM position, it is grounding the tunnel current preamplifier and connecting the tip with the bias line. In this position, the STM is disabled. When the STM position is selected, the bias line is open and the gate of one *field-effect transistor* (FET) is connected to the tip. In this configuration, the current between sample and probing tip can be measured but it is also possible to do AFM measurements simultaneously with the constraint that the bias can only be applied to the sample. Detailed information about the circuit, which the preamp is part of, can be found in section 2.2.3.

The new switch was designed to provide better reliability when it is used and for easier operation. The manipulator gives a very limited force feedback, gentle and precise movements are often challenging or even impossible tasks. In the old design, a pin was moved which had to make the electrical contact. The new switch is using the magnetic coupling between a small magnet (green in Fig. 2.8(a)) and the reed switches (red). The commercial available reed switch consists of two contacts in a glass envelope which are separated by a small gap which is closing when a magnetic

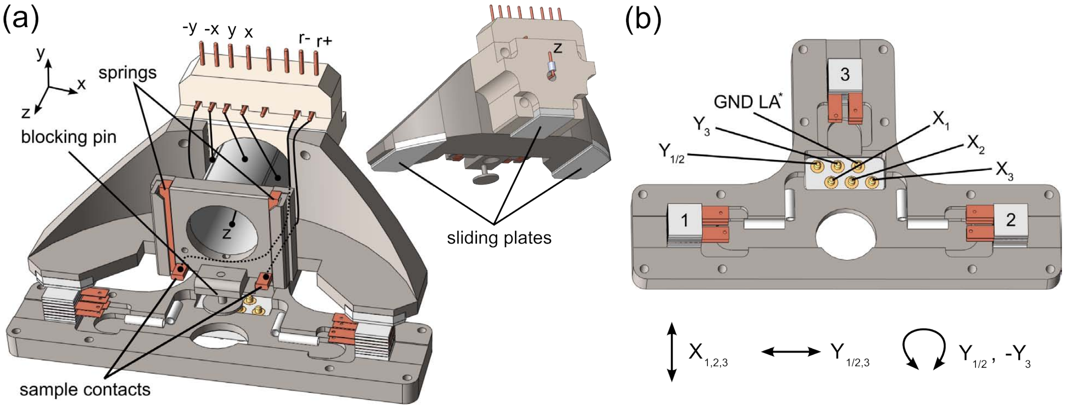

Figure 2.9. The slider (a) with the piezo tube scanner and the sample holder at its end is lying on the three sliding planes of the slider motor (b). The rotator can be translated along x and y as well as rotated by using the assigned motors.

field is applied. Since the switching process is mediated with a magnetic field, the mechanical switch does not have to make direct contact with the actual contacts. This makes it easier to improve the sliding properties of the switch and the switching process can be made very simple and the contacting reliable.

The moving part that selects the AFM or STM function is stuck in its normal position because the cover, shielding the preamp, is lifting and wedging the stamp on one side. When the manipulator is applying a normal force on the switch, it is free to move and can be slided gently to the other position. This mechanism makes it easy to select the STM or AFM function and prevents unintended switching between them.

2.1.4 Slider and its Motors

The slider with the scanner has three hardened metal plates on the bottom as the sliding surface. In addition to the gravitation force pressing the slider against the ceramic plates of the motor, a magnet in the microscope body is increasing pressure on the sliding interface. In Fig. 2.9(a) the slider on the motor is shown. The basic design of the slider was not modified compared to the old microscope. The pins at the sample housing contacting a specially designed sample plate are new. Because the size of the optics has slightly increased, there is less space between sample surface and the cantilever. To compensate this, the ceramic part with the scanner attached is a bit smaller on the back side, therefore the sample can be retracted further. This required a modification on the bottom of the sample housing for blocking the scanner when the slider is fully retracted (see blocking pin in Fig. 2.9(a)). In the blocked position, a manipulator is supporting the scanner at the blocking pin to avoiding large forces and damage on the piezo tube when the sample is changed. The scanner is a PT230.24 with a PIC 255 ceramic type from the company PI. The pin for connecting the z-contact is spatially separated from the other pins and shielded all the way to the UHV feedthrough to pick up as little electrical noise as possible.

Fig. 2.9(b) shows the slider motor which is a single module, the old microscope

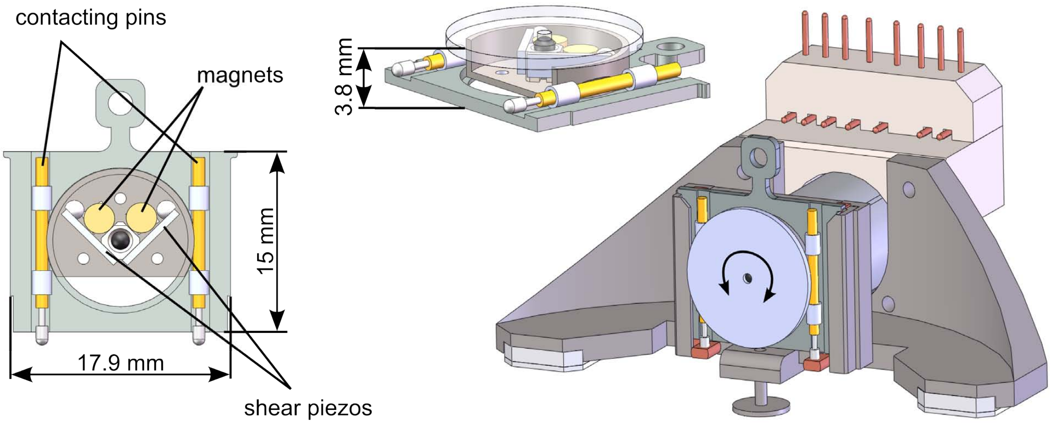

Figure 2.10. The sample rotator mounted on a sample plate. The two pins are contacting to the new connections at the sample holder.

had 3 separated piezo stacks. This change makes maintenance very convenient, the module is removed and the piezo stacks are always nicely aligned to the surface of the running plates of the scanner. This motor is used for the coarse approach of the sample to the tip. The scanner can be moved as described in Fig. 2.9(b). The direction X is approaching or retracting the scanner, Y can move the sample sideways and the rotation is used to reduce the tilt of the scanned surface. In the coordinate system of the scanner, the slider can move along x and z, but not along y which limits the scannable area on the sample to a stripe with the height of the scan range in y, but along x the full sample can be scanned.

2.1.5 Rotatable Sample Holder

The size restrictions for building the rotatable sample holder were given by the design of the sample plate and the space between the plate and the cantilever in the microscope. The surface of the sample plate has the dimensions of 17.9 mm × 15 mm (width × height) but almost 1 mm at the sides of the sample plate can not be used because of the rails of the drawer like fixing of the plate on the scanner (the same restrictions apply on the carousel and the manipulator in the lock). This reduces the usable width to 16 mm. The thickness should be kept as small as possible to get a large gap between the surface of the rotator where the sample is mounted, and the cantilever. The smaller the gap between tip and retracted sample, the harder it gets to do the transfers of the sample and tip without damaging one of them. Finally it was possible to do the whole design with a total height (sample plate and rotator) of only 3.8 mm which allows to use also bigger samples such as a cleaved alkali halide crystal.

The working principle of this motor is the same as in other piezo driven motors: the part that has to be moved is pressed against one or several piezos which are normally covered with a sapphire or polished ceramic piece. When a sawtooth shaped, electrical and periodic signal is applied to the piezos, they are moving in the plane of the interface, fast in one and slower in the opposite direction. If the pressure on the interface is chosen such that the mass to be moved is resting when the

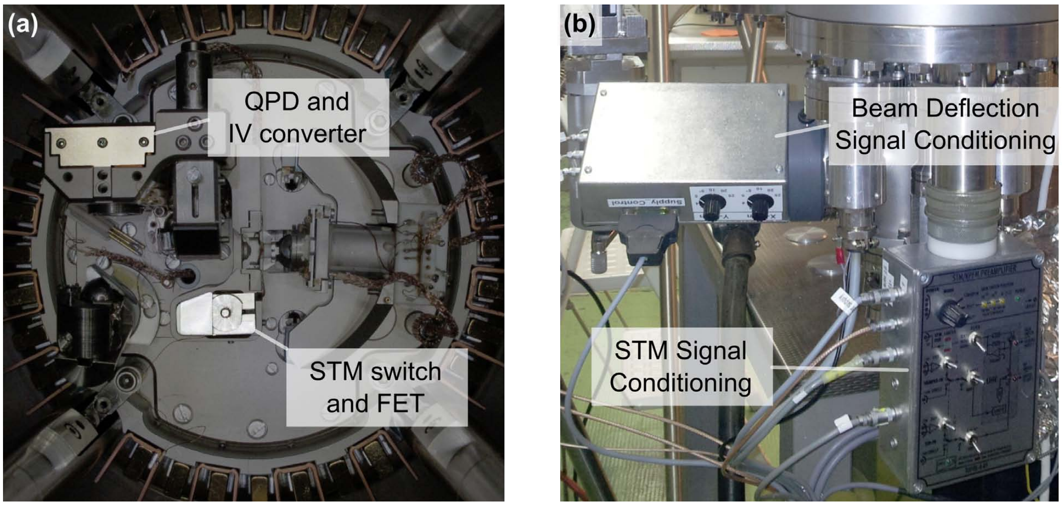

Figure 2.11. The analog signal conditioning is done in the electronics shown in this figure. In (a) the STM Switch and the position of the QPD and the IV converter are highlighted. (b) is a photo of the electronics that is mounted directly to the UHV chamber.

piezo are doing the fast movement (i.e. sliding in respect to the moving support), and sticking occurs when they move slower, a macroscopic movement along one direction is resulting.
The sample on the rotator is attached to the round plate covering the motor which is the moving part (see Fig. 2.10). The hole in the middle defines the center of rotation and is one of three points where the plate is supported. The other two points are supported by the ceramic balls at the end of the two shear piezos. The plate is pressed against these three points with the two cylindrical magnets. When a voltage is applied to the piezos, they move the ceramic balls on a circular path around the center where the piezos are fixed. The motor only works if the system is tuned such, that the plate is sticking to the ceramic balls when they move slowly and sliding occurs during the fast movement. The force between magnet and plate can not easily be changed making it hard to tune the motor that it is working properly, but there are other parameters that can be changed such as the material (ferromagnetic properties of the plate), the surface roughness (influencing the friction properties) and the mass of the plate (and therefore the inertia). The pins need to make a proper electrical contact when the sample plate is at it's position on the scanner. When the sample plate is on the scanner, the springs inside the pins are contracted, pinching the pin between the sample plate and the contacts on the scanner. The sample plate is electrically connected with the sample holder and therefore a bias voltage can be applied to the sample, therefore tunneling and measuring the contact potential is possible.

2.2 Electronic Components

In this section, the analog signal conditioning is described on the way from the raw signal until the signal is fed to the Nanonis signal conditioning electronics where it is digitalized. The complete analog stage was developed with the in-house electronic workshop of the department of physics. The electronics can be divided in an AFM and a STM section. For the AFM signal, the photo current originating from the photo diode, undergoes the IV conversion directly behind the QPD in UHV (see Fig. 2.11(a)) to push the bandwidth of the deflection signals to > 3 MHz. Operating electronics in UHV is normally avoided because printed circuit boards are usually not UHV compatible. Another problem is the UHV compatibility of the electronic components. Heat production in these parts must be dealt with, because virtually no convective heat transport with surrounding gas is possible and warming up the whole microscope is very unfavorable. Further amplification of the deflection signal is done in the electronics mounted directly at the microscope chamber, but on the ambient side (see Fig. 2.11(b)).

The tunnel current needs a special treatment too, part of the circuit for its IV conversion and amplification is located very close to the tip in the UHV chamber, namely two FET transistors and a resistor that is part of a so called cascode amplifier. Further treatment of the signal is done on the ambient side directly at the electronic feedthrough. After the analog signal conditioning, the signals are fed with coaxial cables to the Nanonis electronics. The details of the complete wiring, shielding and the different grounds of the microscope are described in section 2.2.4.

2.2.1 3 MHz Quadrant Photo Diode

The light beam from the SLD diode is oscillating according to the cantilever motions when it impinges on the Hamamatsu S5980 *Quadrant Photo Diode* (QPD). The beam oscillations are converted into 4 photo currents by the segments of the QPD. The QPD is mounted on a circuit board with the IV converter on the back side (see Fig. 2.12(a)). The capacitance of the cables between the diode and the IV converter have the effect of a low pass filter for the signals. If the cables are long, they have to be shielded, requiring the use of coaxial cables with relatively high capacitances reducing the bandwidth of the system. By mounting this first stage of amplification very close to the diodes and converting the photo current to a voltage, the bandwidth of the signal can be increased many times over.

The Hamamatsu QPD is a PIN type diode which are known to have a quite low intrinsic capacitance. It is operated in a reverse biased mode with 15 V applied to broaden the depletion region in the diode which reduces its intrinsic capacitance even more. Like the cable, the capacitance of the diode is reducing the bandwidth, so it should be as small as possible. With the 15 V bias, it is reduced from about 45 pF to 15 pF. The 4 signals are then going to the LT1359CS *integrated circuit* (IC) chip for IV conversion. The signal from quadrant A from the diode to the output is colored in red in Fig. 2.12(b), and has the same circuit like the other signals. The negative feedback over the 22kΩ resistor from the output to the inverting input of the transistor is avoiding a voltage difference between the two inputs. With the other input on ground this gives the output voltage $U_A = -RI$. The capacitor parallel to the feedback resistor is preventing oscillations and has the effect of a low pass filter with a cutoff frequency of $\approx \frac{1}{2\pi CR}$ which is resulting in the 3 MHz bandwidth. The output signals after this inverted IV conversion are then in the range of -2.5 V to 0 V.

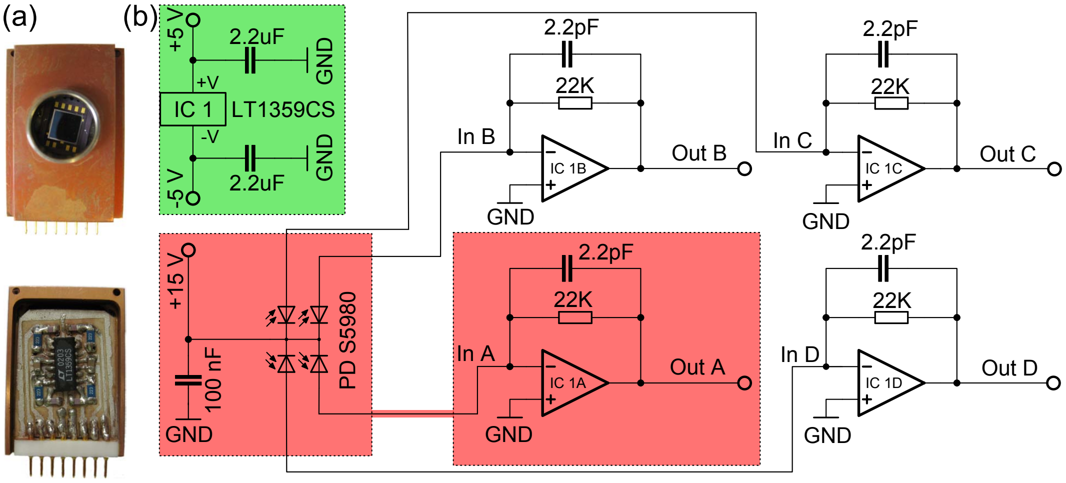

Figure 2.12. The Hamamatsu S5980 QPD can be seen in its housing in the image (a) and the backside of the open QPD box with the IV converter. (b) is the scheme of the circuit of the diode with the IV converter. The red box shows the biased Hamamatsu photodiode and the circuit for the signal of quadrant A, in the green box the integrated circuit IC 1 (containing IC 1A to IC 1D) is shown which needs the ± 5 V power supply.

The whole circuit is well shielded in the copper housing with the round opening at the position of the quadrant diode. The cylinder protruding there, is defining the rotation center for the housing of the QPD. The ability to rotate the housing allows the precise orientation of the QPD to the incoming ray with the two separated oscillation directions to get a well separated normal and horizontal deflection signal.

2.2.2 Amplification Box for the Beam Deflection System

The signal from the QPD after IV-conversion leaves the UHV-chamber trough a D-sub 15 feedthrough on a DN 40 CF flange. There, the electronics for the amplification of the signals is directly attached to the chamber. The electronics provides the power supply of the IV-converter at the QPD with +15 V, ±5 V and the GND. The four signals of the quadrants are in the range of -2.5 V to 0 V coming into the electronics for amplification and calculation of the horizontal, vertical and sum signal. In addition to this, the electronics has a laser driver and can read out two PT100 temperature sensors. These were not used up to now and will not be described here. For further information, see the complete circuit schemes in the appendix 6.1. There, the complete circuit for the gain selection and the voltage drivers for power supply can also be looked up.

The scheme in Fig. 2.13 is the circuit reduced to the most important parts for the signal conditioning. On the left side, the four signals are entering the electronics. The red boxes of signal B, C and D replace the exact same circuit as the one from A which is basically the same kind of circuit as used in the IV converter at the QPD. After the signal was inverted once there, this second amplification with the gain of -4 results with the correct sign. The capacitors at the power supply of the transistors to the GND are all for stabilizing the voltage. At the output of the red box, the signals are in the range of 0 V to 10 V. In the green boxes of the scheme, the vertical,

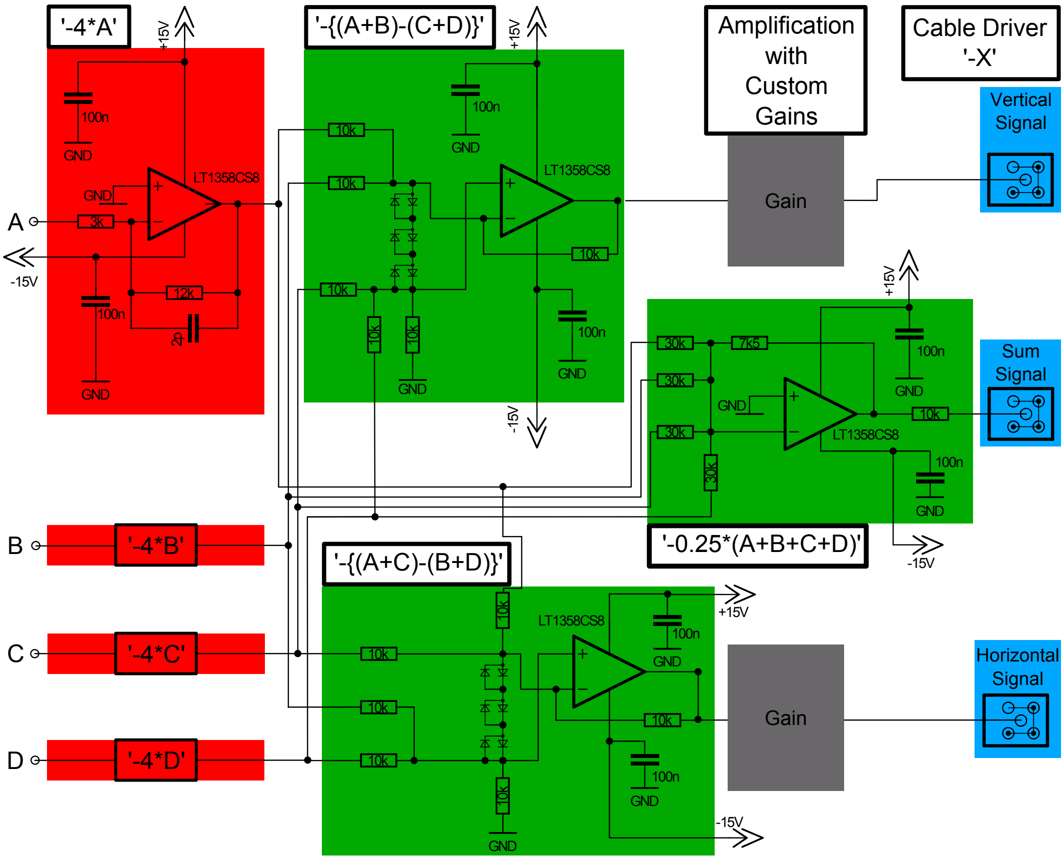

Figure 2.13. Simplified scheme of the amplification electronics of the beam deflection signal. The full scheme can be found in the appendix 6.1. In the red part the signals are amplified by a factor of -4, in the green boxes the vertical, horizontal and sum signal is calculated. The gray boxes contain a further amplification stage and the blue boxes represent cable drivers which also changes the sign of the signal.

horizontal and the sum signal are calculated but at this stage with the wrong sign. For calculating the sum signal, the resistances are selected differently resulting in a reduction by a factor of 4 of the final signal so that the output of the sum signal is still between 0 V and 10 V. For the calculation of the vertical (A+B)-(C+D) signal or the horizontal (A+C)-(B+D), the signals from the quadrants of the photo diode are either at the inverting input of the transistor for subtraction, or at the positive for addition. These two deflection signals are then amplified with gains of 1,2,4,5,10 or 20, depending how 3 digital inputs are chosen for each signal. This gain can be selected either with a switch at the electronics or by the corresponding digital input lines connected with the Nanonis electronics where it can be set in the Nanonis user interface. A last multiplication with -1 is done in the cable drivers (blue box in Fig. 2.13).

Besides the D-sub 15 feedthrough connected at the microscope chamber, there is a second D-sub 15 connector at the electronics for the power supply with ±15 V and GND, totally 8 digital inputs for the gain selection (2 are unused), +8 V power supply for the laser driver, an input for setting the output current of the laser driver, and the two readout channels of the PT100 temperature sensor. The sum signal,

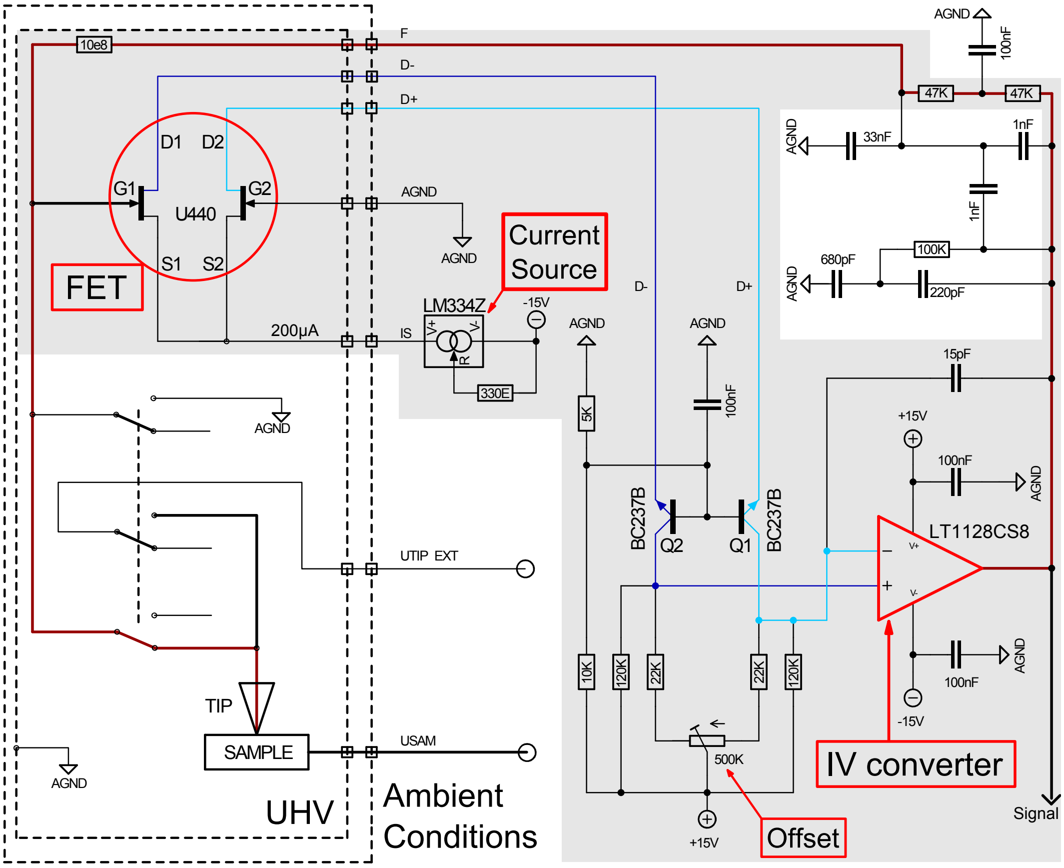

Figure 2.14. In the left box the UHV switch in the STM position with the three reed contacts is illustrated. The path of the current trough the back coupling line is highlighted in a Bordeaux red color. The cascode circuit is drawn on the gray background.

horizontal and vertical deflection signals are leaving the electronics over 3 camac sockets.

2.2.3 Tunnel Preamplification Box - TuPre-4

For the STM function, the precise measurement of the tunneling current is crucial. The current to be detected is roughly ranging to ±100 nA which requires an appropriate electronics. The capacitance of the wires between the current source and the amplifier is limiting the bandwidth. If this distance is large, the electrical connection has to be shielded properly, normally a coaxial cable is used which has a capacitance of about 1 pF cm^{-1}. Because the amplification factor of the IV converter is 10^8 (±100 nA = ±10 V), the capacitance has a huge influence for the resulting bandwidth. In our setup, the 100 MΩ resistor of the IV converter is mounted as close as possible to the FET to keep this capacitance as low as possible, the distance is about 1 cm inside the fully shielded STM switch.
For the voltage conversion and amplification of the tunnel current a cascode circuit was chosen. This circuit has two FETs (in the U440 device) which can be used inside the UHV chamber and very close to the tunnel barrier. One gate of one FET is grounded, the other is directly connected to the tip (see Fig. 2.14). The two

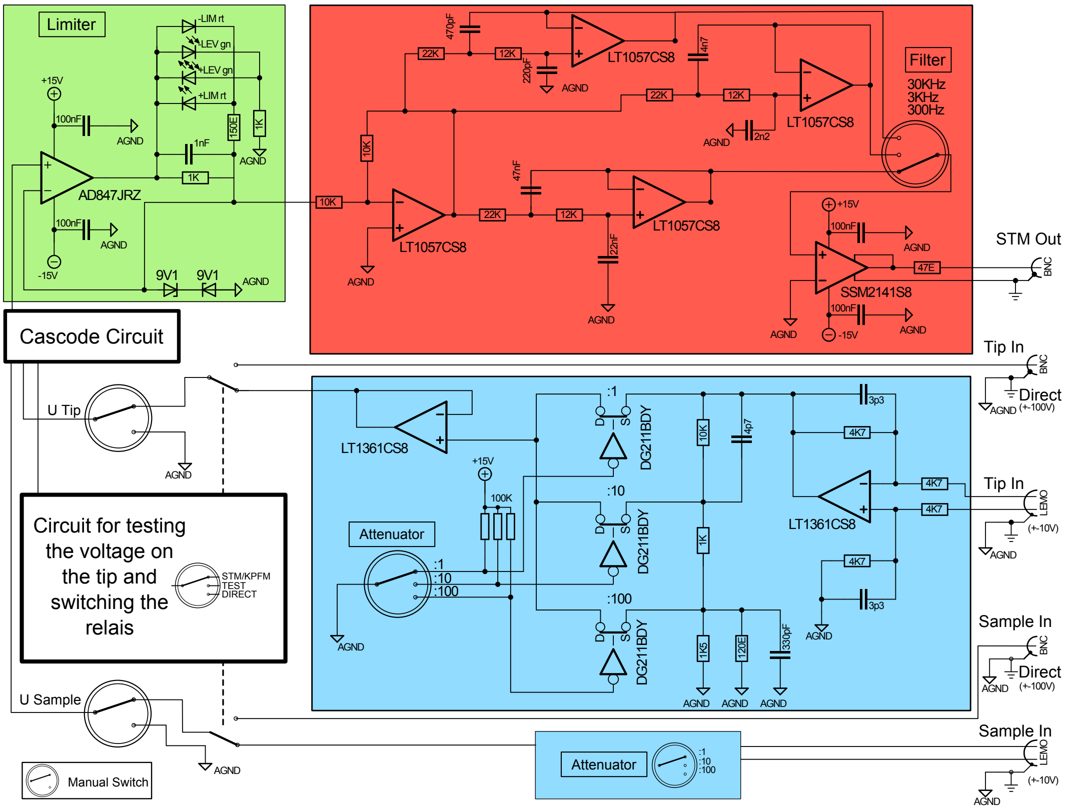

Figure 2.15. A simplified scheme of the TuPre-4 box is shown here. The full scheme can be found in the appendix 6.1.

sources are both connected to the same power supply providing 200 mA in total. On the drains is therefore also 200 mA current in sum, but the distribution on the two channels is depending on the tunnel current. These lines from the drain are now the signal lines that can be prolonged without problems down to the flange and on the ambient side to the IV converter. The whole cascade circuit is marked with the gray background. The switch below the FET in UHV is in the STM position, the AFM position basically grounds the FET to protect it of the high voltages from the externally applied voltage to the tip. The section that is not marked on the right side is a stabilizing network. In the previous version, it was possible to select between two gains which required this network to avoid oscillations. The characteristics of the two FETs in the U440 device in the cascode circuit is always a bit different. Many of those U440 FETs were carefully tested to ensure to finally select a device with two very similar transistors. A small offset in the measured tunnel current is the result of the different characteristic of the transistors which can be compensated with the proper setting of the potentiometer on the bottom of the circuit. The cascode circuit meets the requirements for the amplification of the tunnel current, but it is also a good choice concerning the heat production in the FETs in UHV which is quite small and constant, independent of variations in the tunnel current.
After the amplification of the tunnel current, the STM signal is fed to the limiter (green box in Fig. 2.15). The two diodes on the bottom of the box are grounding the signal when it is close to 10 V. The 4 light emitting diodes are indicators to

roughly show the value of the signal. The green diodes are getting brighter with increasing voltage and the red ones are on when the limiter is grounding the output. The signal in the range of ±10 V is then finally entering the last, red marked filter stage. With a switch, it can be chosen from three different filters (300 Hz, 3 kHz and 30 kHz) limiting the bandwidth. Between the switch and the camac socket, a cable driver avoids large loads on the filters.

For STM operation, a bias is applied to the sample to define the direction of the tunnel current. Operating the microscope as an AFM often requires a biasing of the tip. With a manual switch, the tip and sample can be grounded or connected to the bias lines. To protect the tunnel preamplifier from high voltages, a special circuit on the TuPre-4 circuit board is testing the setting of the UHV switch. If the UHV switch is in the AFM mode and the operation mode is set to "Direct", a relay is switching to the direct biasing allowing voltages up to ±100 V. When working with bias voltages of up to ±10 V, the differential inputs can be used when the mode "AFM/KPFM" is selected. Three attenuator settings can be chosen when working in this mode, no attenuation, and the reduction of the signal with a factor of $\frac{1}{10}$ or $\frac{1}{100}$ (see blue box in Fig. 2.15).

There are 4 additional lines for additional connections which are not drawn in the circuit schemes here. Two of them are connected with the newly added pins on the sample holder connecting the rotator on the sample plate. Each of these lines can be grounded by a manual switch on the box.

The complete circuit scheme of the TuPre-4 is shown in the appendix 6.1.

2.2.4 Wiring

The wiring concept of all the components in the AFM should be considered carefully. The electrical noise which is picked up in the wires needs to be reduced to a minimum. The electrical contact should be good with only small voltage drop over the electrical connections and therefore small resistance is favorable. Because mechanical oscillations need to be avoided, the wires should have little influence on the vibration damping of the microscope meaning they should be flexible and transduce very little vibrations to the platform. Mechanical oscillations can also be induced by electrical noise on connections of the piezo motors. Another important aspect for a UHV microscope is the heat transport through the wires. Since the wires and the shields are made of copper or an alloy of copper and beryllium, they can play an important role.

The vibration isolation of the microscope is an eddy current damping system. The microscope platform is suspended on 4 springs and the copper plates mounted around the platform are in the magnetic field of 16 strong magnets between the plates. The magnets are mounted at the pillars that are holding the springs, so, if there are vibrations, the microscope and the copper plates move relative to the magnetic field inducing eddy currents in the copper plates. The resulting Lorentz force is damping the movement which otherwise would keep oscillating for a long time in UHV. The wires connecting the platform with the flanges, transduce mechanical vibrations to the damped platform. To keep this perturbation as small as possible, we used very thin and flexible copper wires from the company California Fine Wire with a diameter of 0.1 mm including the polyimide (kapton) insulation. The length of the wires is chosen such, that there is no tension even when the microscope is lifted and blocked. The wires are lying on the flange (with a polyimide foil in between for electrical insulation) and the ends are gently lifted by the suspended microscope to reduce the force that is transferred to the microscope by vibrations of the whole system. The most rigid mechanical connection from the chamber to the microscope is the fiber guide for the optical detection system. Another positive effect of the small diameter of the wires is the reduced heat transfer over the electrical lines. The resistance on the other hand, is proportional to the area of the conductors cross section and therefore it is bigger with the long and thin wires. With a length of almost 50 cm and connector pins soldered on both sides, the resistance of such a cable is in the range of 1 to 3 Ω which is acceptable.

The thermal stability should be improved because of the weak heat connection over the electrical lines. The copper cables are used because they have a very good electrical conductivity and it is well suited for UHV use. The thermal conductivity of copper, on the other hand, is also good, which is a disadvantage here. The reduction of the wires cross section compared to the wires of the old microscope reduces the thermal conduction trough the wires. The sandwich structure of the microscope's main body with the viton pieces clamped between two titanium plates should also have a positive effect as it was seen with the FEM simulations in section 2.1.1.

Noise in the measurement signals can have a mechanical or electromagnetic origin. The eddy current damping reduces the mechanical disturbance from outside, a smart wiring can help reducing the one with an electromagnetic origin. Keeping electrical lines free of noise is crucial for the performance of the microscope. Noise can directly disturb the electrical signal of the measurement, originating form electromagnetic waves coupling into the wires. But it can also produce oscillations of the piezo motors of the microscope when it is in the wires connecting the piezos with the electronics, finally with the same result to the signals. A proper shielding of an electrical connection prevents the penetration (and emission) of electromagnetic waves to (and from) the actual conductor carrying a signal. Especially for the connections to the piezo motors, the emission of electromagnetic signals is also an important aspect. The twisting of wires has a similar effect like shielding them. If a signal is picked up on a twisted cable from an external electric field, it is changing the sign every time a conductor and its mass is twisted 180 degrees, canceling each other out. For twisting the wires, a simple device was made with spools of the copper wire attached to a plate. This plate can be attached to a driller and when the plate rotates, the wires are turned around each other. The fact that the wires are very thin and weak makes it virtually impossible to do a nicely twisted wire by hand.

The scheme of the whole wiring from the Nanonis electronics to the microscope can be looked up in Fig. 2.16. One important detail is the grounding of the shields. The whole microscope platform is on the ground called LA*, which is supposed to be very clean and free of substantial currents. The mirrors, the slider motors, the QPD and the STM switch with preamp are shielded by LA*. All of these connections are important regarding the transfer of noise to the measurement signals but they are not carrying signals with big variations of voltage and fast oscillations, except the QPD. But beside the small amplitude of the oscillations, all of the quadrants are in one shield and the sum of all the quadrants should not oscillate. Oscillations of voltage

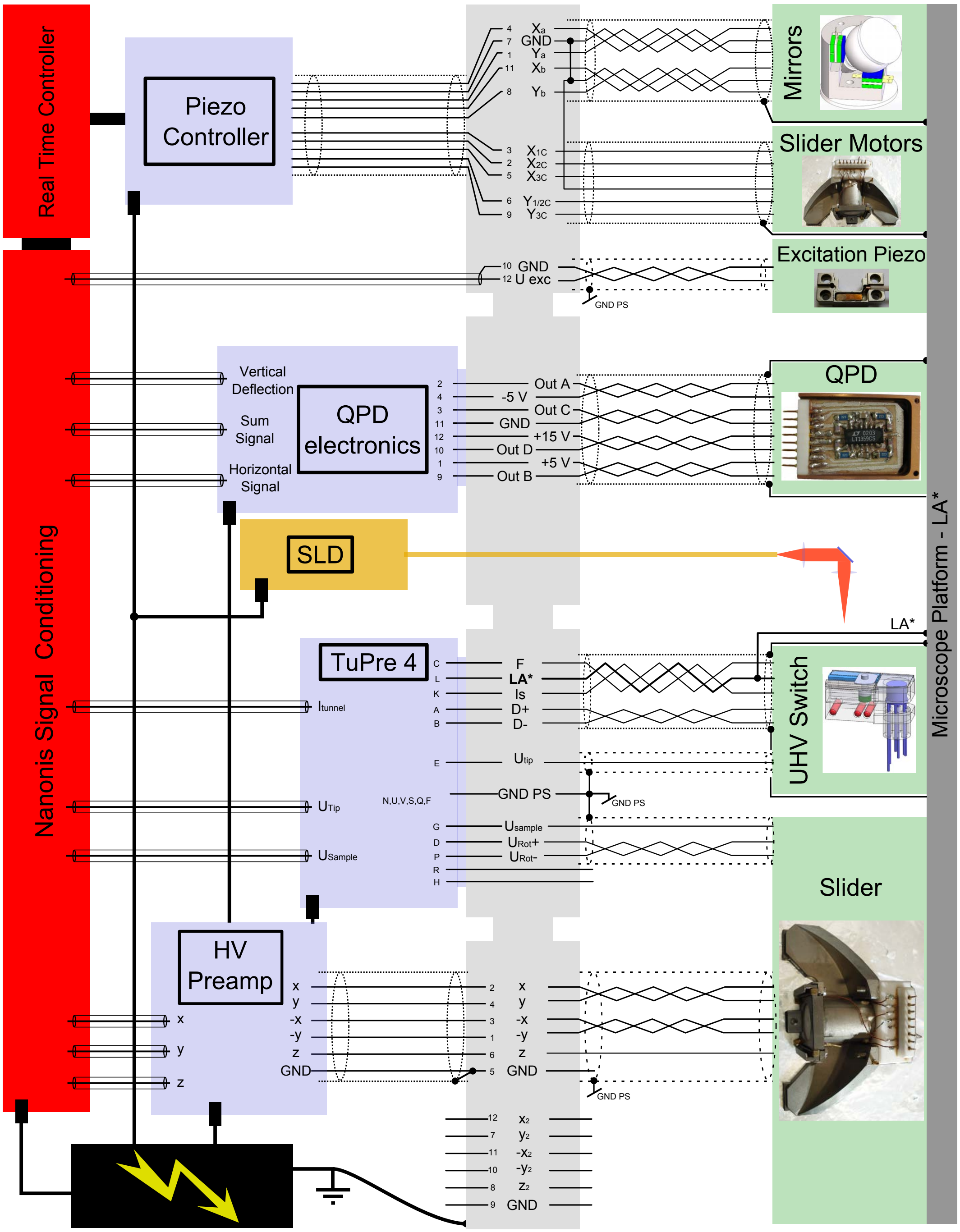

Figure 2.16. Wiring scheme of the microscope. The left side (ambient side) shows the commercial available Nanonis electronics in red and the home built electronics for analog signal conditioning and driving the piezos in blue. The 4 gray blocks in the middle symbolize the DN 40 CF flanges on the bottom of the microscope chamber. The right side (vacuum side) shows the connections to the different parts of the microscope.

and current on the power supply lines are small, so no essential currents should be induced in the shield. The piezo motors moving the mirrors and slider, are not used during the measurements, so these connections do not induce compensating currents on LA* neither. Noise free signal lines are required because the motors would produce mechanical disturbance otherwise. The UHV switch and transistor are also shielded with the clean LA* ground, which is also fine because it is a very stable system with no bigger voltages and oscillations on the lines and the bandwidth is quite small. LA* is the ground which is grounding the gate of one FET transistor of the cascode circuit and therefore originating from the TuPre-4. This ground was designed to be very clean because it directly affects the measurement of the tunnel current and would make a precise measurement impossible otherwise.

The other shields of electrical lines between the flanges on the UHV side and the corresponding device are grounded with a ground that is also provided from the TuPre-4. It is connected to LA* but with resistors between reducing effects of compensating currents flowing on the ground called GND PS. Depending on the scan range, large voltages changes can be applied to the tube piezo while scanning. The additional connections to the sample for running the rotator are very close to the x contacts of the piezo tube. The sample and tip bias lines have oscillating voltages in the range of 1 MHz when doing KPFM. The piezo for tip actuation is often driven at frequencies around 1.5 MHz when using the Nanosensor PPP-NCL cantilevers and working on the torsional or the second flexural mode for example. For these reasons, these lines are shielded with the ground GND PS.

The gold coated fiber is glued to a DN 16 CF flange and electrically connected to the chamber ground.

The wiring scheme of the connectors and the locations at the cluster flange on the bottom of the microscope chamber can be looked up in the appendix 6.1.

2.3 Ultra-High Vacuum Chamber

The microscope is mounted to a big chamber that was used for a Park AFM and a home built AFM with an integrated time of flight analyzer [55] before. The Park AFM was removed to make space for the new microscope. A CAD drawing and two photos are shown in Fig. 2.17. All the manipulators, except for the manipulator at the load lock chamber which could be reused, were replaced to enable the usage of the Omicron sample plates and to adapt to the new requirements. The manipulator at the load lock was modified to allow transferring three sample plates at a time to the vacuum. The path of a sample can be followed in Fig. 2.17(a): when the valve between lock and the main chamber is opened, the samples or tips are moved with manipulator 1 from the load lock (green) into the main chamber (gray) and can there be picked up with the tall manipulator 2. This manipulator moves the sample to the carousel attached at manipulator 3 with its 6 slots, from where it can be transferred to the preparation chamber (yellow) with manipulator 4 or to the SPM chamber (red) and to the microscope with the wobble stick 5.

The load lock is where a sample or tip is introduced to the vacuum. It is pumped by a turbo molecular pump and its backing pump to a pressure of typically 10^{-7} mBar to protect the main chamber of strong pollution when opening the connecting

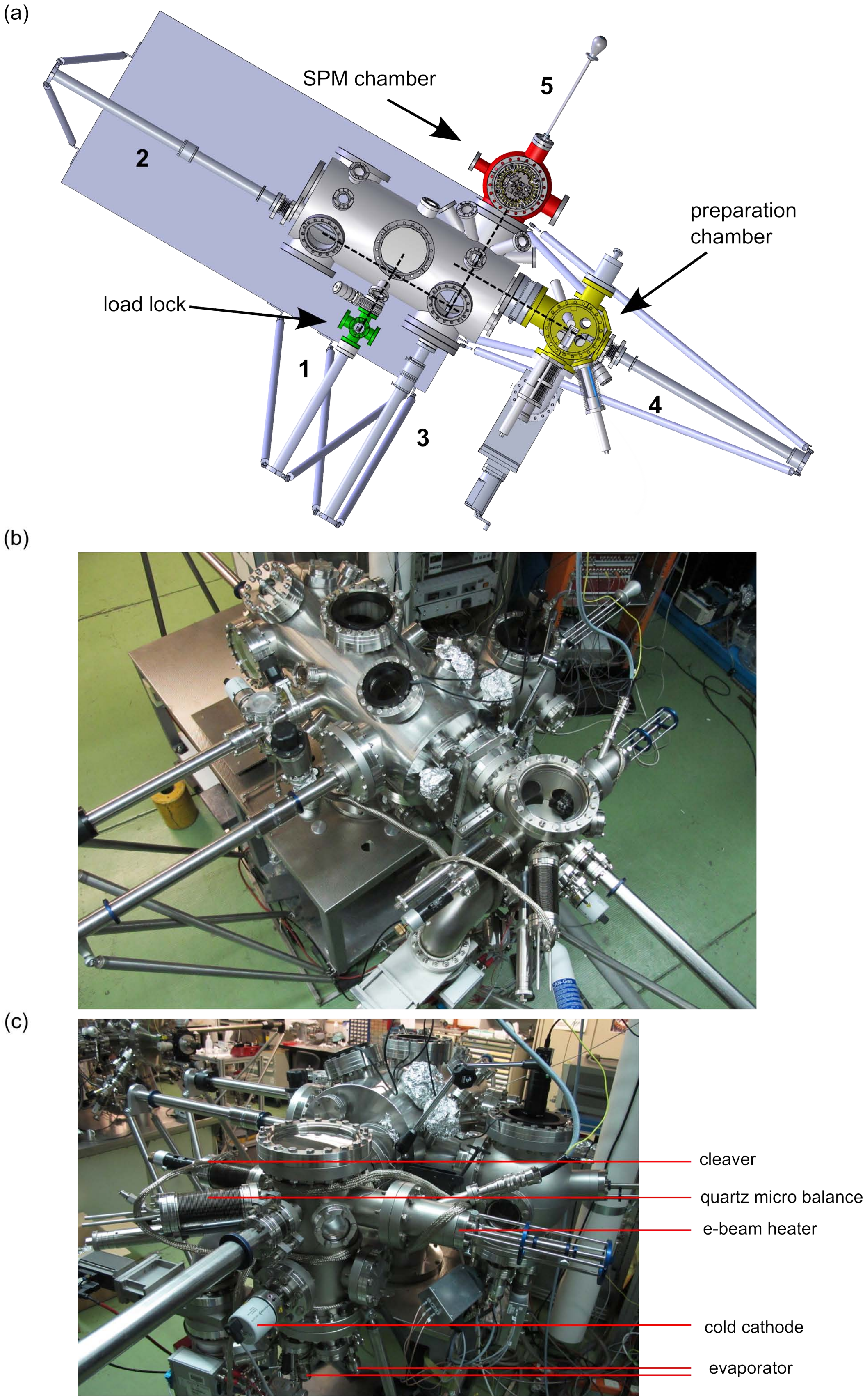

Figure 2.17. CAD drawing in a) and photos in (b) and (c) of the UHV chamber. The path of the sample is marked with the dashed line.

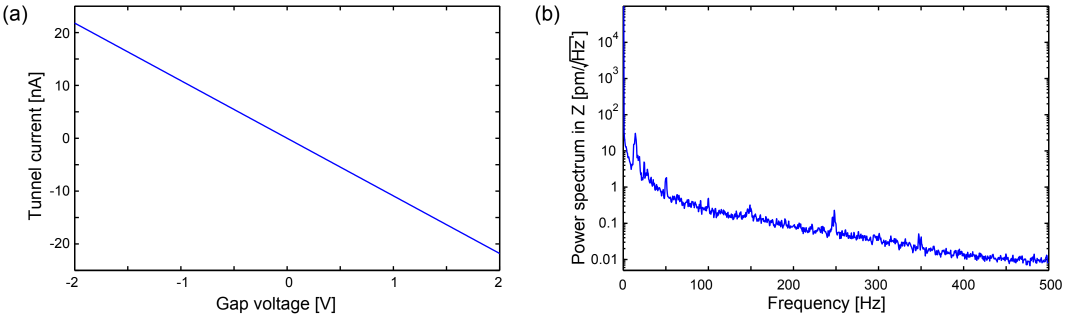

Figure 2.18. Calibration curve (a) and noise spectrum (b) of the STM tested with a Pt/Ir tip on HOPG.

valve. The main chamber is connected to the SPM chamber and separated with a valve from the *preparation chamber* (p-chamber). It is pumped by a *titanium sublimation pump* (TSP) and an ion getter pump. When pumping from ambient conditions, it has to be done over the load lock or the p-chamber. The p-chamber is pumped by a HiPace 300 turbo molecular pump from Pfeiffer with another valve between the pump and the chamber. The pressure in the p-chamber is measured with a cold cathode as it is in the load lock, a Bayard-Alpert ionization gauge is used in the main chamber. After baking the whole system, the base pressure in the main chamber, SPM chamber and p-chamber is about 10^{-10} mBar.

Except for the table carrying the whole system, the heaters for bake out, the ion gauge, the complete load lock and main chamber, the ion getter pump and the TSP, the complete system is new except for a few parts that were on stock and reused (mainly blind flanges, windows and the evaporators). Beside the new manipulators 2, 3, 4 and 5 in Fig. 2.17(a), the p-chamber with the e-beam heater, cleaver, quartz micro balance, the cold cathode, the valve to the main chamber and the turbo pump are new, the evaporators and two linear translators and the pneumatic valve between turbo pump and chamber were reused. All the manipulators and the p-chamber are stabilized and secured by the bars going to the base of the table. Finally, of course, the microscope chamber with all it's contents is new.

2.4 Noise Level and Performance Tests

In this section, some first tests are presented to get an impression of the microscopes performance. All tests were done in UHV with a base pressure of around 10^{-10} mBar. The STM is only briefly characterized, the main focus is on the AFM. There are very sophisticated methods for testing the performance of an AFM, but due to the fact that still some very important improvements have to be done, only a basic noise characterization and drift measurements are shown here. Some problems with mechanical noise around 20 Hz were present in the microscope, which was analyzed and found to be in connection with the table where the whole chamber is mounted and the mounting of the single mode fiber. These problems will be fixed in the course of the next maintenance works and then a detailed characterization of the microscopes performance can be done.

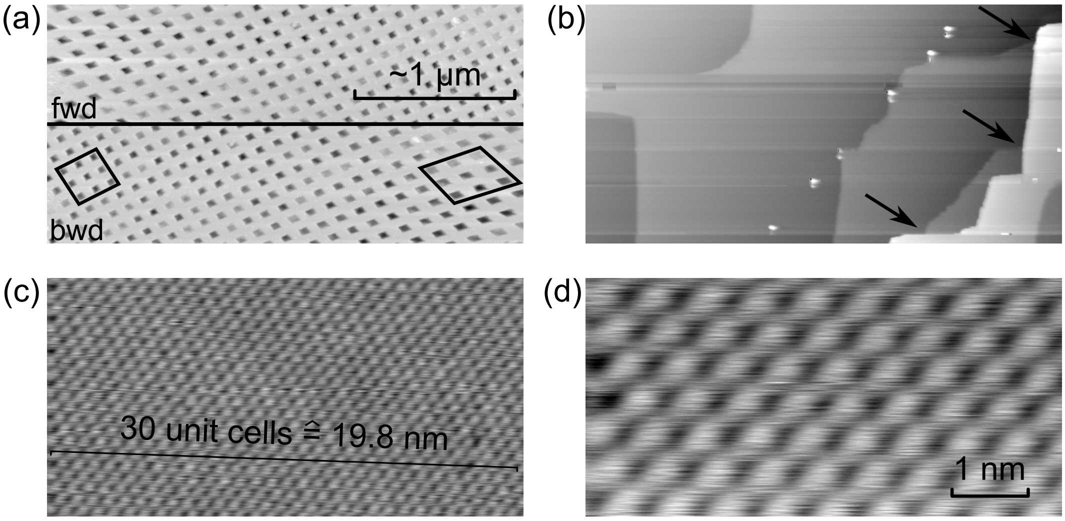

Figure 2.19. Topographic images of nc-AFM measurement for the calibration of the scanner: in (a) on a commercial calibration grid (Nanosensor 2D200 calibration standard), images (b), (c) and (d) are made on a KBr(100) single crystal from Mateck. The arrows in (b) are pointing at the positions, where a step edge splits up into two smaller ones.

2.4.1 STM Calibration and Test

For testing the STM preamplifier, a 10 GΩ resistor is mounted between tip and sample mimicking a tunnel barrier. The response of the signal is measured when a bias is applied to the sample. First, the offset of the amplifier on the TuPre-4 electronics can be tuned that the current is 0 A at 0 V bias. The linear response of the tunnel preamplifier can be verified with the Ohm's law $\mathrm{I}=\frac{\mathrm{U}}{\mathrm{R}}$. With the 100 MΩ resistor in the circuit for IV conversion, a signal of 10 $\frac{\mathrm{nA}}{\mathrm{V}}$ is expected. The measurement with the test resistor shows 10.9 $\frac{\mathrm{nA}}{\mathrm{V}}$ which is almost in the 5 % range of the error of the test resistor.

For the noise tests, a self-made Pt/Ir tip was in tunnel distance with a *highly ordered pyrolytic graphite* (HOPG) surface. The HOPG was cleaved in ambient conditions and then transfered to the vacuum. Imaging with atomic contrast was not possible with the used tip and surface, probably a graphite flake was picked up at the tip making the imaging very unstable. The measurement of biggest interest concerning the STM function of the microscope, was the noise spectrum. In the old microscope, the 50 Hz noise due to the big loop of the tunnel line, is disturbing the measurement as much that it was not used at all. In the noise spectrum recorded on HOPG, the 50 Hz peak is suppressed quite well. A bigger problem is the peak at about 20 Hz which will be discussed in the AFM section.

2.4.2 AFM Calibration and Performance Tests

The tests of the AFM were done on KBr after a rough calibration with a calibration grid. The problems with the measurements on the calibration grid in Fig. 2.19(a) are, that the structures with a periodicity of 200 nm require a large scan area. Comparing the topography images of *forward* (fwd) and *backward* (bwd) scan, essential

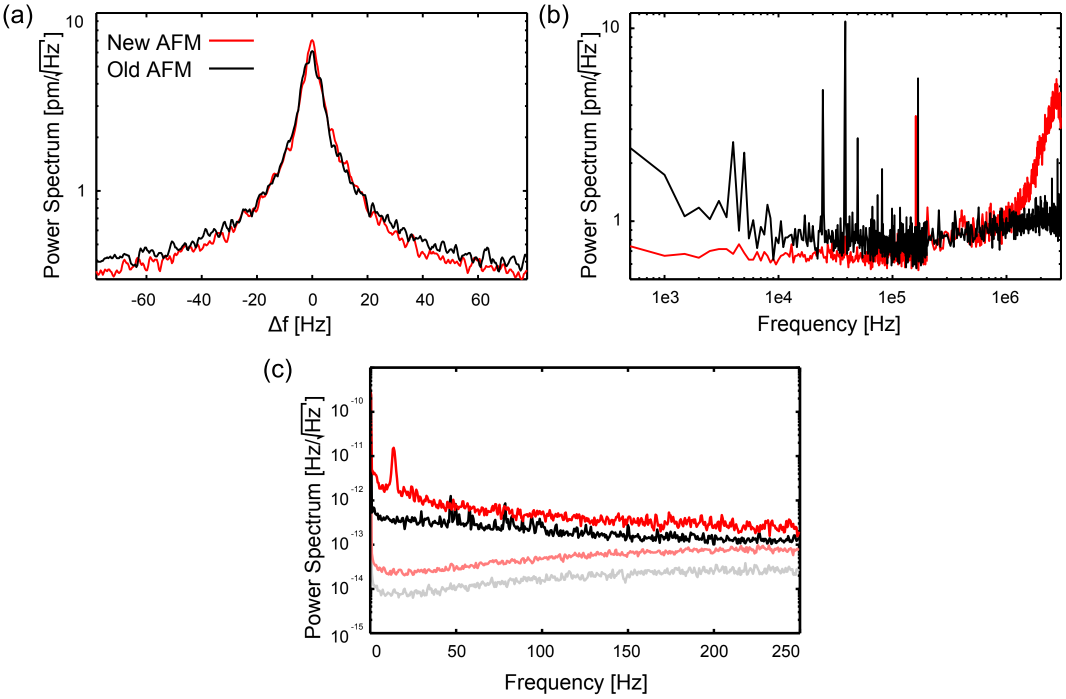

Figure 2.20. Thermal noise spectrum (a) around the first flexural mode with f = 160'239 Hz for the cantilever in the new AFM and f = 167'524 Hz for the cantilever on the old microscope. The Q factors are both in the range of 32'750. The noise in the height z is shown in (b). The frequency noise measured with the PLL of the Nanonis system is plotted in (c). The pale graphs are measured when the tip was retracted from the surface.

creep and hysteresis effects are seen on large scan areas in the range of micrometers. Because the microscope is intended to be used for high resolution imaging on atomic and molecular scales where these effects can mostly be ignored, the scanner was finally calibrated with frequency modulated *non-contact* (nc) AFM measurements of the atomic structure on KBr (Fig. 2.19(c),(d)). In contrast to contact mode measurements, both scan orientations along the scanners x and y direction can be used whereby drift influence can be minimized. The crystal was cleaved in-situ with the UHV cleaver and subsequently annealed to reduce a surface charging. The calibration of z was done with multiple steps that could unambiguously be attributed to a certain number of steps. It helps identifying the number of steps, if a multiple step is suddenly splitting up in two smaller steps as seen in the marked locations in Fig. 2.19(b).

The following noise and drift measurements were done simultaneously on both, the old and the new AFM. The measurements were done on a KBr surface which was cleaved before transferring into UHV with annealed but not sputtered cantilevers. Both microscopes were operated with a Nanonis system where some of the measurements were made, others were done with a network analyzer (Hewlett-Packard) and a USB oscilloscope (PicoScope). The measurement of the thermal noise around the resonance frequency of the first flexural mode of PPP-NCL levers (Nanosensors) in Fig. 2.20(a) looks almost the same for the two systems, the difference can be at-

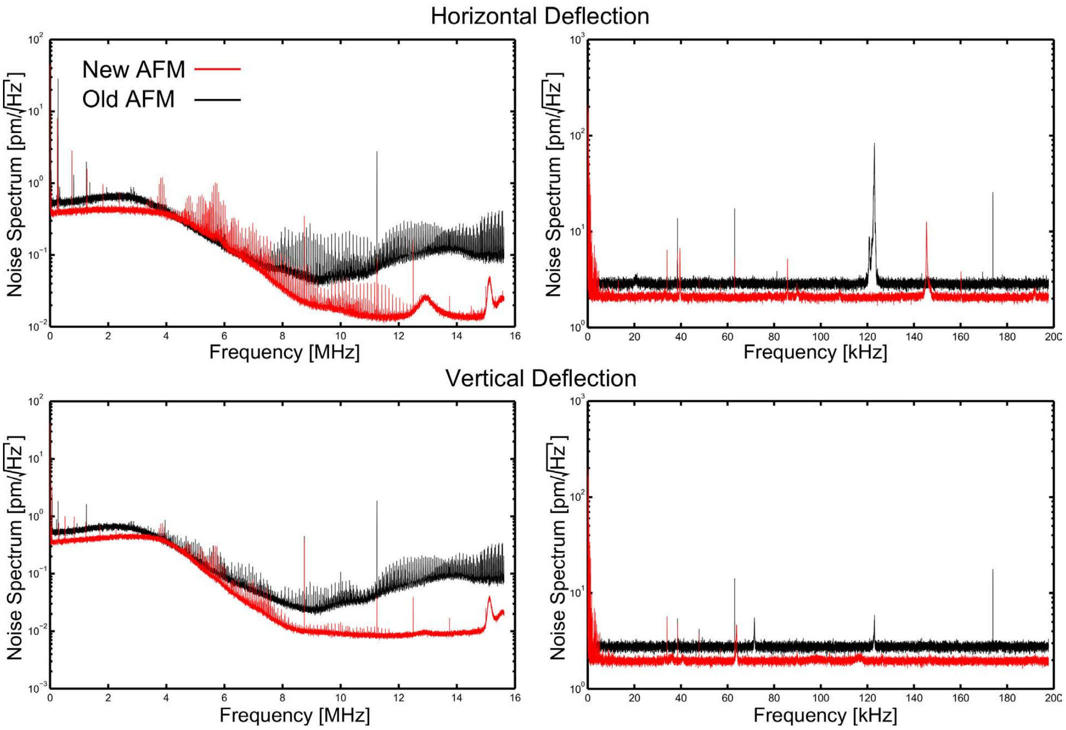
Horizontal Deflection

Vertical Deflection

Figure 2.21. Noise spectra recorded in contact mode on both microscopes.

tributed to the different quality factor Q of the used cantilevers. The measurement of noise in z when the tips are in contact is shown in 2.20(b). A slightly lower noise level is observed on the new device but approaching the 3 MHz, the new electronics shows an elevation in the amplification behavior of the vertical and horizontal signals which is transferred to the z channel. The frequency noise in 2.20(c) however, is larger compared to the old microscope. There is a prominent peak around 20 Hz on the new microscope which is not present when the tip is retracted from the surface (pale colored plots). This is an indication for a mechanical induced noise. Since it is not present when the tip is retracted, the oscillations are not on the beam deflection system but between the sample surface and the tip. Therefore it could originate from a noise in the z piezo, the slider motors or an oscillation of the mechanical path between optical system (i.e. tip) and the sample. There are indications for a mechanical origin (i.e. not piezo induced), namely a very strong sensitivity of the noise when the fiber is touched and therefore vibrating, problems at the same frequencies with the previous device in the same vacuum chamber, and the fact that the bearing of the table where the chamber is mounted is strongly influencing the noise level at 20 Hz. Unlike in the new design, the fiber in the old microscope is shielded at the attachment point of the focusing optics preventing oscillations of the otherwise suspended fiber. This should be changed in the next maintenance. In future, the microscope will also be used in the UHV chamber of the old microscope which will reveal, if the table and the whole UHV system is causing the oscillations. Imaging on the atomic scale with nc-AFM is very difficult and noisy because of these oscillations.

With contact mode AFM measurements, the 20 Hz noise is not as prominent as in

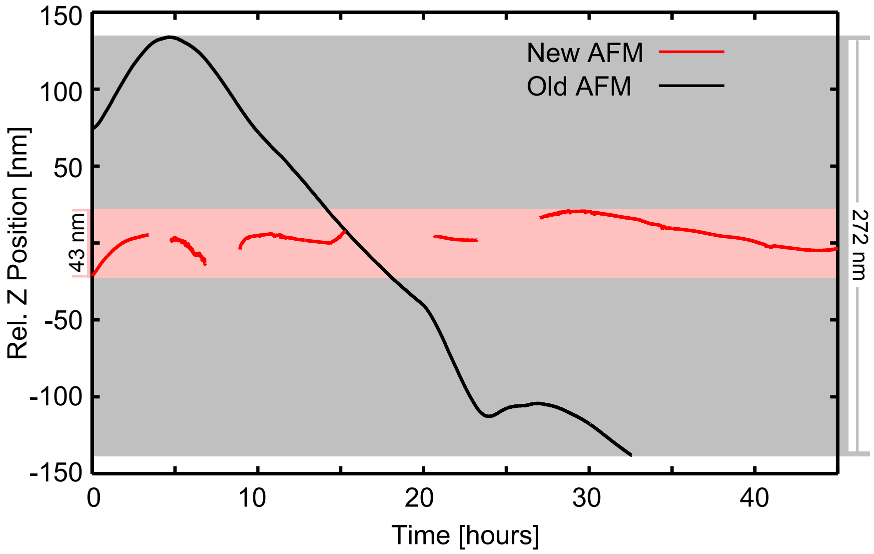

Figure 2.22. Z positions were simultaneously measured for a period of 45 hours on the two microscopes.

the dynamic mode and imaging on flat surfaces is more facile. In the experimental section 3, numerous force maps and other data are presented which give sufficient proof for that. Comparing the noise level of the two systems in Fig. 2.21 mainly shows two important facts: the noise in the new microscope is a factor 2 smaller and the bandwidth is bigger (≈ 4MHz). All the measurements on the new microscope were made with the 678.5 nm wavelength SLD light source of the same type as it is used in the old microscope. Since the sensitivity of the QPD is better at larger wavelength with the maximum between 900 nm and 1000 nm, the other SLD with 830.6 nm should give even better results.

The thermal drift of the microscopes was measured in z direction. Therefore, the tip was approached to the surface and the set point was kept constant for two days. To avoid the influence of the drifting photodiode which directly influences the z position in contact measurements, frequency modulated nc-AFM was used. As seen in Fig. 2.22, the movement in z is recorded over 45 hours. When the measurements started, the temperatures in Basel were over 35 °C and dropped to about 15 °C within the first 10 hours which caused a large drift on the old microscope but surprising little drift on the new one. After 33 hours, the surface drifted out of the scan range in the old microscope and it did not drift back into the measurable area until the end of the measurement. The gaps in the data of the new microscope are due to some problems with the software which caused the tip to retract a few times. The new microscope drifted in a range of only 43 nm within the 45 hours, the old microscope drifted 272 nm in 33 hours and probably kept drifting further. The thermal stability is much better on the new microscope with a factor of (at least) 6.3 less drift along z direction over the measured period.

2.4.3 Summary

Additional electrical connections provide additional functionality. For the measurements presented later, a sample rotator was run with the two new electrical connections at the sample holder on the scanner. Connections for an 8 segment scanner are available for a further increased scan range, the described 4 segment scanner has already a 5 times larger scan range than the old microscope. Beside the additional electrical connections which are available, there are connections for two PT100 temperature sensors and a laser driver with adjustable output current. The PT100 readout and the laser driver is implemented in the electronics for the signal processing of the QPD signals. Newly, the gains of the preamplification of horizontal and vertical signal can directly be set through the Nanonis user interface. For a future upgrade, the feedthrough for an additional fiber guide is available. A multimode fiber can be mounted with an optics attached on the bottom side of the microscope for optically actuating the sample surface. A notch in the microscope body was made to make space for its beam path. With KPFM the charge distribution in a molecule can be mapped [56] and therefore the change in electronic properties under optical actuation can be investigated.

The modularity should be improved in order to reduce maintenance times. The piezo motor for the movement of the slider is one single module compared to the three single piezo stacks of the old microscope. The slider could be replaced very easily as well as the mirror motors, the cantilever holder with the piezo actuator, the optics for focusing the beam of the SLD and the QPD module.

The wiring was optimized to provide little noise, good electrical contacts, more connections and the design of the tunnel line was changed to avoid the big loop which induces a large 50 Hz noise. The diameter of the cables is smaller to reduce the thermal contact through the electrical connections.

The operation of the microscope is more facile because more tasks can be remotely done over the computer with the user interface (coarse motion of the slider, motion of the mirrors, gain selection of the deflection signals, optical image from the digital camera). Also the transfer of samples is easier, the manipulations with the wobble stick are much easier and less dangerous for the fiber. The UHV switch offers a facile use and more reliable solution compared to the old one.

With the new platform, the thermal stability has strongly improved, to which extent the mechanical stability has changed is difficult to say at the moment. As suggested by FEM simulations, the eigenresonance of the platform has shifted slightly to a higher frequency (roughly 350 Hz).

Logic takes care of itself; all we have to do is to look and see how it does it.

Ludwig Wittgenstein

Chapter 3

Angle Dependence of Friction on the Atomic Scale

The experimental measurement of friction anisotropy on the atomic scale is a delicate thing. There are only few works in literature presenting conclusive and clear experimental evidence for friction anisotropy originating from the atomic (or molecular) scale [20, 23, 25, 28–30]. These experimental works were either done with a specially designed device [20], only along two orientations [25], the investigated surface consisted of domains with different orientations that can be compared directly [28, 29], or the method was adopted to see only relative changes of friction [23, 30]. NaCl, a well known material in nanotribology, and BNL, a material that will soon be described in detail, were investigated with the new microscope using the rotatable sample holder to investigate orientation dependence of friction on atomic scale. NaCl is a relatively simple system for the investigation, both, from the experimental and theoretical point of view. Big single crystals are commercially available and atomically flat surfaces can be obtained by cleaving, ideally in UHV. Calculations on the base of the Prandtl-Tomlinson (PT) model using simple sinusoidal potentials showed, that the phenomenological model gives satisfying results reproducing the experimental findings. BNL on the other hand, is an unknown material in the field of tribology and offers a special surface which is very regular and well ordered, but yet anisotropic. Friction anisotropy, if measurable by means of FFM, can be expected to be quite large.

3.1 Experimental Methods

For the experiments, PointProbe® Plus Contact Mode levers from NANOSENSORS™ were used, which have typically a normal flexural force constant of 0.1 N/m, resonance frequencies around 15 kHz and in UHV rather large Q factors of up to 10^6.

This becomes a problem when the sample is approached to the tip. The coarse motion of the slider produces vibrations on the microscope platform which induce large oscillations of the cantilever. When approaching, the slider is moved about 1 μm at a time which requires about 6 steps with 100 V on the piezo motors. This can produce an oscillation of the lever with amplitudes of 100 nm and more. Given a resonance frequency of 15 kHz and a Q factor of 10^6, it takes minutes until the cantilevers oscillation reduces to an amplitude of less than 10 nm. In order to protect the tip from a violent crash to the surface, this oscillation is actively damped using the PLL of the Nanonis OC4 station before the force feedback is turned on and the tip approaches to the surface. The sample approach is finally a repetition of moving the slider, damping the oscillation and approaching with the scanner using the force feedback, until the set point of the regulating system is reached.

For friction measurements along different orientations on the crystal, the sample has to be rotated after the measurements in one direction. Ideally, the measurements would be performed in the exact rotation center on the sample. The tip could then stay on the surface while rotating, the tip condition might be very stable when it always stays in contact with the surface and no extreme forces are acting on the interface. Unfortunately, this is very difficult to realize, especially when the slider can only be moved horizontally and not vertically, which reduces the scannable area in the vertical direction on the sample to the 4 μm scan range along the y axis of the scanner. As long as the tip is not at the center of rotation, the surface is moving below the tip when the rotator is in use. If the sample is extremely flat and steps very small, it is possible to leave the tip on the surface during sample rotation, though the speed of the tip sliding over the surface can exceed the normal scan speeds by far and tip changes can be very severe. In reality, the risk to damage the tip is too high and therefore it was always retracted during the sample rotation.

A quantitative analysis of friction anisotropy is a tricky task in the experiment. Relatively good results are reached on *self-assembled monolayer*'s (SAM), when they appear in domains with different orientations on a surface [28, 29, 57]. The friction values of different orientations of the SAM can be compared directly within a single measurement. The relative change in friction between different orientations is directly measured while no significant changes in the contacting area have to be accounted for. No bigger changes in the interface can be expected, when it is not necessary to retract the tip from the surface which applies for measurements that were done with the unique sensor called tribolever [20, 21]. The advantage with this probe is that lateral forces in all directions can be calibrated and measured, sparing a sample rotation. A quite new method called transverse shear microscopy is showing nice results [30–32] and allows the measurement of friction anisotropy by AFM without sample rotation, though the interpretation of the data and calibration of the forces is disputable. FFM measurements along various directions are compared in the following, which has the advantage that the lateral forces can directly be measured, but changes in the interface due to the separation and reapproach of the tip to the surface can not be excluded. For very sharp tips, relatively big changes of the interface can be induced by the rearrangement of only few atoms at the apex. This can be observed for example with the different adhesion forces that are measured, when a series of z-spectroscopies is done. The measured adhesion force is also varying because of the thermal movement of the atoms at the interface.

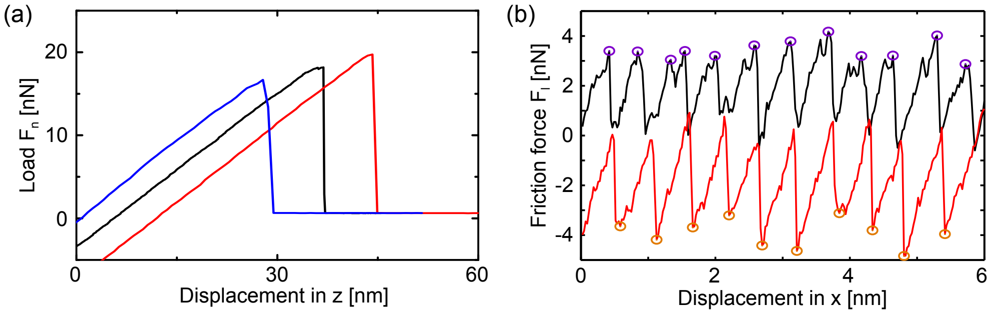

Figure 3.1. In (a) the retraction curves of 3 force-distance curves are shown that were recorded within a period of 5 minutes. The shift in z is done afterwards for illustration. First the black, then the red and in the end the blue curve was recorded. The friction loop in (b) was made along the [100] direction of NaCl(100) with a load of 4.5 nN. The slip positions detected for the calculation of the static friction are marked with circles.

In Fig. 3.1(a) such measurements are shown. The adhesion forces were 16.7 nN, 18.2 nN and 19.7 nN, which is quite stable compared with the variations that occur with other tips, but still it is a change of 15 % in three measurements that were done within 5 minutes. The 3 nN difference on 15 nm displacement corresponds to 1.4 eV energy difference which is equal to the thermal energy of 35 atoms at room temperature. 35 atoms of the NaCl sample are involved on a circular interface with the diameter of 2.8 nm which is in the range of the expected contact area. This rough estimation is suggesting, that thermal vibrations can have substantial contributions on the masured adhesion forces in the presented experiments. These changes can be a problem when friction forces at a given load are compared, because the adhesion is not known during the measurement. In the presented measurements, the normal force is defined as 0 nN for the relaxed position of the cantilever regardless of the adhesion. Therefore, instead of a comparison of friction forces, the friction coefficient μ is calculated out of a series of measurements with different loads for the analysis of the orientation dependence. The coefficient μ could also be extracted from friction spectroscopies [6, 58], but for the qualitative analysis of the friction force maps it is not suited. For the comparison of friction coefficient versus sample orientation, the normal force $F_{n,i}$ of a scan line is calculated as

$$F_{n,i} = \frac{1}{N}\sum_{j=1}^{N} F_n(i,j) = \langle F_{n,i} \rangle \,, \tag{3.1}$$

with the coordinates (i, j) of the data points in a measurement and N the number of points j in a row. The corresponding lateral force $F_{l,i}$ is the difference between the mean friction of forward minus backward direction of the line i

$$F_{l,i} = \frac{1}{2}\left(\frac{1}{N}\sum_{j=1}^{N} F_l^{fwd}(i,j) - \frac{1}{N}\sum_{j=1}^{N} F_l^{bwd}(i,j)\right) = \frac{\left\langle F_{l,i}^{fwd}\right\rangle - \left\langle F_{l,i}^{bwd}\right\rangle}{2}. \tag{3.2}$$

These values were calculated for all the lines of a measurement which was performed with the feedback system enabled, so the values of $F_{n,i}$ should not vary much within a measurement. The measurement though were made with extremely small proportional and integral gains of the z feedback, in order to not be sensitive to the buckling

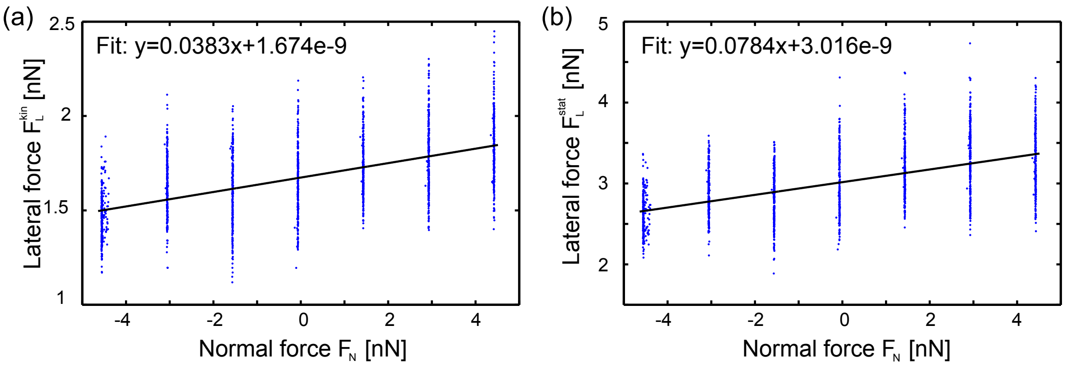

Figure 3.2. Kinetic (a) and static (b) friction values of the lines in a measurement series done along the [100] direction of NaCl(100). The slope of the linear fit corresponds to the friction coefficient, $\mu_{kin} = 0.0383$ and $\mu_{stat} = 0.0784$.

of the cantilever, but the gains should be just big enough to compensate the drift in z direction to keep the load close to the set point. A careful selection of these gains is allowing a measurement that is practically a drift compensated constant height measurement. For the calculation of the kinetic friction $F_{l,i}^{kin}$, the mean over all values of a line is taken, whereas the calculation of the static friction requires the detection of the forces just before the slips occur. This can be a difficult task for a noisy measurement. It was realized with a Matlab program that is checking every points in every line for a drop of lateral force which is bigger than a threshold value. The threshold has to be tuned very well for every measurement in order to find small slips but at the same time, noise or other features that should not be interpreted as slips need to be ignored. The static friction $F_{l,i}^{stat}$ is then calculated with the friction force values that were found by this program. An example of a loop with the detected slip positions is shown in Fig. 3.1(b).

For the evaluation of friction coefficients as a function of rotation angle, the measurements were performed only in a range of wear-free sliding. For every measured crystal orientation, a series of measurements with different loads was performed to finally calculate μ out of the slope of the linear fit through the data points. Such a measurement along the [100] direction is seen in Fig. 3.2. Both, kinetic and static friction show that the increase of friction on the used range of loads is quite small regarding the wide spread of up to 1 nN of the data points at a fixed load. The friction coefficient μ, describing the linear relation of friction force and normal force

$$F_l = \mu F_n, \tag{3.3}$$

does not always apply for single asperity contacts. With the well known continuum mechanic models like the Hertz, JKR or DMT models, the contact radius, Young moduli and Poisson numbers are necessary values for the evaluation of friction and they all end up in a proportionality of $F_l \propto F_n^{\frac{2}{3}}$. It was shown, that the JKR model applies best for the measurement on NaCl [6], and there it can also be seen, that the range of normal forces applied is very high compared to the forces used in this work. It was very important to use small forces to maintain a very sharp tip and avoid essential changes of the interface. In the used range of forces, the non-linearity can hardly be seen. The tip radius can not be determined exactly, the manufacturer state that it is smaller than 10 nm and changes during the measurement can not be measured up to now. Of course, a new effective friction coefficient for point-contact-like single-asperity friction for a JKR type contact could be introduced as proposed for the Hertz model [59] but still, the measurements are in a linear regime which was described before [14] and explained by means of the PT model by the linear increase of the energy barrier E_0 preventing the tip from slipping to the next potential minimum. The focus of this investigation is fully set to the relative changes in friction when the sample orientation is changed, and therefore the sliding direction in respect to the crystal orientation. All the measurements that will be compared were made with one tip, and therefore only small changes of contact area and the sliding interface can be assumed.

The vertical and horizontal deflection signals are used to calculate the normal and lateral forces using the Hooke's law $F = -kx$. On the other hand, the displacement of the tip along x and y direction can be calculated from the force maps using the same relation. Assuming the situation when the tip is pinned to the sample surface, a linear increase of the lateral force signal is measured when the scanner is moving uniformly. In the measurements this happens in the sticking phase between two slips. The x and y coordinates of the tip (x_{tip}, y_{tip}) are determined as

$$x_{tip} = -\left(\frac{1}{k_{lat,x}} F_{lat,x} - x_{sup}\right) \; and \; y_{tip} = -\left(\frac{1}{k_{lat,y}} F_{lat,y} - y_{sup}\right), \tag{3.4}$$

with the support positions x_{sup} and y_{sup}, the lateral spring constants $k_{lat,x}$ and $k_{lat,y}$ and the measured forces $F_{lat,x}$ and $F_{lat,y}$. The support positions are well known, the lateral spring constant along x can be determined with the slope of the sticking phase in the friction loop, which is also called the experimental lateral spring constant k_{exp} as described in [47], which was determined to be 10.1 N m^{-1} (see Fig. 3.7). The effective spring constant k_{eff} is the result of the spring of the cantilever in series with the lateral spring of the contact and can be calculated form k_{exp}. k_{eff} and k_{exp} are dominated by the contact stiffness since it is much softer than the torsional spring constant of the cantilever. Assuming an isotropic contact stiffness, $k_{lat,y}$ is known. Another assumption that has to be made, is concerning the $F_{lat,y}$. The vertical deflection is used to determine the normal deflection of the cantilever, but the stick slip movement also produces the so called buckling of the lever which is the result of the lateral movement along y. Under the assumption, that the deflection of the cantilever due to the atomic corrugation of the substrate can be neglected, the vertical signal can be used to calculate the movement along the y direction.

3.2 Friction Anisotropy on NaCl

3.2.1 Numerical Calculations Using an Ab Initio Calculated Potential

The interaction between the probing tip and the NaCl surface is described by the potential $V_{NaCl}(x, y)$. In the past, calculations were presented using the potential

$$V_{NaCl}(x, y) = -\frac{E_0}{2} \cos\left(\frac{2\pi}{a} x\right) \cos\left(\frac{2\pi}{a} y\right), \tag{3.5}$$

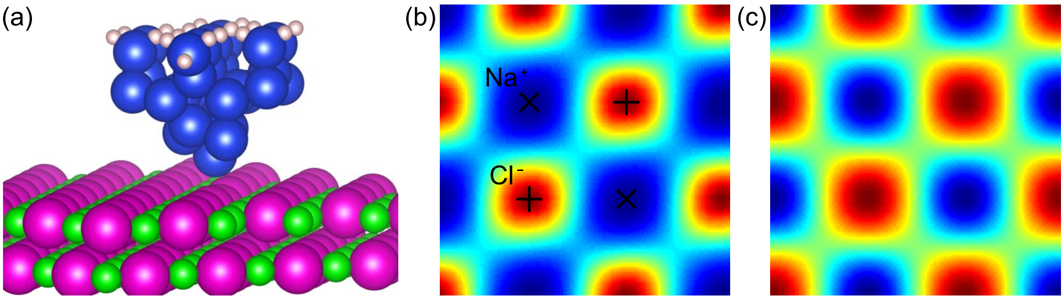

Figure 3.3. (a) is an illustration of the tip and surface that was used for the DFT calculations. In (b) the resulting potential energy at 3 Å separation and in (c) the sinusoidal potential as described in eq. 3.5 is shown.

with the lattice constant of a = 0.56 nm, which fulfills the expected geometrical properties of the system. The selection of the sinusoidal potential was not the subject of bigger debates since it explained many aspects of experimental data quite well. Measurements with nc-AFM [60] have shown that the interaction potential can be described this way for the measured tip sample separations. With very small tip-sample separations however, chemical interactions affect the structure of the force field and need to be accounted to provide an accurate description of the system. In order to take into account the atomic relaxations, one has to exploit atomistic simulations where the atomic cores are allowed to find their relaxed positions once the position of the tip is changed with respect to the surface. For this purpose, the *density functional theory* (DFT) was used as implemented in the BigDFT electronic structure calculations code [61], within the local density approximation and using the Hartwigsen-Goedecker-Hutter pseudo potentials [62]. Because of the large size of the unit cell, the calculations were performed only at the center of the Brillouin Zone. However, it is not feasible to use it on-the-fly at each time step of the PT simulation because of high computational demands. Since not the detailed structures of the tip-apex and sample-surface but only the force on the tip is required, an approximate force field based on DFT can be made replacing the previously used potential in eq. 3.5. The force field as a function of the lateral position of the tip is obtained by bilinear interpolation of the forces calculated by DFT on the points of a grid. At each height, we used a 19 x 19 grid covering a unit cell of the NaCl (001) surface. At each of the grid points, all atoms of the model Si tip and the sample in Fig. 3.3(a) are relaxed except those that are located on the base of the tip and sample. The latter includes one atomic layer on the top of the tip and one on bottom of the sample slab. The base atoms are kept frozen at the atomic positions as in the corresponding bulk. Once the free atoms found their relaxed positions, the sum of forces on the atoms in the tip-base are calculated and considered as the chemical force acting on the tip. The interpolated potential energy for a representative separation of 3 Å is shown in Fig. 3.3(b) and the corresponding sinusoidal potential in Fig. 3.3(c). The reduced symmetry according to the tip asymmetry and the consideration of chemical forces are seen in the resulting potential which clearly deviates from the sinusoidal potential. The PT simulations are made using this potential, the Langevin equation (eq. 1.6) was numerically solved using the Ermak algorithm [18]. For the simulations along different orientations, the scan direction was altered. In other words, the

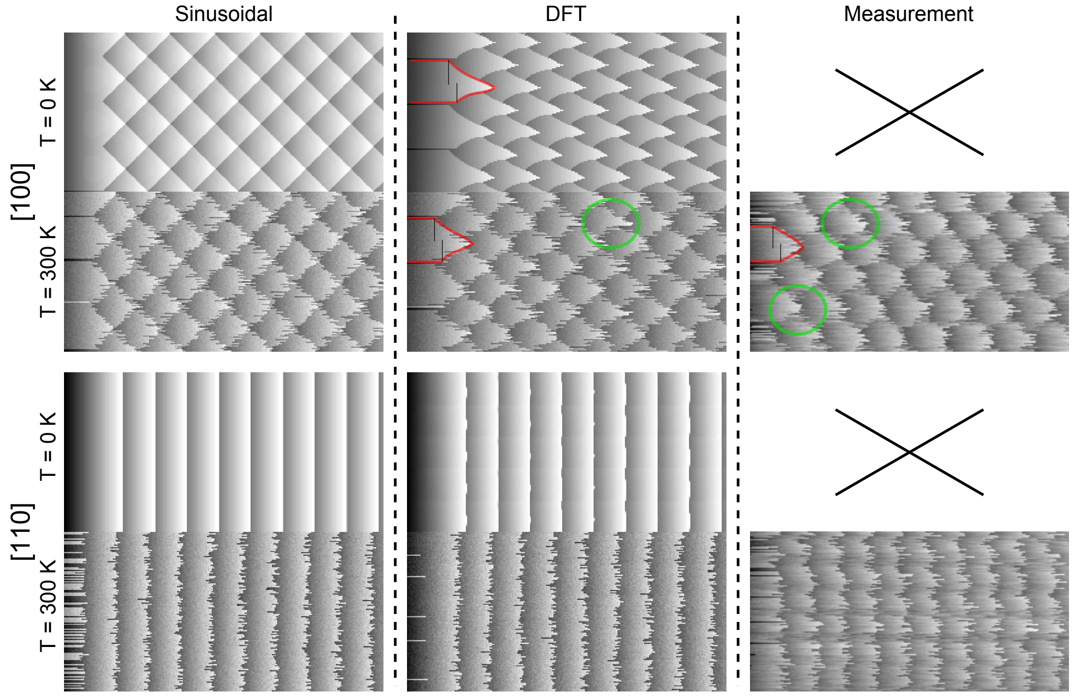

Figure 3.4. Friction force maps from PT simulations with T=0°K (upper part) and T=300°K (lower part) along the the [100] and [110] directions using the sinusoidal potential and the ab initio calculated DFT potential. The measurements are only available for room temperature. The nose like feature is marked in green and the asymmetric feature of the initial slip is drawn in red.

effect of the tip asymmetry to the potential was calculated for one orientation, the potential was then used to do calculations along orientations from 0° to 90°. This can be compared with the situation of the rotation of the scan axis x and y in respect to the tip. In the experimental situation, the scan axis remains constant in respect to the tip but the scan axis x and y in respect to the sample is rotated. To reach the latter situation, the DFT calculations need to be done for every scan orientation which is just too expensive. In the following discussions, the x direction of the scanner is always the fast scan direction and the slow direction therefore y.

A comparison of calculated friction force maps with the sinusoidal and DFT potential, respectively, is shown in Fig. 3.4. On the left hand side, the well known force maps from calculations with the sinusoidal potential can be seen with T=0°K in the upper part, T=300°K in the lower half of the image. Friction diamonds along the [100] and stripes along [110] are the characteristic features. The DFT simulation along [100] reveal a very different pattern at T=0°K, the difference at room temperature is less obvious. The friction diamonds are elongated along the scan direction, especially in the center of the diamonds. This nose-like elongation can still be seen at room temperature as well as in the experiments, though it is easily overlooked or misinterpreted as noise. The distorted friction diamond at the initial sticking part (left side for the forward direction, marked in red) is slightly asymmetric in the measurement as it is in the simulated map from the DFT potential but not in the simulations with the commonly used potential. Along [110] a slight deviation

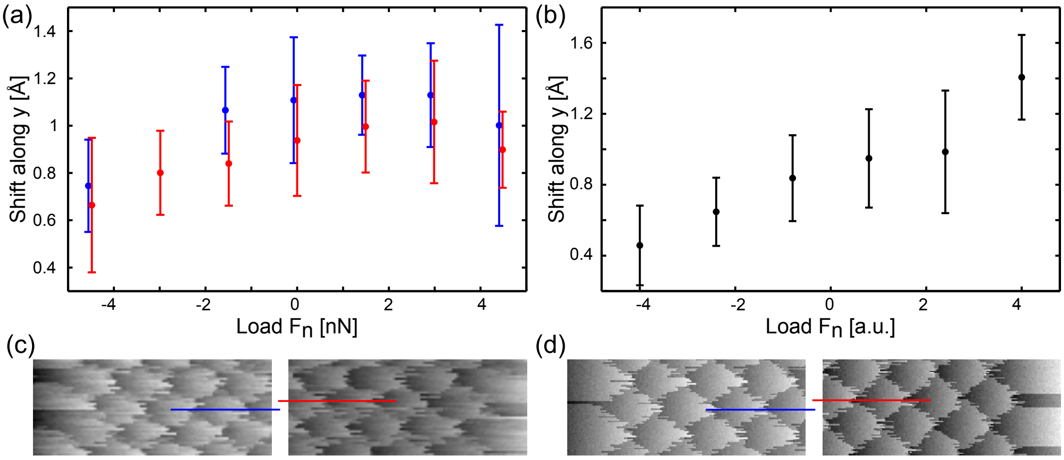

Figure 3.5. The shift of the friction diamonds along the slow scan axis y between forward and backward direction is shown for the measurements (a) and the simulations (b) for different loads along the [100] direction. Two different measured data sets were analyzed in (a), the blue along 0° and the red along 90°. A small section of the forward and backward force map of the measurement (c) and simulation (d) are illustrating this effect.

from the straight lines is seen at T=0°K which is not seen by eye in the simulation including temperature. The measurement shows a much stronger deviation from straight lines, the atomic sites can be recognized. It would be interesting to see, if simulations with a potential using a DFT calculated potential using a NaCl tip could reproduce this contrast more accurately.

Another striking observation that can be made, is a shift of forward compared to the backward friction force map along the slow scan direction. One consequence of this fact is an asymmetry of the forward and backward friction loops. This will be discussed later in section 3.2.3. In Fig. 3.5 the load dependence of this offset is shown for the measurements as well as for the simulations. It is seen, that the shift is growing with an increase of the load, values of more than 1 Å are observed in both, simulation and measurement. This effect is most probably caused by the tip asymmetry. In fact, this break of symmetry can hardly originate from the highly symmetric halide surface, it virtually can only be caused by the structure of the tip. In the simulations based on the sinusoidal potential, the offset is not present. These observations make strong evidence for the good agreement of the newly presented simulations with the measurements explaining some effects that were not discussed yet in the nanotribology community.

3.2.2 Measurements Along Various Directions of NaCl(100)

The measurements in this section were done on the (100) plane of a NaCl single crystal bought from Mateck. The crystal was glued to the round sample plate which is covering the sample rotator. The sample preparation is affected by the use of the rotatable sample holder. The sample can not be cleaved in situ because relatively large forces are acting on the sample and the holder which is problematic for glued samples, they normally break at the base, and most probably it would damage the

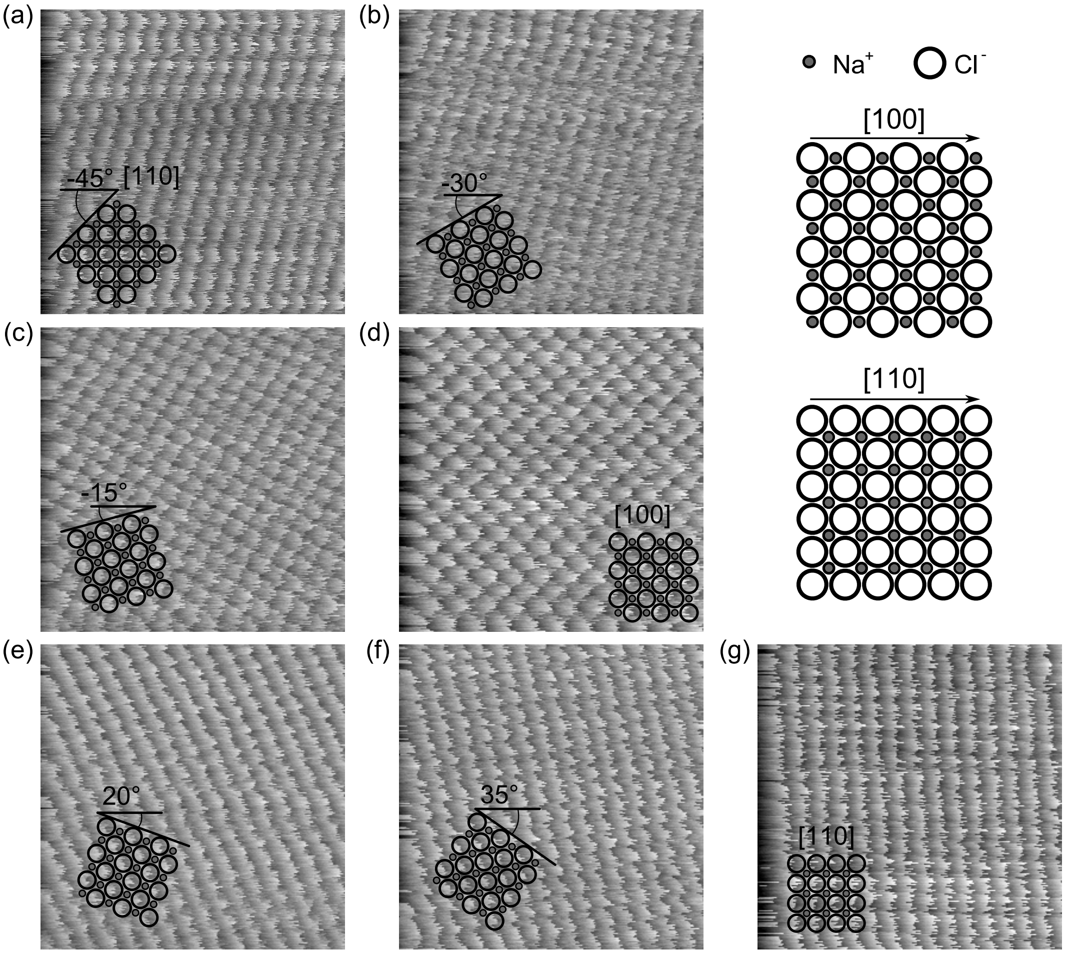

Figure 3.6. Lateral force maps of the forward scan on NaCl along selected orientations. The rotation angles are all in respect to the [100] direction, the rotation was made clockwise. All measurements were done with 0 nN load and with 13 nm/s scan speed.

piezo ceramic parts of the rotator. As a result, the sample was glued and cleaved right before transfer to the load lock where it was directly pumped. After some hours in the load lock, the pressure is smaller that 10^{-6} mBar and the sample can be transfered to the main chamber. The sample is usually annealed in UHV but this is also problematic with the rotator. The glue that was used for the assembly of the rotator is not stable at high temperatures (> 120°C), and when we tested a soft annealing, the magnet holding the round sample plate and the sample fell off. Finally, the sample preparation was simply reduced to the cleaving just before the transfer to vacuum and pumping for some days before starting the measurements.

A selection of measurements are shown along different orientations starting with the fast scan direction along [110] in Fig. 3.6(a) going in 15° steps to the [100] direction in Fig. 3.6(d) and in the following (e)-(f) again to the [110] orientation. Because of the 90° rotation symmetry of the cubic lattice of the NaCl crystal, it is sufficient to investigate the friction along 90 degrees. In literature, the [100] orientation was intensively investigated and friction maps like in Fig. 3.6(d) are well known with the typical friction diamonds with the periodicity of the lattice constant of NaCl. Thus,

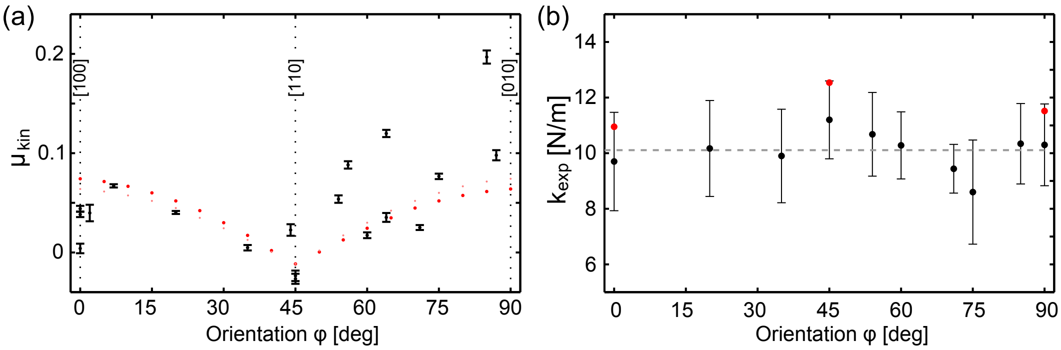

Figure 3.7. In (a) the friction coefficients μ_{kin} are plotted for different sliding directions on the NaCl crystal. The red points are the values (a.u.) extracted from the PT simulations using the corrugation potential from the DFT calculations. The measured stiffness k_{exp} as a function of orientation is plotted in (c), the red points are k_{eff}.

only one ionic species is 'seen' in the measurement, whether the tip sticks at the Na^+ or Cl^- position is often not known. Simulations using a NaCl tip have shown that the attractive forces at different positions over the surface strongly depend on the ionic species at the tip apex [63]. Therefore the Na^+ terminated tip would stick over the Cl^- sites and vice versa. The silicon tip used in the experiment can be covered in the course of scanning on the halide. According to the simulations introduced in section 3.2.1, the bare silicon tip would be sticking at the positions of the Na^+ atoms. The characteristic FFM contrast is getting lost the more the sliding orientation deviates from the [100] orientation. The contrast is getting weaker, especially along the slow scan direction. This is seen in Fig. 3.6(a)-(c),(e)-(g). Along the [110] direction, only vertical stripes are seen corresponding to the atomic stick slip motion of the tip, the contrast along the slow scan direction is very weak. For the determination of the orientation, the crystal axis with the smallest angle to the fast scan direction was used, because it is least affected by thermal drift.

These measurements demonstrate that the sample rotator works nicely. For the rotation of 1°, about 100 steps with an amplitude of 60 V on the piezos are necessary. The data presented in the following were all made with the same cantilever with a resonance frequency of 15'779 Hz, a normal stiffness of $k_N = 0.39$ N/m and lateral stiffness of $k_T = 246.8$ N/m. The measurements were started along the [110] direction referred as -45°. The well known [100] direction is therefore also referred as 0°. Measurements were done from -45° to 135°, since NaCl has a 90° rotation symmetry, the orientations exceeding [0°,90°] can be projected to this interval. This is valid as long as the sample is rotated and the scan direction is fixed relative to the cantilever (and therefore the tip), which is the case in the measurement. The simulations on the other hand, were made with a DFT potential calculated for one tip sample configuration and then the scan direction was changed. This is resulting in the situation of a resting surface and a changed scan direction in respect to the tip. Slightly different results could be expected for the simulations when the potential would be calculated for every tip sample configuration but the computational cost would be immense.

The results of the measured angle dependence of the friction coefficient are shown in Fig. 3.7. The same analysis was done with the data from the PT simulations using the DFT potential, which is represented by the red data points in the figure. As proposed in literature [25, 26], friction should be smallest along [110] and rise towards [100]. The behavior of the μ_{kin} from the simulation has the same angle dependence as the friction values that were found by *Steiner et al.* [26], here it is shown that this behavior also applies for the coefficient. The experimental data are following this trend. The error bars drawn here, are the standard error from the fit trough the data points and can not be regarded as the true error range. The accuracy of the values is limited because of the very narrow range of loads that were applied, this leads also to the negative values that were measured at 45°. The data from the experiment is in agreement with the simulation. The values of the measured contact stiffness are found to be constant in the range of 10 N m^{-1} with an error of ±2 N m^{-1}. Therefore, the measured friction anisotropy is not caused by an anisotropic stiffness of the tip which is assumed to be the softest spring in the system and therefore the determining one.

3.2.3 Analysis of [100] and [110] Direction

Another advantage of the rotatable sample holder is the ability to perfectly align the scan direction to the orientation of the crystal lattice. The orientation can be tuned very precisely by small movements of the rotator. The best results are achieved when there is very little drift and the piezo was moved on a small scale to reduce the influence of creep. The alignment of the main crystal axis parallel to the x and y direction of the scanner is done by optimizing the orientation of the measured friction diamonds along the fast scan direction. This is minimizing the influence of the drift by reducing the time scale of the measurement by a factor of typically 512, twice the number of lines in an image. Assuming a lateral thermal drift of 1.5 pm s^{-1} and a scan speed of 13 nm s^{-1} like in the images of Fig. 3.6 on a 6 x 6 nm^2 image, a drift of 2 x 256 s x 1.5 pm s^{-1} $\approx$ 0.77 nm is resulting along the slow scan direction (factor two comes from forward and backward movement). In other words, this is an error of almost 13 % or a misfit of the orientation of about 7° compared with less than 0.1° along the x direction. The precise orientation and small drift rates enable the measurement of very nice friction loops because it is possible to slide over many unit cells of the crystal without a substantial movement along the slow scan direction away from the desired position. With a misalignement of only 2.7° of the crystal orientation compared to the scan direction x, the tip is moving half a lattice constant along the y direction to the next row of ions of the lattice on a scan distance of only 6 nm. With the precise allignement of the sample, the scanned lines can be made to be parallel to the low Miller index crystal orientations.

The measurements in Fig. 3.8 were made after the careful alignment to the two crystal main axis. The force maps along [100] in 3.8(a) show the typical features, also referred as friction diamonds. Two friction loops are shown below the forward (left) and backward (right) force maps, they are chosen from the lines in the center of the friction diamonds (line 1) and between two centers (line 2) of the forward scan. Comparing the positions of the same lines on the *backward* (bwd) image, it is apparent that none of these two lines are at the same position in respect to the friction diamonds as they were on the *forward* (fwd) scan. The features of the bwd scan are slightly shifted toward the top. This has the consequence that friction

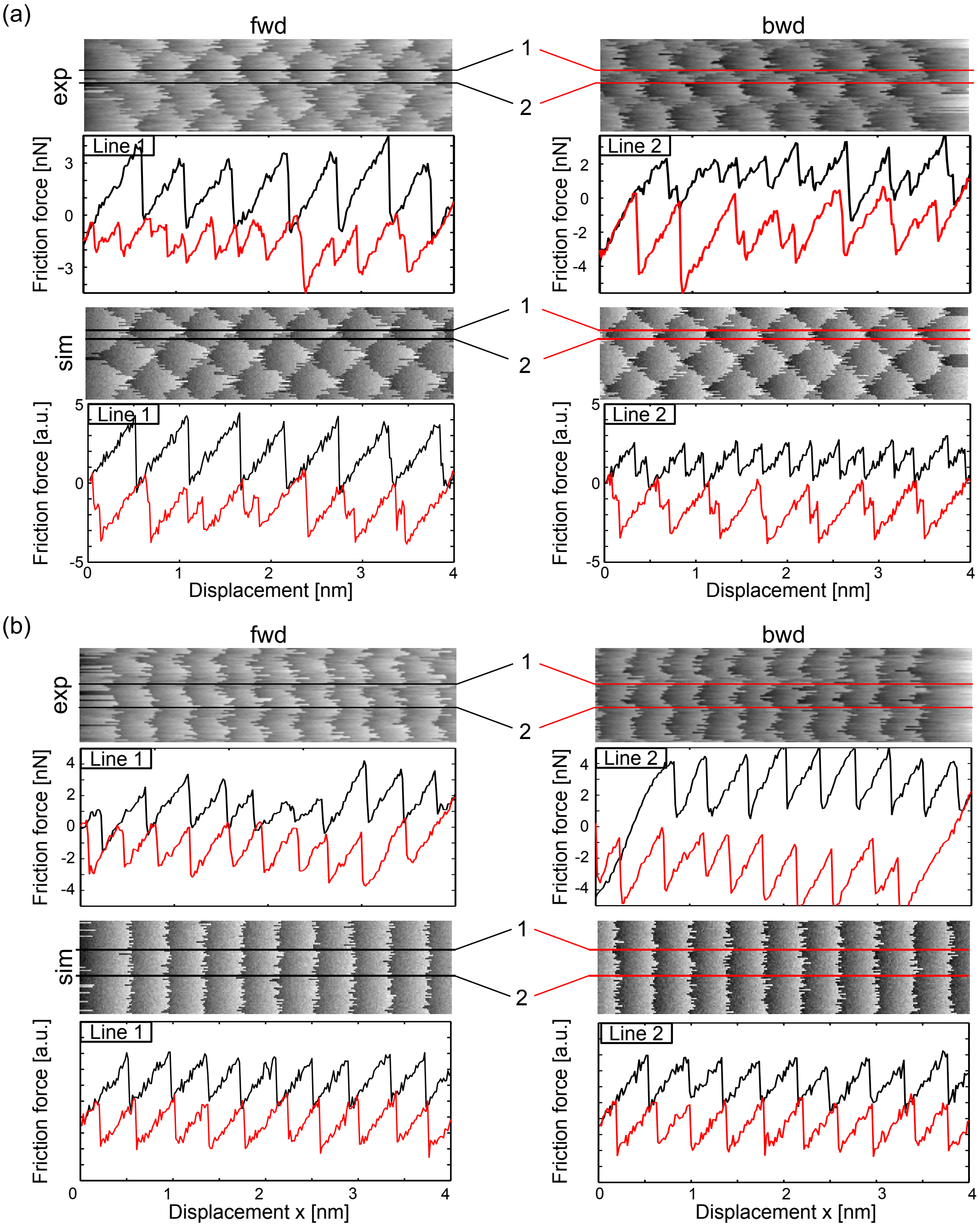

Figure 3.8. Friction force maps from experiment (exp) and simulation (sim) of forward and backward scans of the [100] direction in (a) and the [110] direction in (b) are presented. Two friction loops at characteristic positions for each orientation are shown. The load in both measurements is 0 nN and the scan speed was 8.7 nm s^{-1}.

loops are often looking quite different in fwd compared to bwd direction, a 180° asymmetry is often observed. In literature, often the idealistic loops are shown where the tip is crossing the center of the friction diamond in fwd and bwd scan and the tip is moving straight from one minimum to the next along the path of the support, resulting in symmetric friction loops. In the following discussion of the tip path it will be shown that this is a special case. The friction loop of line 1 shows this described stick slip mode in the black fwd line. The distance separating two slips, roughly corresponds to the lattice constant of NaCl. When the tip moves bwd, the periodicity is doubled, which is typical for the zig-zag movement when the support of the tip is moving between two minimas of the potential [64]. Line 2 is presenting the opposite behavior. The tip is expected to move in the zig-zag mode and therefore the sticking phase is shorter which is only seen in the fwd direction, the bwd scan is shifted such, that it is already in the region with the straight movement along x between the minimas. The comparison with the simulation shows exactly the same situation. The fwd and bwd maps are as well shifted along the slow scan direction resulting in the described differences of fwd and bwd scan. After the rotation of 45°, the tip is no longer moving over anions and cations alternatingly, it is scanned either over Na^+ or Cl^- along the dragged path (see Fig. 3.6). The force maps and friction loops along [110] are shown in Fig. 3.8(b). Since the tip is sticking to only one ionic site, it is clear, that the next closest sticking position will be found following the direction of the support movement. A straight stick slip movement instead of zig-zag movements can be expected at all positions and is observed in fact. This results in a very different contrast without the diamond structures. Because of the missing zig-zag movement, only vertical stripes remain. The friction loops confirm the expectations, the stick slip pattern has always the same periodicity indicating the straight tip movement. A weak contrast along y still exists, the loops 1 and 2 are on different sites that can be expected to be the Na^+ and Cl^- rows, respectively. The loop and therefore the friction of line 1 is much smaller than the one of line 2, indicating a different friction force depending on the ionic species below the tip. In the simulations, the contrast with the vertical lines is even more extreme. The positions of the ionic rows can not be guessed from the force maps and a difference in the friction loops is not visible. This will be discussed later to show, that even if not obvious here, a different friction on Na^+ or Cl^- rows is measured in the simulation as well.

The tip path along [100] at various positions can be seen in Fig. 3.9. The positions where the tip path was calculated, are drawn over the force map on the top of the figure. The line 1 is in both, the fwd and bwd scan, on top of the stability region where the stick slip pattern has the periodicity of the lattice constant. It is seen, that the tip is mostly moving straight from one position to the next, but already the next line (line 2) shows a zig-zag movement in most of the slips along the bwd direction. In line 3, the tip movement is in a zig-zag mode for both scan directions before the transition to a linear movement along the bwd scan happens in line 4. At last on line 5, a fifth mode shows a zig-zag movement where the tip jumps up along the fwd direction, down to the next stability regions in the bwd scan. The shift of fwd and bwd force maps is leading to this sequence of different combinations of tip movements which is also seen with the same manifestation in the numerical simulations (b). Only the linear tip movement is observed very rarely in the calculated force maps and therefore the linear movement along both, fwd and bwd direction, is missing. The combination of linear 'l' and zig-zag 'z' movements are sketched in (c). The observed sequence starting with the well known linear movement along both directions, would therefore be: 'll', 'lz', 'zz', 'zl' and '∞' (with '∞' as the zig-zag mode where the tip positions are different for fwd and bwd directions). Assuming a different shift along y of fwd and bwd scan, some modes could be observed more often, others could disappear. A slightly bigger shift would suppress the 'll' movement and produce more measured lines in the '∞'-mode. In literature the 'll' movement is often shown as the prototype of stick slip movement, but in fact, it is a quite special and rare case. These observations give clear evidence for the importance of an accurate and well suited potential for doing PT simulations since these effects are not observed when using the sinusoidal potential from eq. 3.5. The sinusoidal potential is failing to explain the discussed observations while the DFT calculated potential can reproduce the experimental findings consistently. The structure in the interface on the atomic scale has an influence on friction as it was lately also shown by means of nc-AFM by *A. J. Weymouth et al.* [65]. They described the angular dependence of lateral forces with nc-AFM when scanning over a Si dimer. In the presented situation here, the asymmetric behavior of fwd and bwd scans can not be explained by an asymmetry of the surface and is most probably only caused by the tip asymmetry.

Along the [110] direction, the slip number along fwd and bwd scans is the same. The friction loops are constantly showing the large slips with the long sticking phase in between. It is not surprising to see the tip path constantly along the scan direction without any zig-zag movement (see Fig. 3.10). The contrast along the slow scan direction is caused by different friction $F_{l,i}$ which is shown in the following and can not be explained with different tip paths.

Friction maps along the [100] and [110] directions are shown in Fig. 3.11(a) and (b). On the right hand side of the friction maps, the values of $F_{l,i}$ at the corresponding positions are plotted. The values of $F_{l,i}$ are distributed in a range of up to 1 nN, roughly according to a Gaussian distribution, though $F_{l,i}$ is changing as a function of the support y position leading to a wide distribution of the values. The variation of $F_{l,i}$ as a function of the displacement of the tip support along y can directly be related to the structures that are visible in the friction maps and therefore to the underlaying crystal lattice. The periodicity $\Delta y = 0.313$ nm of the oscillations of $F_{l,i}$ correspond roughly to half of the lattice constant of NaCl. In the plot of the friction force in Fig. 3.11(a) with the tip sliding along [100], it is seen that $F_{l,i}$ reaches the minimal value at the positions of the center of the friction diamond when the tip is sliding in the above introduced 'll' mode. In the 'zz' mode, located between the center of the diamonds, friction is found to be largest. The same behavior is observed in the PT simulations seen in 3.11(e). The data from the center (marked in yellow) was taken to calculate 3.11(c), which presents the mean values of $F_{l,i}$ at different positions averaged over 6 rows of friction diamonds. The result in 3.11(c) is shown as a map and below the mean value of each row is plotted. The friction reduces about 15% from 1.5 nN when sliding in 'zz' mode to 1.3 nN in the 'll' mode. The variation of $F_{l,i}$ in connection with the y position of the support is also clearly visible in 3.11(b), where the tip is sliding along the [110] axis, meaning the tip is dragged over only one kind of ions in a scan line. In this image, the atomic features

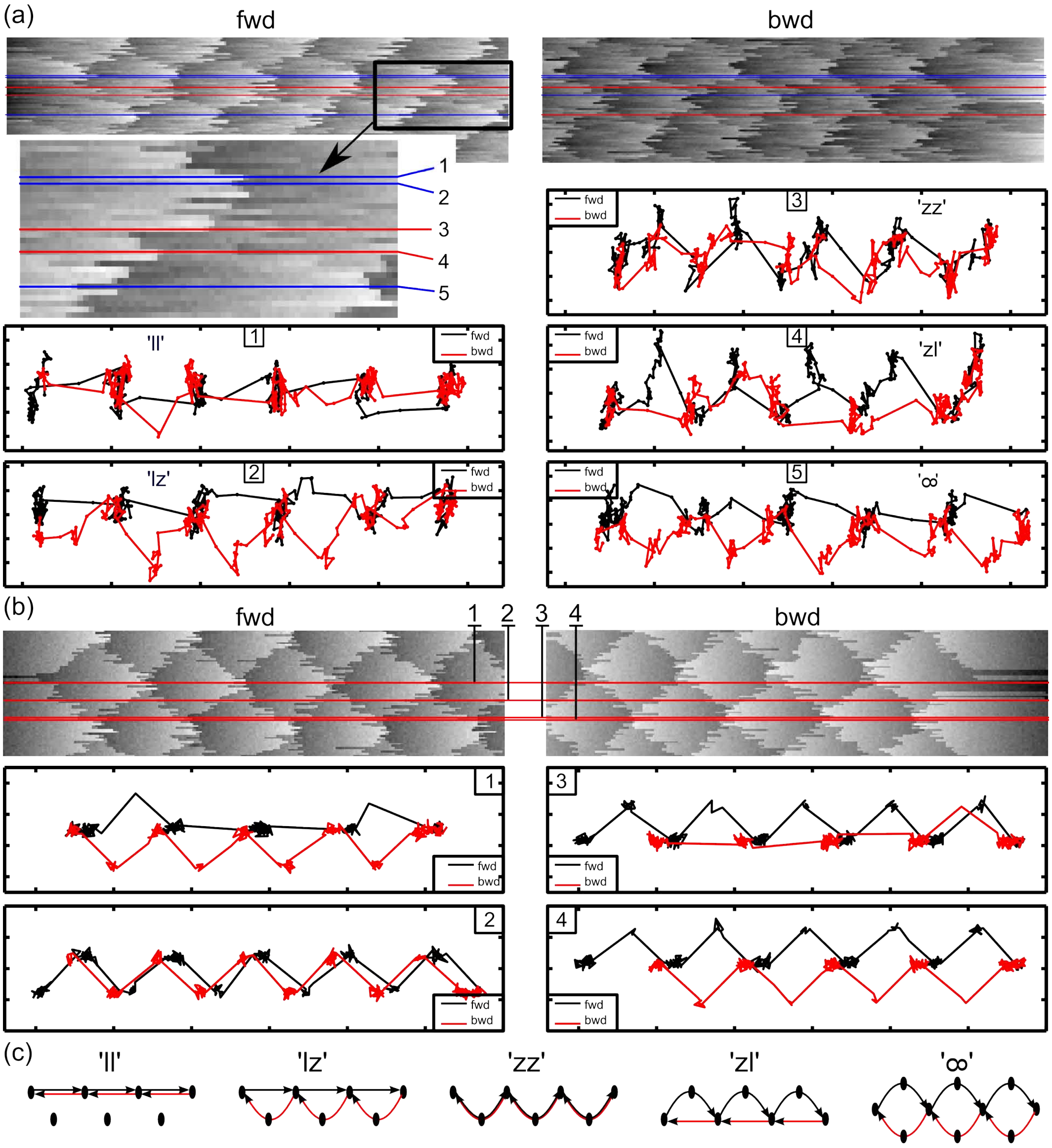

Figure 3.9. The tip path for 5 different positions of the measurement with 0 nN load is seen in (a), the corresponding simulated paths are shown in (b). (c) is sketching the 5 prototypes of observed tip paths.

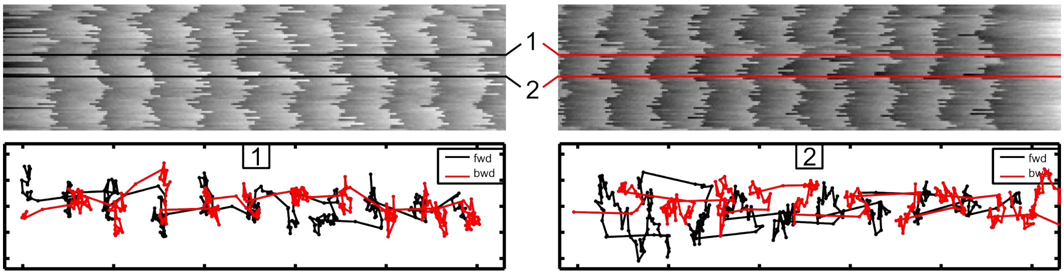

Figure 3.10. Tip path along the [110] orientation at positions separated by the distance between the Na and Cl rows of almost 2 Å.

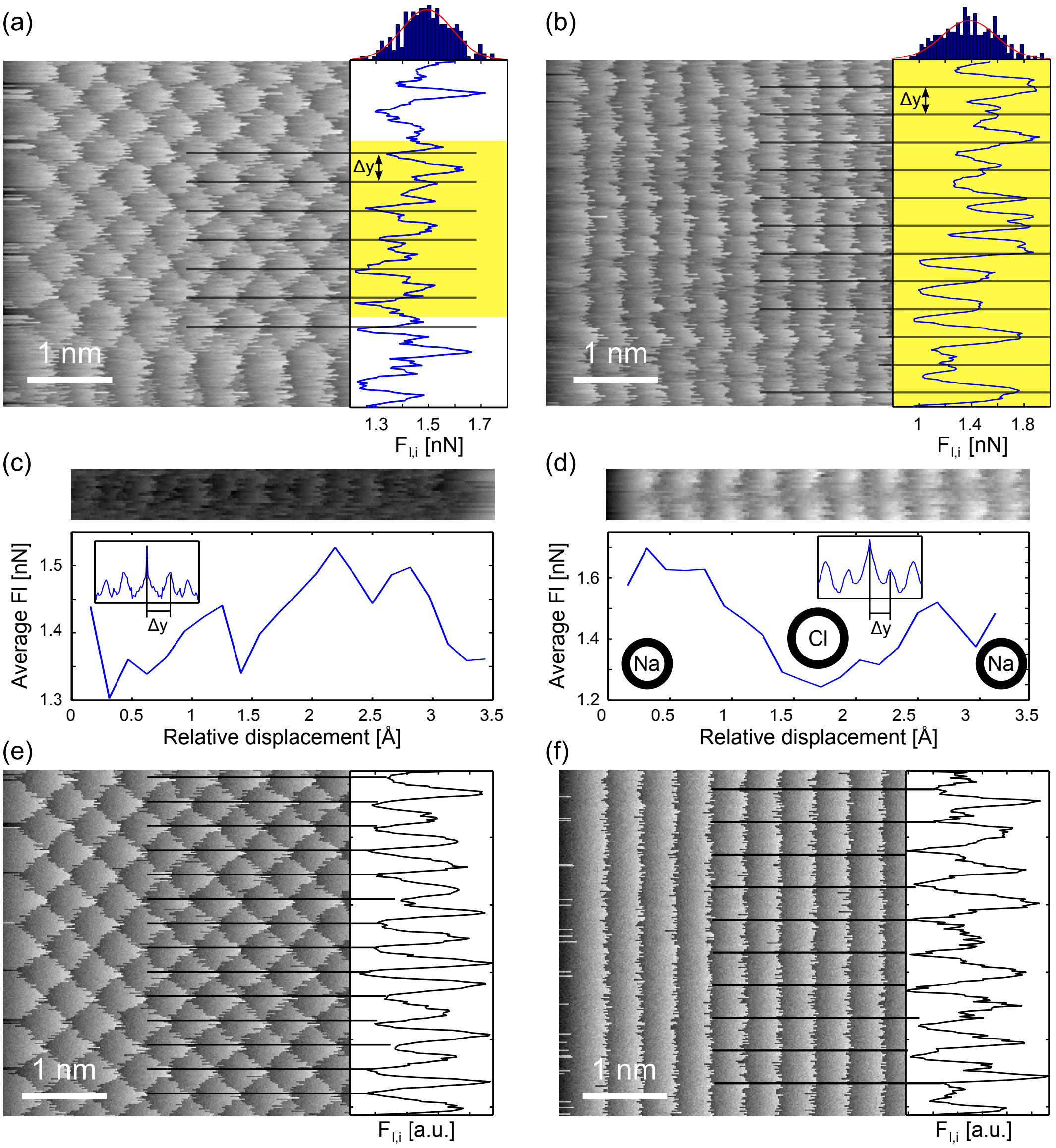

Figure 3.11. Friction maps along (a) [100] and (b) [110] orientation on 4 x 4 nm^2. Right to the maps, the corresponding $F_{l,i}$ is plotted after smoothing the data, a histogram of the raw values is shown on top. In (c) and (d), unit cell averaged values from the yellow marked regions of (a) and (b) were calculated. The periodicity Δy of the lattice was determined with the autocorrelation in the inset. The corresponding friction maps from the simulation in (e) along [100] and (f) along [110].

can not only be seen in the stick slip curves along the scan direction, there is also a contrast along the slow scan direction, manifested clearly in the variation of $F_{l,i}$. The periodicity $\Delta \mathrm{y} = 0.344$ nm of the oscillations of $F_{l,i}$ along [110] roughly correspond to $\frac{1}{\sqrt{2}}$ times the lattice constant of NaCl which is the distance between ions of the same kind along [110] and [$\bar{1}$10], respectively. In the simulation 3.11(f) the contrast along y is not clearly seen in the map but the $F_{l,i}$ values show the same behavior as described for the experimental data. With the averaged values of $F_{l,i}$ in 3.11(d), the different friction on Na^+ compared to Cl^- sites is seen. Here, the assumption was made, that friction on Cl^- sites is smaller because this was the result of the numerical simulations where the silicon tip was probed on the surface. In the experiment it is quite probable that the tip apex was covered with NaCl, meaning friction could also be smaller on Na^+ and larger on Cl^- positions. Either way, the friction was 1.7 nN on one ionic species and 1.24 nN on the other, a reduction of 27%. In the image of the averaged values, the contrast on the supposed Na^+ sites is quite strong and weak on the Cl^- rows.

In our understanding, the process behind the contrast formation along the slow scan direction of the two investigated orientations is very different. Along [100], the tip is dragged alternatingly over Na^+ and Cl^- sites, independent of the y position of the support. The tip path is depending on the y position though, producing the contrast of the friction diamonds. The resulting friction force is directly related to the tip path. Sliding along the [110] axis, different lateral forces are measured when the tip is dragged over Na^+ or Cl^- sites, which produces the very clear oscillations in Fig. 3.11(b). A difference in friction force of 0.454 nN was measured on different ionic sites or in other words, a friction reduction of 27% is found between cationic and anionic rows. An influence of the tip path in this orientation can be excluded because the tip is as good as always jumping straight parallel to the scan direction to the next position. The absence of the zig-zag movement is the origin of the different contrast along the slow scan direction.

3.3 Friction Anisotropy Investigation on BNL

3.3.1 The Benzylammonium Crystal

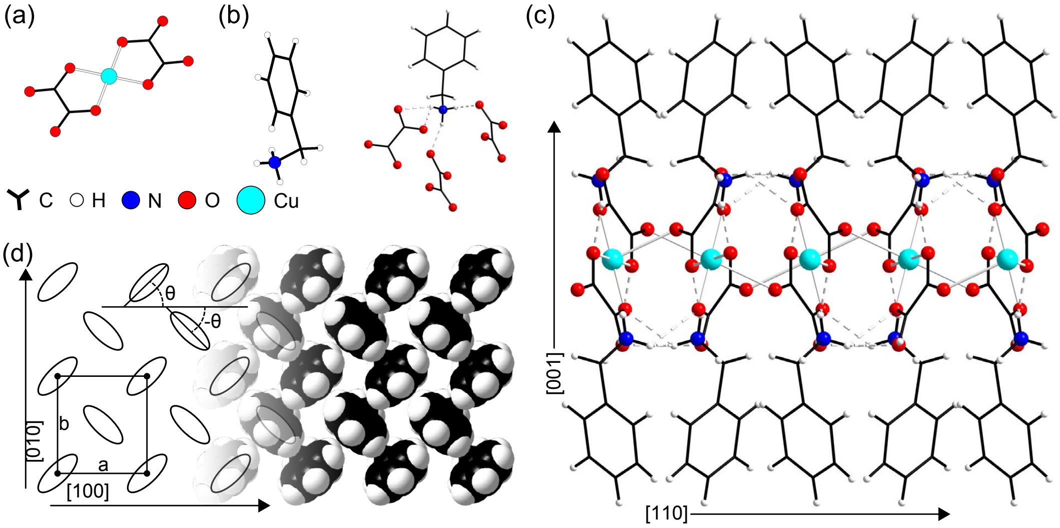

Figure 3.12. The $[Cu(C_2O_4)_2]^{2-}$ complex (a) builds up an extended two-dimensional structure surrounded by the organic benzylammonium cations (b). Structural motif of the compound (c) which is built up by multiple stacks of the illustrated layers. The top view of the (001) crystal surface (d) showing the orientation of the BA molecules. BA molecules are rotated by $\theta \approx 48°$and $-\theta$ with respect to the [100] direction. The lattice constants are $a = 7.1$ Å and $b = 8.0$ Å.

The *benzylammonium crystal* (BNL) investigated in this section, can be categorized as a transition-metal oxalate complex, which are well known to exhibit extended layer-type crystal structures [66]. In this case, the salt bis(benzylammonium)bis-(oxalato)cuprate(II) described by the formula $(C_6H_5CH_2NH_3)_2[Cu(C_2O_4)_2]$ crystallizes in a hybrid lamellar structure [67]. The planar $[Cu(C_2O_4)_2]^{2-}$ metal complex anions (Fig. 3.12(a)) aggregate into robust two-dimensionally extended anionic coordination networks which are separated by organic cations [68], *benzylammonium* (BA) cations in the investigated BNL crystal (Fig. 3.12b). These pendant organic cations decorate the tops and bottoms of the anionic sheets formed by the copper oxalato complexes by means of hydrogen-ionic bonding of their NH_3^+ heads to the oxygen atoms of the oxalate ligands (Fig. 3.12c). Thereby, the benzyl groups of the cations extend into the space between the inorganic layers giving rise to non-covalent v*an der Waals* (vdW) interlayer interactions, and serving to organize the neighboring inorganic layers into a complete lamellar crystal structure. This compound crystallizes in the form of solvate-free light-blue elongated and rectangular plates in the orthorhombic space group *Pbca*, whereby the layer structure as well as the single crystal morphology is extended along the [100] and [010] crystallographic directions. Consequently, by extrapolating the crystal structure from the bulk of the crystal to its extended flat (001) surface, the latter appears to be decorated in a stereoregular manner with the benzyl groups in an upright orientation, slightly

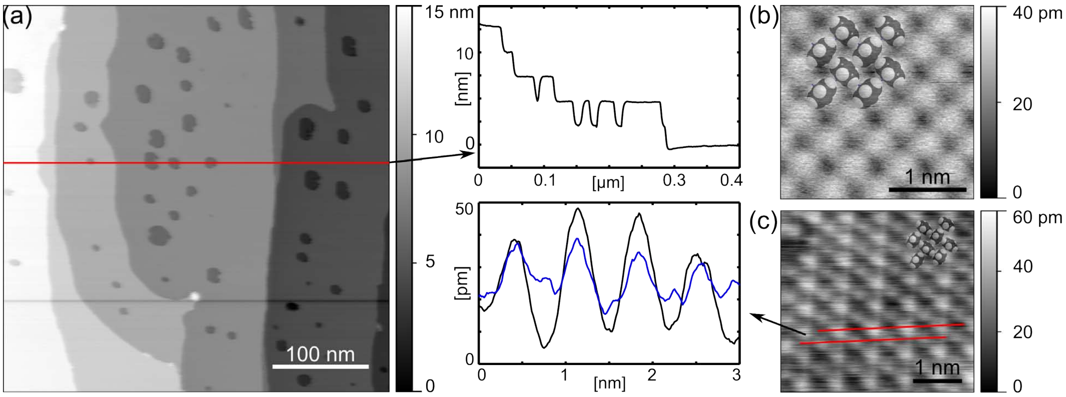

Figure 3.13. The steps and wide terraces of a BNL crystal are seen in (a). (b) and (c) show two different contrasts measured by means of nc-AFM.

tilted to the surface normal (Fig. 3.12c). The result is a crystallographically defined anisotropic molecular surface cover (Fig. 3.12(d)) [33].

For the investigation of friction anisotropy, such well ordered, anisotropic molecular surfaces offer a promising platform. The layered nature of the compound enables the cleaving of the crystal, similar as it is done with graphite. The vdW forces between the layers of the crystal are weaker than the hydrogen-ionic bonds of the BA molecules to the metal complex sheet, enabling the peeling off of complete layers, giving rise to the BA covered surface. On the surface, the BA molecules are organized in rows with two different orientations as seen in Fig. 3.12(d), which will be investigated by means of FFM. Other crystals based on these layered organic and metal complex structure described in literature [68] could provide an even more anisotropic surface coverage of the molecules. Similar compounds with different molecules and different molecular configurations on the surface were tested. The stability under UHV conditions is a crucial aspect which made it impossible to work with other compounds so far and finally lead to the investigation of BNL. The discarded crystals were decomposing in vacuum and the surface quality was not reached to resolve molecular stick slip.

For the investigation with the UHV AFM, a BNL crystal was glued on the rotatable sample holder and cleaved before the transfer into the vacuum chamber. The sample was not annealed in UHV. In additional to the risk of damaging of the rotatable sample holder, the crystal is decomposing at temperatures around 100°C. On a nicely cleaved surface, wide and atomically flat terraces are seen as shown in Fig. 3.13(a) exhibiting an excellent surface quality. Even on the molecular scale, the surface quality is very good as seen with nc-AFM in Fig. 3.13(b). The small corrugation of less than 50 pm requires a very sharp tip and small tip sample separation.

With nc-AFM techniques, 3D force maps can be generated by collecting data either by scanning in a topographic mode or by doing force spectroscopies on a grid [69]. The number of points on a 3D force map is given by the product of the number of points along each of the tree Cartesian coordinates. Even with small resolutions in each direction, the number of data points is large and the scan time scales with this number. For measurements at room temperature, thermal drift is a big problem that must be compensated. An elegant way to do this is by tracking a reference

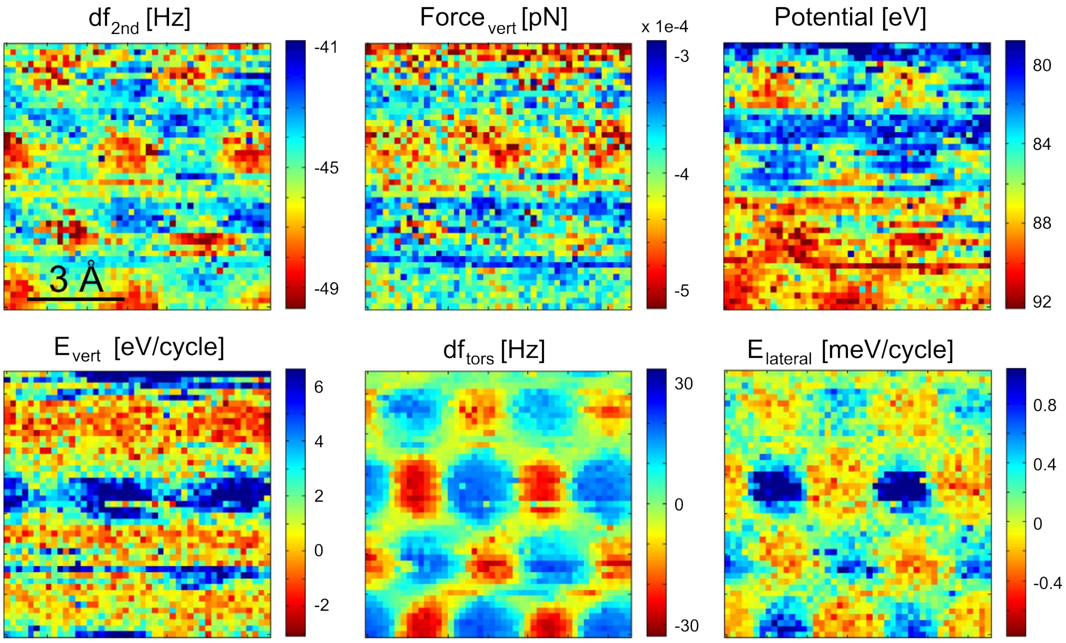

Figure 3.14. Section of a force field made on the BNL surface with the old RT AFM with the help of the atom tracking function. Two PLL's were used for tracking the second flexural and the first torsional resonance.

point with the atom tracking procedure and doing force spectroscopies alternatingly. The atom tracking function is basically determining the position of an atom (or molecule in the case of BNL) by circling around it at a certain set point. This requires a good resolution on the atomic scale. In the case of BNL with the quite small atomic corrugation, it was very difficult to achieve and tip changes during the measurement were the biggest problem. Often the atom tracking fails when the tip state is changing, severe contrast changes occurred in most of the measurements. Different channels from one plane out of such a forcefield are shown in Fig. 3.14. An experimental extraction of a potential for the use of PT simulations explaining the frictional behavior of BNL could be done with the gained forcefield, but as the previous discussion about NaCl showed, the application of such a potential for the simulation of the tip in contact is questionable because of a too large tip sample separation. The strong contrast changes related with the state of the tip apex is another factor that has to be kept in mind. Forces and energies can be extracted from the frequency shifts using the Sader-Jarvis formula [70] for the fundamental oscillation. Here the 2^{nd} flexural mode was used on the first PLL and the torsional resonance on the second. The forces and energies are derived according to the formulas described in literature [48, 71]. A weak contrast disappearing in the noise is seen in the channels from the normal oscillation. Tip changes probably happened in the middle and lower parts of the map, though it is only seen in the calculated force and potential. A good contrast is seen in the channels from the torsional oscillation. A contrast between neighboring rows could be seen, but it is questionable whether it is due to tip changes or a real effect. The interpretation of the lateral frequency shift is not trivial [71] and will not be discussed further here.

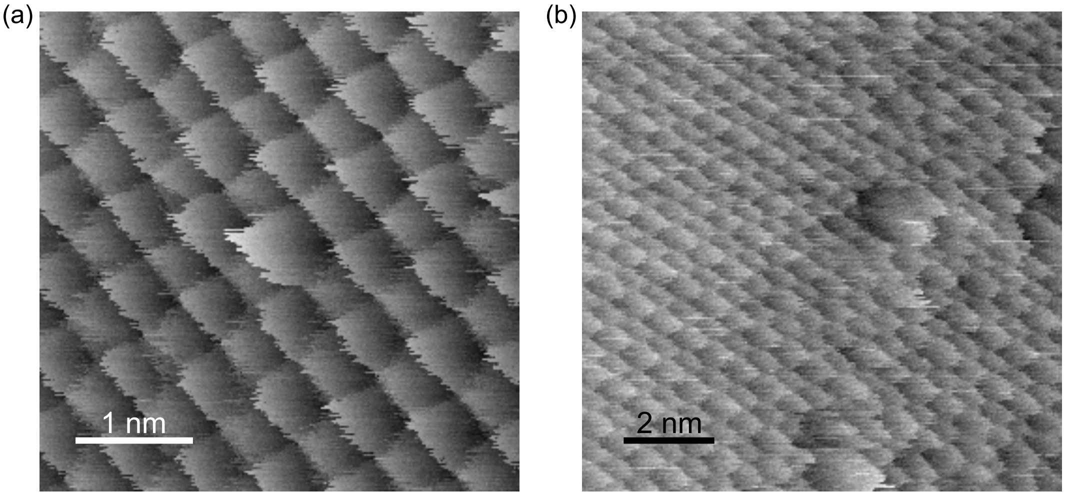

Figure 3.15. The friction maps (a) and (b) show defects which are evidence for a very small contact area.

The nc-AFM measurements in Fig. 3.13(b) and (c) demonstrate that a contrast between differently orientated molecular rows is depending on the tip apex configuration. The measurements are ranging from a clear, distinct contrast to a perfectly regular pattern, where the two molecular configurations can not be detected. This makes the use of a measured potential for a base to do PT simulations even more questionable as long as the tip condition can not be controlled. Various recent studies reported the use of a well defined tip that was functionalized with a molecule, mostly CO, which improves the resolution to a range where sub-molecular features are visible [72, 73]. A force field made with such an extreme sharp and stable tip would minimize the influence of an asymmetric tip and it would be interesting to see the resulting contrast. On the other hand, tip asymmetries are also influencing the frictional behavior as it was shown in section 3.2, which are missing for such a tip.

3.3.2 Friction Contrast on BNL

The friction measurements were done with doped silicon PointProbe® Plus Contact Mode levers from NANOSENSORS™. The levers were heated in vacuum to remove absorbed water on the surface. With some luck, the tip apex is such, that a contrast between neighboring molecular rows is visible, corresponding to differently orientated molecules. In all of the presented FFM measurements, the tip apex can be considered to be very sharp with a contact radius in the range of 1 nm. Measured defects indicate the size of the contact area which ranged from single molecular size up to few molecules with the used cantilevers as seen in Fig. 3.15. The tip state is essential for the measurement of a good molecular contrast and only measurements with this kind of tips are considered here. With small contact areas, the pressure is increasing strongly with an increase of normal force, 1 nN results in 1 GPa for a 1 nm^2 contact. To preserve the tip state, a narrow range of loads of -5 nN to 5 nN was used.

In Fig. 3.16 such friction force maps are shown for scans along different orientations.

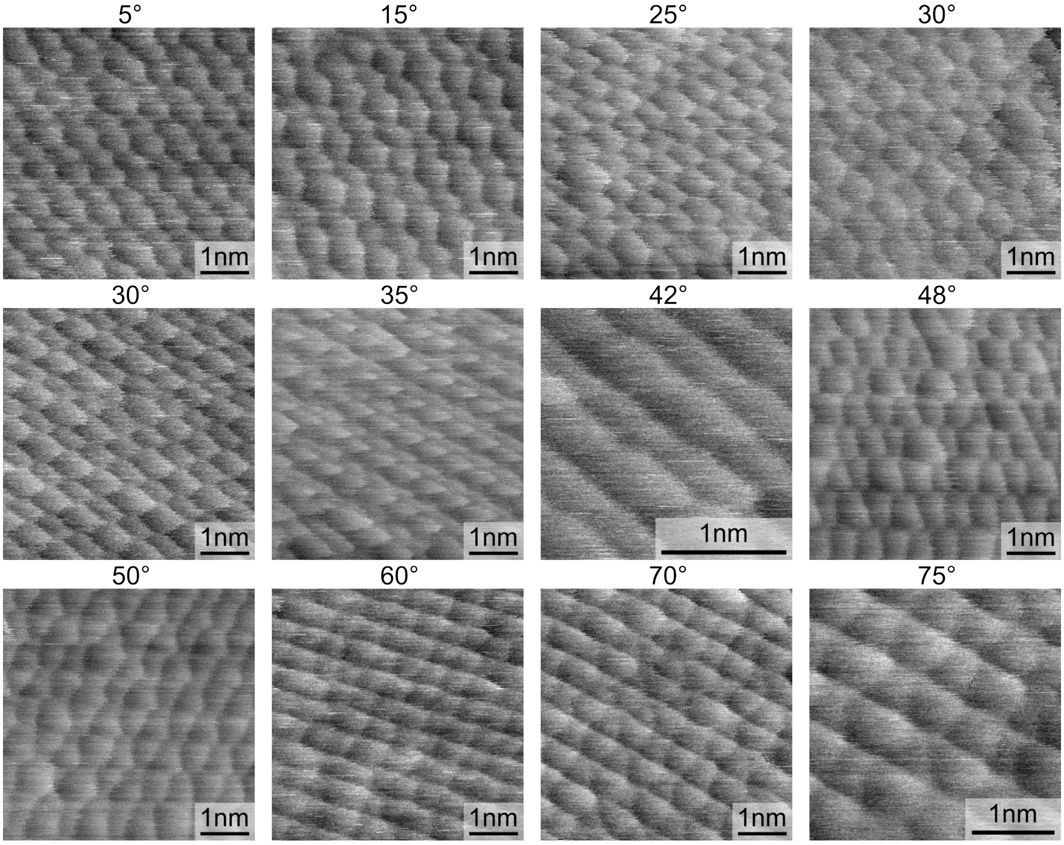

Figure 3.16. Friction force maps along different orientations made with the same cantilever starting at 5°, increasing the angle constantly to 75°.

The crystal orientation can be determined according to the geometry of the crystal, but the [100] and [010] directions can not be distinguished so easy. The lattice constant along [100] and [010] differ by roughly 1 Å and can be measured with the AFM. The [100] orientation will later be referred as 0°, [010] correspond to 90° and [110] to roughly 48°.

The presented force maps in Fig. 3.16 show the range of contrasts that were measured with the clearly visible difference between the two different orientated molecular rows of the BNL surface. In the friction maps on the first line along 5° to 30°, a characteristic shape of friction diamonds can be observed. The diamonds show a different shape than it was described in the previous section about NaCl. The friction diamonds of BNL in these first 4 friction maps have a hexagonal shape resulting in a honeycomb pattern. In the second line, another measurement along 30° is shown which does not show this honeycomb structure anymore. This different contrast is most probably due to a tip change and can also be observed in the measurements along 35° and 42° before it changed again. The following measurements of 48° to 75° can be classified as a 3^{rd} contrast with trapezoid-like structures. A lot of questions arise from these observations concerning the origin of this contrast and the consequences for the frictional behavior. The former can here only be speculated about while the measurements will exhibit some of the consequences for the friction. Assuming the situation of a two body problem, namely the silicon tip and the BNL

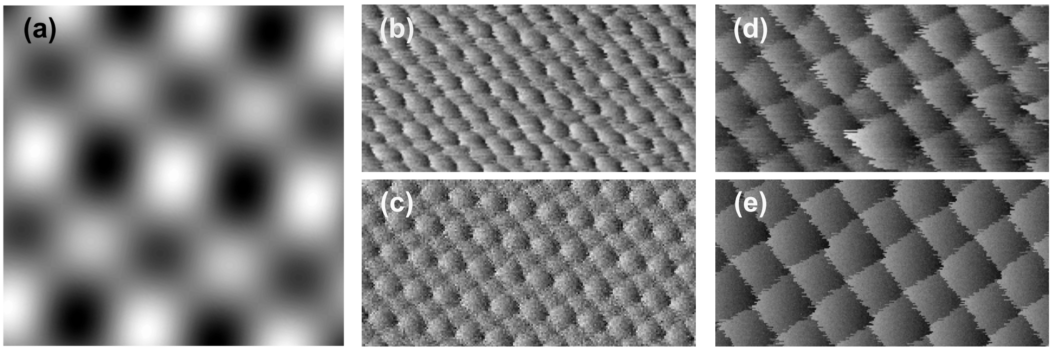

Figure 3.17. The modified potential V$_{BNL}$ (a) rotated by 10° to match the scan direction of the measurement in (b) with 0 nN and (d) 1.1 nN Load. The simulation (c) was done with $\eta = 1$, c = 0.35 and (e) with $\eta = 3$, c = 0.1.

surface in sliding contact (i.e. no contaminations in the interface), the contrast is an indication of either the influence of the tip symmetry (or rather asymmetry) or the response of the different relative angle of the molecule in respect to the scan direction. The interaction of BA with the tip has an anisotropic component leading to the contrast which can be observed even by means of nc-AFM techniques. The influence of a tip change to the measured contrast is then obvious. On the other hand, the BA molecules are strongly confined on the ammonium side close to the metal complex but the benzyl heads forming the surface could move slightly when forces are applied. Molecular dynamics simulations of a BA terminated diamond surface showed a clear movement of the molecules when forces are applied by an approaching tip [74]. The resulting simulated force spectroscopies are qualitatively explaining an indentation that is seen in nc-AFM force spectroscopies. The model system in these simulations was simplified by the use of the well known carbon backbone structure which only allows to draw qualitative conclusions, particularly the simulations are showing clearly that the molecular arrangement can not be considered as a rigid system and the sliding tip can locally influence the molecular orientation.

For a comparison of the FFM measurements with numerical calculations, an interaction potential of the tip with the surface is not available. Nevertheless, simulations were made along the 10° orientation using a potential on the base of the sinusoidal potential V$_{NaCl}$ but modified in order to get two different neighboring rows which differ in amplitude, width, and with adopted lattice constants along [100] and [110]. The potential

$$V_{BNL}(x, y) = -\frac{E_0}{2}\cos(\frac{2\pi}{a}x)\left(\cos(\frac{2\pi}{b}y) + c\right) \tag{3.6}$$

matches these expectations with the lattice constants a and b and the parameter c giving rise to two different energy barriers $E_0^+ = E_0(1 + c)$ and $E_0^- = E_0(1 - c)$. The resulting potential was rotated by 10° to match the measurements (seen Fig. 3.17(a)). Two examples of measurements and corresponding simulations (b), (c), (d), and (e) are shown. The measurement in Fig. 3.17(b) exhibit a contrast of a row with almost smooth sliding and the neighboring ones with considerably larger friction which initiated the selection of the potential with different energy barriers E_0^+ and E_0^-. The friction diamonds have different sizes which was the reason to introduce the

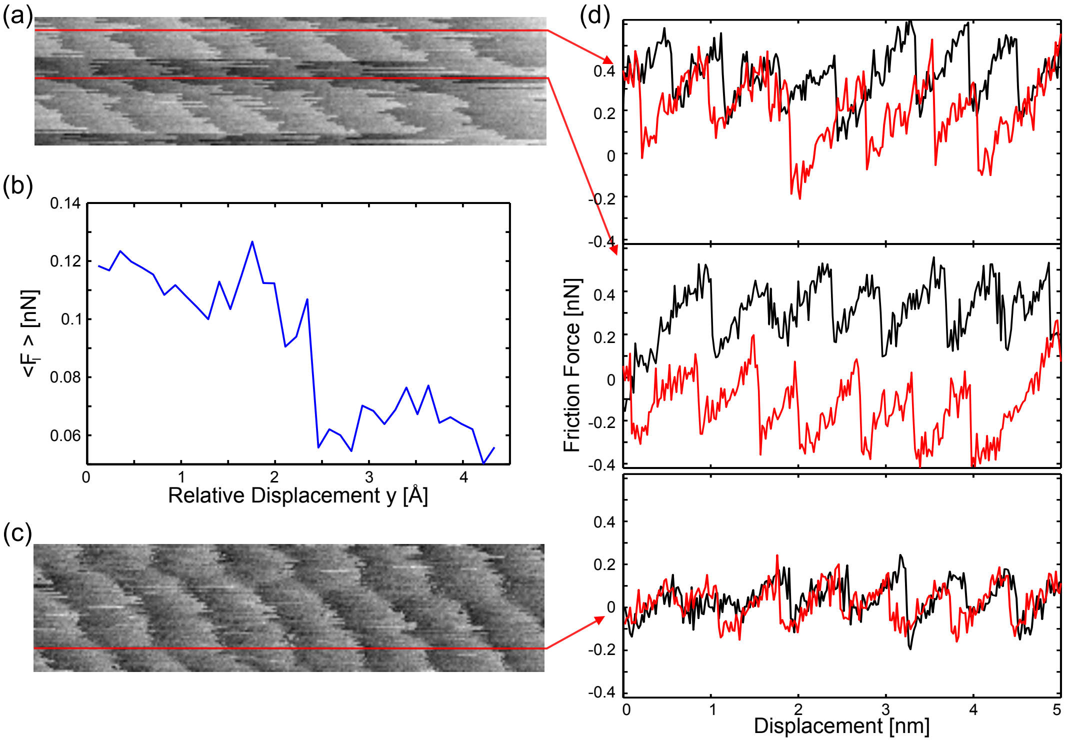

Figure 3.18. Friction force map from the measurement along [100] in (a) and 5° off in (c) are shown. In (b) the unit cell averaged <F$_l$ > is shown which was calculated from the average of F$_{l,i}$ values which are from lines that are separated by a multiple of the unit cell. The line sections in (d) are taken from the marked lines representing characteristic friction loops.

different width in the potential. Further details can be read in the published article [33]. The potential showed a very good agreement with the measurements, indicating that the corrugation potential is in fact influenced by the molecular orientation. For the simulation along different directions, a much more sophisticated potential is needed to meet the physical properties of the surface probed by the AFM tip, probably only an ab initio calculated potential can produce satisfying results.

3.3.3 Friction Anisotropy on BNL

In the above presented friction maps, the measurement along [100] is missing. The selection in Fig. 3.16 intended to show the nicely resolved contrast of differently orientated molecules which can only be achieved in a regime of low friction. Approaching the [100] direction, the friction increases drastically with a big effect on the contrast in the force maps. The resulting contrast can be seen in Fig. 3.18(a). The part of the bwd friction map shows a clear contrast between neighboring rows, but the diamond or honeycomb like structure is strongly disturbed. The two upper friction loops in Fig. 3.18(d) show a clear stick slip pattern, but the fwd and bwd lines are separated much more in the darker regions of the friction map. This effects the values of F_l as clearly seen in the plot in 3.18(b) which presents the averaged values of lines from the same position within the unit cell. On about 55% of the

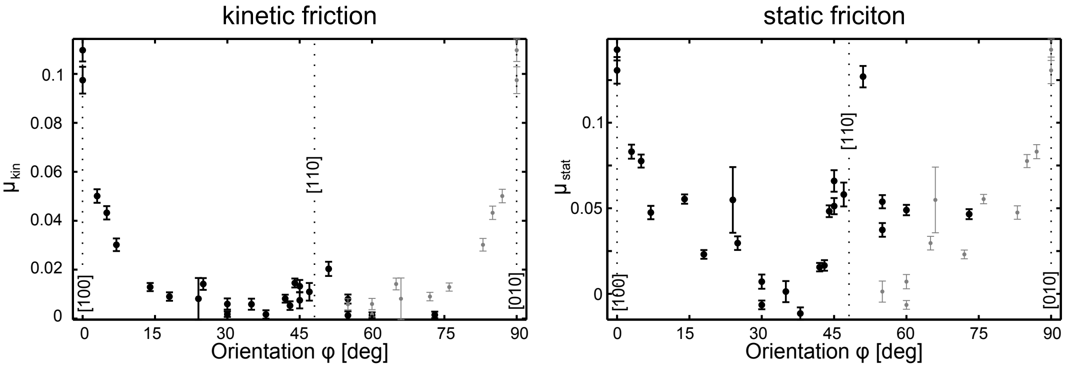

Figure 3.19. Orientation dependence of the kinetic (a) and static (b) friction coefficients. The gray points are projected measurements from the orientation 90° − φ.

surface the friction is with 0.12 nN twice as large as on the other 45%, a gradual transition between these two states is not seen but rather a sudden jump between the two regimes. The fact that this is only seen clearly along the bwd direction gives a clear evidence for a tip assymetry and for the sensitivity of the friction to the actual tip state. The measured contrast between different orientated molecules along [100] arises from a certain tip condition that offers a bigger cross section to the molecules with one orientation. The molecules of the next row include the same angle to the scan path but rotated in the other direction. Changing the scan direction from bwd to fwd can involve another part of the tip apex interacting with the surface and therefore result in another contrast. When the sample is only rotated by 5° away from the alignment of the lever with the crystal axis, the friction response is already extremely different as seen in fig 3.18(c) and the corresponding friction loop in (d). This is not due to a tip change, the measurement along 0° was repeated afterwards and showed again the large friction values with wide friction loops. The measurements were done with the same normal load and still, a misfit of the alignment of only 5° reduced the friction to less than 50% resulting in an almost smooth sliding.

The friction measurements with this tip were started at 0°, then 3°, 5° and again 0° was measured to see if the high friction state is really a result of the scan direction, and not due to a tip change. Except for the step from 5° back to 0°, the rotations were all made in clockwise direction in steps ranging from 1° to maximum 7°, ending at 73°. There, a severe tip change happened and it was not possible to do a full cycle to 180°. Unlike the NaCl crystal, the 90° rotation symmetry of the BNL surface is broken by the different lattice constant along [100] and [110]. In addition, the crystal structure is such, that the molecules are slightly tilted compared to the surface normal as seen in Fig. 3.12. The tilt is only a few degrees and will be ignored in the following discussion, it could have an effect to the interaction with the tip, though. The different lattice constants along the main crystal orientations is influencing the elastic energy that is stored in the lever just before the tip is jumping. This is described with the parameter $\eta = \frac{2\pi^2 E_0}{ka^2}$ from the PT model introduced in eq. 1.4. The different lattice constants a along [100] and [110] result in two different values of η with the ratio of

$$\frac{\eta_{[100]}}{\eta_{[010]}} = \frac{8\text{Å}^2}{7.1\text{Å}^2} \approx 1.27. \tag{3.7}$$

Accordingly, the response to a decrease of normal load will effect the friction differently along the [100] and the [010] direction, and the regime of a continuous sliding and ultra low friction should be reached earlier along [010] where η is smaller at a given load [14]. Therefore, friction on BNL can be expected to be smaller along the [010] direction.

The measured friction coefficients of the rotation experiment were calculated by the same methods as described in 3.1. In Fig. 3.19 the kinetic and static friction coefficients are plotted in black. The gray data points can only be considered under the assumption that the 90° asymmetry of the surface has no mayor effect on the frictional properties and should only show what could be expected for the orientations between 65° and 90°. The high friction values when sliding along the [100] crystal axis are very distinct regarding the kinetic friction. It reduces within the first 10° down to a level that is difficult to measure by means of AFM with such a small range of loads that were applied in the experiments. The loads ranged from -5 nN to 5 nN with the relaxed lever position as the 0 nN reference. The static friction shows a less pronounced decrease of friction away from the main crystal direction. An increase when the sliding direction is close to the [110] orientation at 48° can also be observed. The friction behavior is reminding of measurements on graphite where often a small graphite flake is attached at the tip apex and therefore in a period of 60° a commensurate state is reached. Friction in the commensurate state is then large and going below the detection limit of the instrument in the incommensurate state [20]. Even with the very sharp tip it can not be excluded, that this situation is also present in our system. The tip could be covered with BA molecules or even a very small flake of the BNL crystal, resulting in a commensurate interface along [100].

The best that most of us can hope to achieve in physics is simply to misunderstand at a deeper level.

Wolfgang Pauli

Chapter 4

Friction on Pristine and Hydrogenated Graphene

Graphite is known to be one of the best solid-state lubricants in air [75]. This makes its monolayer variation, graphene, an attractive prospect as a lubricative coating, e.g. for *nano electromechanical systems* (NEMS). For instance, it was recently shown that the friction coefficient of SiO_2 reduces from 0.68 to 0.12-0.22 after coating it with a monolayer graphene [76]. Currently, large size monolayer graphene can be grown either by epitaxial growth on SiC or by chemical vapor deposition (CVD) on a metal substrate, while graphene prepared with the second method can be subsequently transferred onto a desired scaffold of use [77, 78]. Graphene has a negative thermal expansion coefficient and, therefore, when prepared with these thermal methods, suffers greatly from the formation of grafolds (also called wrinkles or ripples) during cool-down. Another problem concerning the quality of graphene is its extreme lipophilicity. When exposed to air, it is virtually not possible to obtain graphene without hydrocarbon contamination [79–82]. High temperature annealing (>300°C) in ultra-high vacuum (UHV) or in dry ambient air is a frequently used technique to remove contamination from graphene [83–85]. Various techniques such as atomic force microscopy (AFM) in intermittent contact mode [83], transport measurements [84], and position of the Raman spectroscopy peaks [83–86] were used to check the effectiveness of the cleaning process. However, this process may lead to degradation of electronic properties of graphene due to closer contact with SiO_2 [85]. Furthermore, annealing at moderate temperatures (100-200°C) already changes the doping behavior without removing the hydrocarbons [85,87,88], making the actual role of hydrocarbons quite disputable. Another recent study suggests that such contamination has no substantial effect on the properties of CVD graphene by presenting an insignificant degradation in the electron mobility after thermal

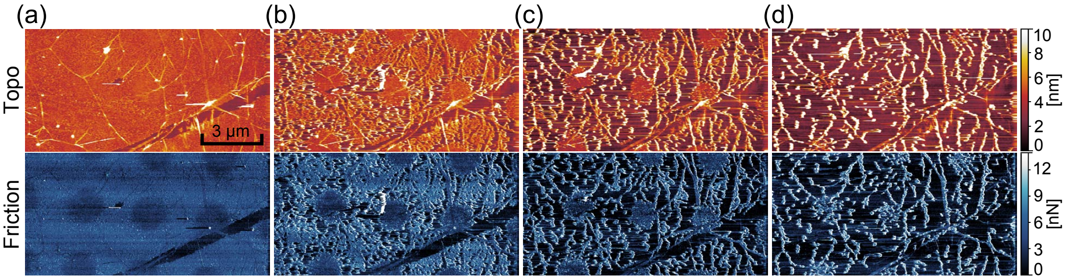

Figure 4.1. Topography (upper panel) and friction (lower panel) images of 12 × 6 μm^2, obtained during the (a) 2^{nd}, (b) 15^{th}, (c) 22^{th} and (d) 37^{th} scan. All measurements were made with 3.2 nN normal load and a scan velocity of 50 μm s^{-1}. The scan was started from the bottom with the fast scan direction along the 12 μm long edge.

treatment [89]. As an alternative to thermal annealing, two recent studies show that further cleaning (after thermal treatment) is possible in the course of scanning the AFM tip in the contact mode over the surface [90, 91].

Another novel and quasi-two-dimensional material is graphane, which is graphene fully hydrogenated from both sides with a 1:1 carbon to hydrogen ratio [92]. Currently there is no experimental data available regarding the frictional properties of hydrogenated graphene. In this section, the previous research on the mechanical cleaning and frictional behavior of single layer graphene supported on Si/SiO_2 is extended to those related to hydrogenated graphene.

Monolayer graphene was grown on a copper foil in a split quartz tube furnace using a CVD method involving methane and hydrogen gases [93]. Transfer of the graphene layer onto the Si/SiO_2 substrate was achieved by the standard procedure involving PMMA coating, dissolving the copper foil in an iron nitrate solution, 'fishing' the polymer with the substrate, and the removal of PMMA in acetone [78, 93]. Hydrogenation was achieved with low temperature plasma treatment, which has an electron temperature of 3.5 ± 0.5 eV and an ion flux of $1.5 \pm 0.5 \times 10^{15}$ $cm^{-2}s^{-1}$. The sample was kept electrically floating during 5 minutes of exposure, and accordingly the ion impact energy is estimated to be ~12.6 eV. With this technique, proton deposition energies can be obtained which are high enough to overcome the energy barrier (3.7 eV) to penetrate the center of the hexagonal carbon [94], without physically sputtering the carbon atoms (36 eV) [95], enabling double side hydrogenation of monolayer graphene. More detailed information about the plasma treatment can be found elsewhere [96]. During plasma exposure, the sample was covered with a silicon stencil mask with a periodic hole pattern. The mask itself was not in direct contact with the investigated surface. The obtained sample has a passive zone, the pristine graphene which was completely covered during plasma treatment, and an active zone consisting of round hydrogenated graphene spots surrounded by pristine graphene. Finally, the sample was heated to 130°C in UHV to remove the interfacial contaminants (e.g. water) between the graphene layer and SiO_2 [88], and to release possible charges in SiO_2.

Due to its outstanding attributes, graphene has been investigated various times in the last couple of years by means of friction force microscopy (FFM) [97–99]. The FFM experiments were performed with a Nanosurf FlexAFM with a 100 × 100 μm^2 scanner with a Nanosensor PPP-XYCONTR silicon cantilever. All measurements were done with normal forces in the range of 1 nN to 100 nN in ambient conditions. The force calibration was made according to the Sader method [38,39], the sensitivity of the diode was determined with force spectroscopies.

Raman spectroscopy is a frequently used technique for the quantification of the defect density in graphene. Raman microscopy measurements were performed using a WITec alpha 300 confocal Raman microscope. The wavelength of the excitation laser was 532 nm and the power of the laser was kept at 2.1 mW. The laser spot size was 360 nm and the spectral resolution 3 cm^{-1}. The Raman spectrum of graphene consists of the D and G peaks [100–103], around 1345 cm^{-1} and 1590 cm^{-1} respectively, which arise from vibrations of sp^2-hybridized carbon atoms. Hydrogenation of graphene is leading to a strong atomic buckling and results in a D to G intensity ratio of over 4 at 532 nm excitation [88,104,105]. Raman microscopy was utilized in this work to map the I(D)/I(G) ratio in order to find out the effects of the mechanical treatment on the phononic character of monolayer graphene.

The investigation with FFM showed mechanical cleaning of the pristine graphene as suggested in other studies, and confirmed the ratio of about 3 to 6 of friction force between bare SiO_2 and cleaned graphene [76, 90, 91]. Figure 4.1(a) shows a typical measurement performed on the active zone of the sample, where several observations can be made. The areas which were exposed to hydrogen plasma reveal a different friction contrast from those which were masked during the treatment. The hydrogenated surface is located at the darker spots in the friction image, corresponding to lower friction. In topography, no contrast is apparent, although the signal seems to be slightly less noisy on the hydrogenated surface. The topography shows ripples originating from the cool-down and transfer process of the sample preparation. Moreover residuals of the PMMA resist appear as highly protruding objects. A scratch-like feature with a lower height and smaller friction force is apparent, cutting the image from the bottom to the right hand side. Ripples are crossing this scratch showing that the graphene layer is still intact there. The existence of such a feature already suggests that the surface is almost entirely covered with hydrocarbon contaminants caused by the sample preparation process as well as the storage in ambient conditions. When this area is repeatedly scanned, the topography and the friction images show major changes. Figure 4.1(b) presents the 15^{th} scan, where some modifications, mainly located around the border of the hydrogenated parts, can be observed. The horizontal lines are indications of manipulation events which typically appear along the scan direction. The process of cleaning can be followed in the next images (Figs. 4.1(c)-(d)), where the trajectories of such manipulations get even more pronounced. The trajectories are seen in the topography as elevations indicating a 'tip on top' kind of manipulation [106]. The cleaned surface appears as the initial scratch presented in Fig. 4.1(a): the topography is about 2 *nm* lowered, the friction force signal becomes smooth, and the friction force reduces by a factor of around 4. Contaminants are agglomerating at the ripples and on the hydrogenated areas.

The observation that the contamination is removed faster and more efficiently on non-hydrogenated parts indicates a different absorption strength of the contaminants on the two regions of the sample. Assuming that, as recently suggested for graphite [107], the major part of the contamination are polycyclic aromatic hydrocarbons (PAHs), it is obvious that the absorption mechanisms are different on the

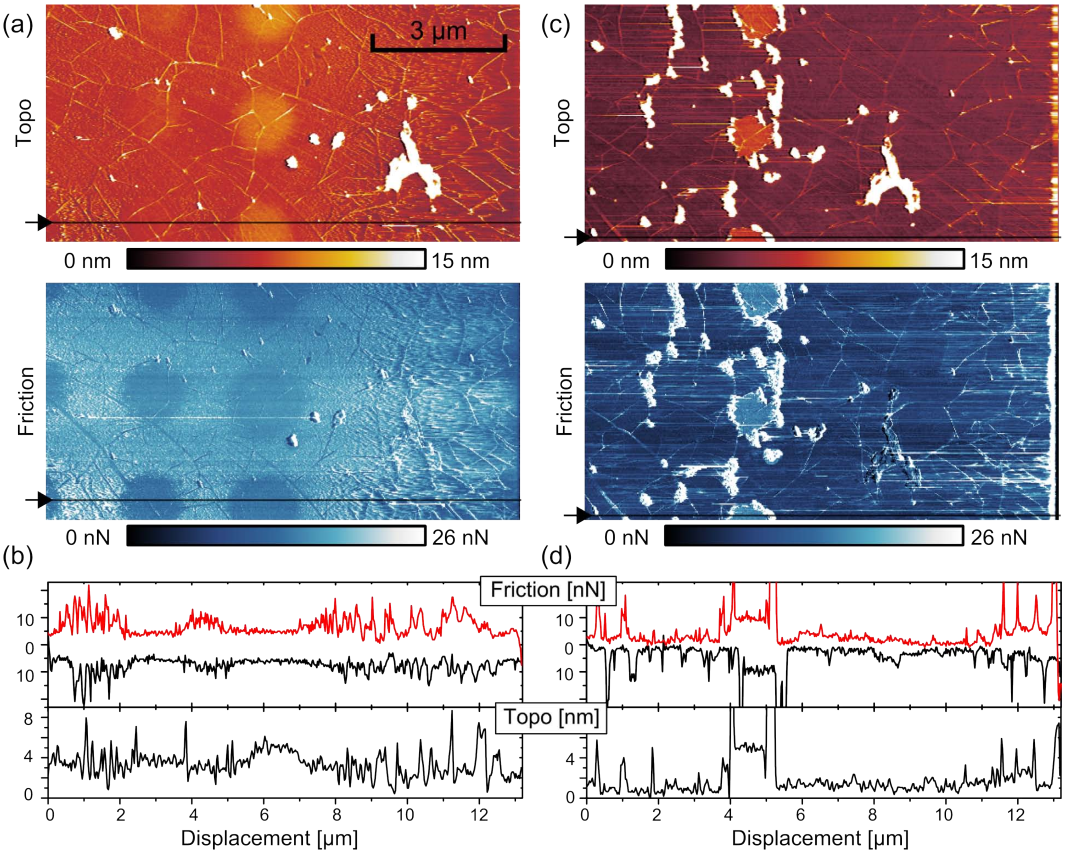

Figure 4.2. Topography (upper panel) and friction maps (lower panel) of 13.2 × 6.6 μm^2, measured with 9.1 nN load and a scan speed of 50 μm s^{-1} along the horizontal direction and starting from the bottom. (a) shows the first measurement, (c) was taken at the same position after 100 scans. The line sections (b) were extracted from the marked lines in (a), (d) from the marked lines in (c).

two materials. In the case of graphene, the aromatic rings are preferring to arrange flat lying on the surface minimizing the total energy with the π-stacking, as it is, for instance, shown for pentacene [108, 109]. Such a configuration is not possible for the hydrogenated graphene, but the hydrogen coverage of the surface probably results in stronger π-H bonding with PAHs. Another possible origin of the contamination is in connection with the sample preparation, especially the transfer process involving PMMA. It can not be ruled out that the hydrogenation is also affecting the chemical structure of the contaminants which could also explain the observations.

In Fig. 4.2(a), the measurement of the first scan at the border between the active and passive zone is shown. The contrast in the friction map is very clear. In addition to this, the last row of hydrogenated areas at the border to the passive zone is also visible in the topography and appear elevated compared to the rest of the surface, which is also noticeable in the profile of Fig. 4.2(b). The high and large contamination (PMMA) is very prominent in topography but hardly producing any contrast in the friction image. These effects become even more pronounced after most of the contamination is removed (excluding PMMA) as seen in Fig. 4.2(c). At the last row of hydrogenated areas, the hydrocarbon contamination is much more stable against

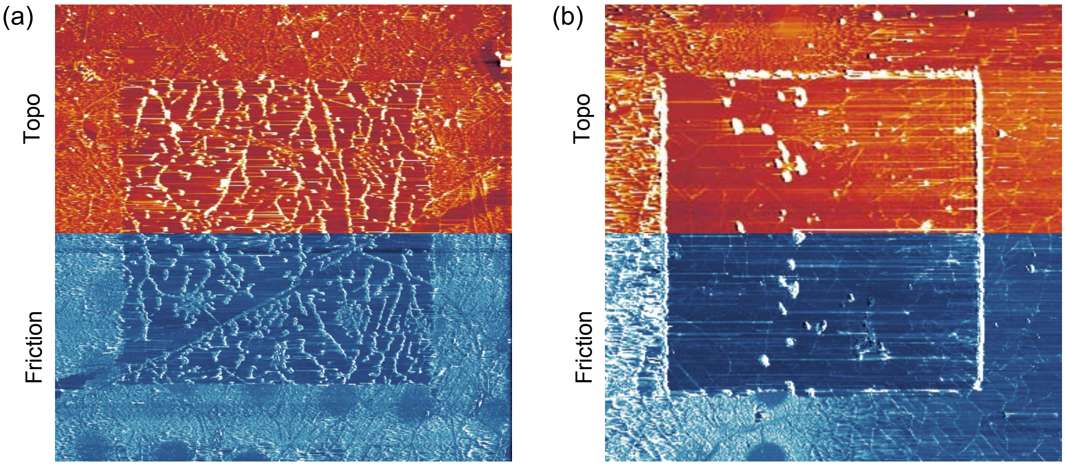

Figure 4.3. Lower magnification images of the cleaned region of Fig. 4.1 in (a) and Fig. 4.2 in (b).

the mechanical cleaning while scanning. The measurement in Fig. 4.2(c) is from the 100^{th} scan with a load of 9.1 nN. The contamination layer on the last row of hydrogenated parts is 4 *nm* high and shows no significant change in friction between the 1^{st} and 100^{th} scans (Fig. 4.2(b) and (d)), but it is 3 times higher than on the cleaned graphene surface. Dirt has agglomerated around the hydrogenated parts and piles up to 100 *nm*. Unlike the PMMA leftovers, the agglomerates show a clear contrast in the friction map.

The mechanically cleaned areas from Fig. 4.1 and 4.2 are presented with a lower magnification in Fig. 4.3. The uncompleted cleaning procedure in Fig. 4.3(a) results in the agglomeration of contaminants at the graphene ripples and on the hydrogenated parts. As the treatment continues, the contaminants are moved more and more to the border of the scan frame as suggested in the literature [90,91]. After 194 scans with 9.1 nN and 30 scans with 51.6 nN load, the surface in Fig. 4.3(b) appears fully cleaned (except for some agglomerates) and no height difference between the hydrogenated and pristine graphene is visible anymore. The agglomeration at the scan frame reaches a height of 100 nm. More surprising is the fact, that also the contrast in the friction image is lost. Raman measurements in Fig. 4.4(a) show that the hydrogenation is not affected by the treatment with the silicon tip. The same mechanical cleaning was done on the square inset, without any significant affect to the D and G peak intensities. We conclude that, in the range of our measurement sensitivity, the frictional properties of pristine and hydrogenated graphene are the same, even if their electronic and chemical properties are different.

When the sample was controlled again some weeks after the presented measurements, the cleaned spots remained clean within the resolution limit of FFM in air. Another 8 months later with the sample stored in ambient air, the same measurements were repeated in UHV with the same results and surprisingly, the cleaned spots were found to be still clean. This is a strong evidence that the contamination originate from the sample preparation and not from ambient influences.

The available data suggest that the different stability of contamination on different zones of the sample is determined by the local hydrogenation and the defect density.

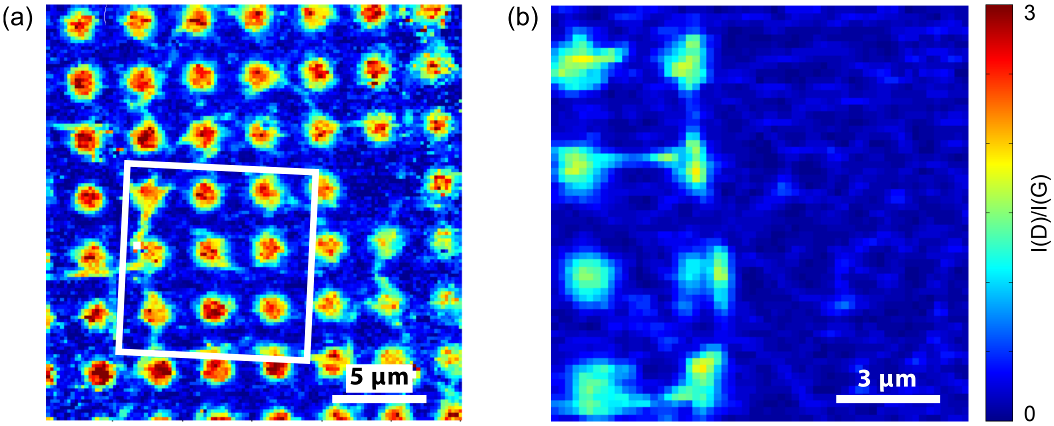

Figure 4.4. Raman images of the active zone (a) and the border between active and passive zone (b). The marked region in (a) was cleaned by means of FFM which did not change the I(D)/I(G), showing that the hydrogenation is not affected by mechanical cleaning with the silicon tip. The edge of the active zone (b) is revealing a reduced hydrogenation.

Contrary to the cleaning inside the active zone which was shown in Fig. 4.1, the contaminants stay compact on the last row of the plasma exposed graphene and shrink only from the sides. The contamination there is the most stable and two times thicker than elsewhere on the sample. The Raman spectroscopy results in Fig. 4.4(b) show a drop of I(D)/I(G) from 3 to 1.5, suggesting that there are hydrogen deficiency states which could be electrostatically more active, serving as anchor points for contaminants and, therefore, sticking to the layer strongly. The different stability on hydrogenated and non-hydrogenated graphene is obvious in the present measurements, it can be attributed to the different electrostatics of the two surfaces. Another evidence that defects are producing a more resistant contamination layer is that the contamination on the pristine graphene in the passive zone is faster removed than on the pristine graphene in the active zone, where a higher defect density in terms of hydrogen can be expected. In close proximity to the plasma (i.e. on the active zone) a minor hydrogenation in the graphene can be expected because CVD graphene is known to have many defects, which can locally be hydrogenated with atomic hydrogen, or even with the dissociation of molecular hydrogen, which are both abundant in plasma [110].

I don't mind your thinking slowly; I mind your publishing faster than you think.

WOLFGANG PAULI

Chapter 5

Conclusion and Outlook

The measurements on NaCl revealed a number of newly observed phenomena which can not be explained by the PT model when a sinusoidal potential, describing the interaction of tip and surface, is used. As an alternative to this sinusoidal potential, a potential calculated with DFT methods was introduced here which should suit the problem more adequately when the tip and surface atoms are very close. Calculated friction force maps using this DFT potential are able to reproduce the observations including the newly found characteristics, namely the distortion of the diamond shape with the nose like feature in the center, the asymmetric shape of the partial diamond in the initial sticking part, the shift of the forward and backward friction maps along the slow scan axis and as a result of it, the asymmetry of the tip path in forward and backward direction with the 5 described modes that can be observed. Therefore, these new aspects can not be regarded as a breakdown of the PT model as it was already termed [65] after the publication of first results on BNL [33]. It should, however, strongly motivate the nanotribology community to elaborate more on the potential, which is the part of the theoretical model including all relevant information of the system in relative motion. This potential is the only quantity in the PT model where quantum physical processes can be included, which is obviously playing an important role on the single asperity scale. The PT model can reproduce single asperity friction processes on NaCl if the used potential is adequately describing the interactions of the sliding system.

With the ability to precisely align the scan direction with the crystal orientation, it is possible to perform measurements where the tip is crossing many unit cells of the crystal at the same position. In the orientation along [110], the measurements revealed a reduction of friction of 27% on one ionic species compared to the other. According to the simulation, the smaller friction should be measured on the Cl sites. This ionic contrast in the [110] orientation is a material contrast, unlike in the [100] situation. Friction along [100] at a constant load was measured between 1.3 nN and

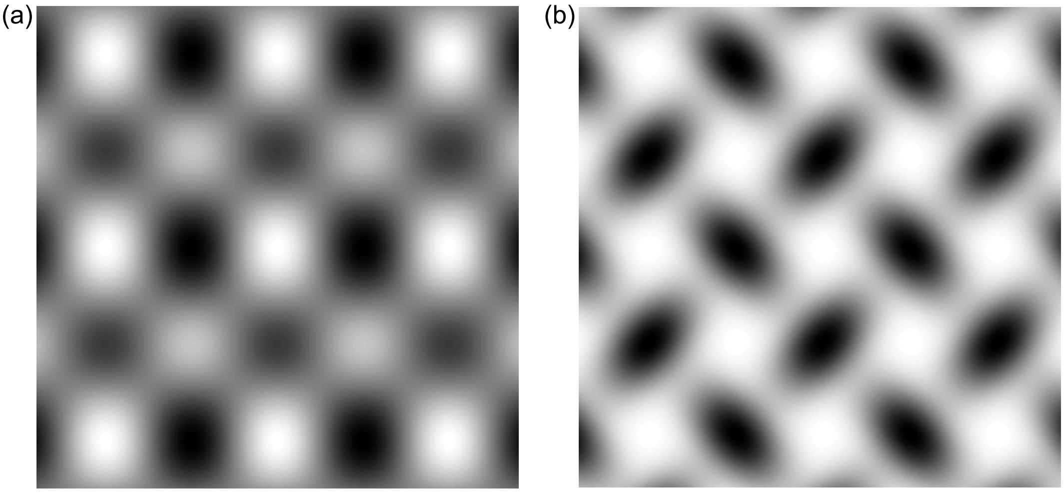

Figure 5.1. Two examples of potentials, (a) is based on sinusoidal functions described in eq. (3.6) and (b) is the result of a combination of differently shifted and weighted Gaussian functions.

1.5 nN depending on the position within a unit cell, which can be attributed to the different tip paths that are observed.

An obvious question arising at this point is concerning the influence of the tip material for the interaction with the halide surface which is a well defined and Si cluster in the simulated force maps. In the experiment, it is very likely that the relevant parts of the tip for the interaction with the surface, are fully covered with NaCl. The presented calculations with the Si tip are a more facile approach which could be extended, for example with an approach as described by *Kawai et al.* [111]. In order to investigate the origin of the contrast along [110], on one hand, the simulations should be repeated with a NaCl terminated tip, on the other hand the experiments could be compared with other surfaces, such as other halides or metals. The differences that could be measured on another salt with the same crystal geometry but a different corrugation (e.g. KBr) could be attributed to the different chemical properties, but not to the ionic nature of the surface. The contrary is the case for a metal surface or an insulating surface which is not an ionic compound offering a completely different platform in the electrostatic point of view. The electronic properties of the sliding materials can substantially influence friction, which was clearly shown by non contact friction measurements [112].

The determination of friction coefficients along various orientations was done for the measured and calculated data sets. In the measurements, large variations of μ_{kin} can be seen, the trend of a reduction towards the [110] orientation is confirmed as predicted by the simulations. For future studies, it could be useful to compare the method for the measurement of friction coefficients that was presented by *Campione et al.* [32] with the measurements done with the well established FFM methods. If the measured forces from this method can be compared with the lateral forces that are directly measured with FFM, it would in fact be much easier and more convenient to use the height profile and lateral force profile to reconstruct the force along the scan direction, which is being changed in order to get the angular dependence of friction.

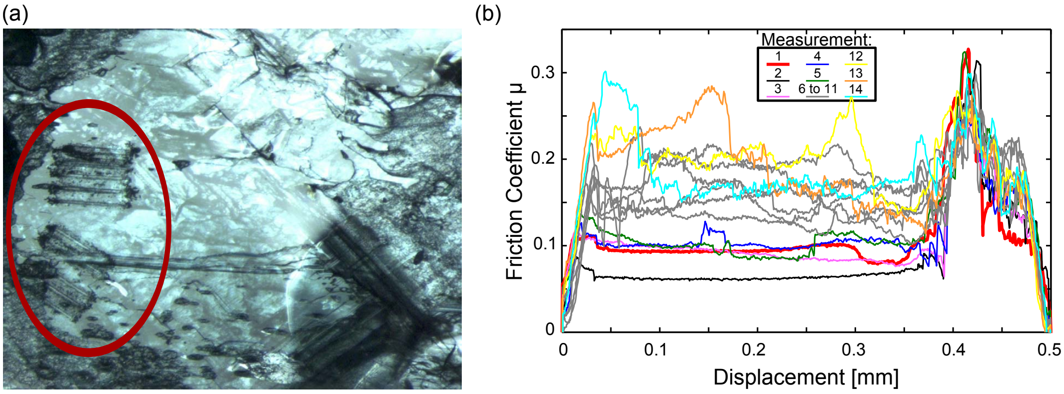

Figure 5.2. Optical microscope image (a) of the investigated BNL surface with wear tracks marked in red. (b) shows the measured friction coefficient by means of a tribometer for the first 14 cycles of scratching forth and back with a ruby ball on the same line.

The measurements on the organic surface of the BNL compound clearly show an anisotropy of friction on the molecular scale, which is manifested in the different contrasts produced by the alternating orientation of molecules in neighboring rows. Until now, the question is unanswered, to which content the interaction between tip and molecule is depending on the relative orientation of molecules and scan direction, or if it is the result of a dynamic process of the molecules being moved by the interaction with the tip. Again, the selection of an adequate potential for performing simulations is very important, and probably the only solution to get there, is the calculation of such a potential with numerical methods for the given material. On the other hand, systematic studies of different potentials could be performed to gain the knowledge, how a certain modification of the potential is influencing the friction on the single asperity scale. With such experience, it might be possible to predict frictional properties of a material or design a surface such, that the desired properties could be achieved on the atomic scale. This could be useful for a platform of NEMS as well as for nanomanipulation or even controlling diffusive processes such as the formation of self assembled monolayers (e.g. wire formation assisted by a surface with anisotropic friction). As examples for such potentials, the Fig. 5.1 shows the already discussed potential (a), and another potential (b) which could also be used to compare the results with the measurements on BNL. The potential (b) is a combination of Gaussians and was chosen because its geometrical match with the BNL surface with the benzyl heads in the upright orientation. As a first approximation, it could be assumed that the potential has such deformations.

The angle dependence of friction on BNL resembles the frictional behavior of a graphite flake which is slided over HOPG. A sharp increase of friction in the commensurate state is observed there, which could also apply for the given situation on BNL. The observed defects are a clear sign for the small contact area. If a flake of BNL is attached at the tip, it can still form a very sharp apex. It would be very interesting, to also modulate a system with such a flake for the calculation of an interaction potential, though the computational effort is probably too high. It would be desirable to extend the PT model to a multi-asperity model, but still including the accuracy of a calculated potential which is allowing atomic relaxations in the interface. The scaling of the described frictional properties with the contact size could be an interesting aspect for investigation. How small must the contact actually be in order to see the contrast of differently oriented molecules? How is the angular dependence scaling with the contact area of the sliding contact? Maybe the answers to these questions could give some new perspectives for new devices or functional surfaces. An example for an experimental approach to one of these questions can be seen in Fig. 5.2. The measurements were made with a tribometer on a BNL crystal. The problem though, was that the force sensitivity was too poor and the used cantilever too stiff to ensure a wear-less sliding over many cycles. the first measurements show a relatively small μ which increases drastically when wear sets in. A problem with the tribometer was also, that no feedback system is available, resulting in strong increase or decrease of normal force within scanned lines (see between 0.4 mm and 0.5 mm in Fig. 5.2(b)). The requirements for the sample are more demanding, the large scan paths are requiring big crystals of excellent quality. In the image from an optical microscope, the 0.5 mm long wear tracks are seen very well.

Friction measurements on graphene and hydrogenated graphene showed, as previously reported, that this very promising material suffers greatly from contamination. This is an aspect, that should be considered in all experiments that are done on graphene. The results are showing that graphene and its hydrogenated version can be cleaned mechanically by the treatment with the AFM tip. Even if the hydrogenation has a strong effect on the electronic properties of graphene, the properties as a lubricant are not degraded as far as it is measurable by means of FFM, though it can have an effect on the stability of the absorbed contamination layer. The surface contamination should not be ignored in the graphene community. Ways to clean and prevent contamination should be developed if the unique electronic properties of graphene are aimed to be explored.

Should I kill myself, or have a cup of coffee?

Albert Camus

Chapter 6

Appendix

6.1 Schemes and Plans of Electronics

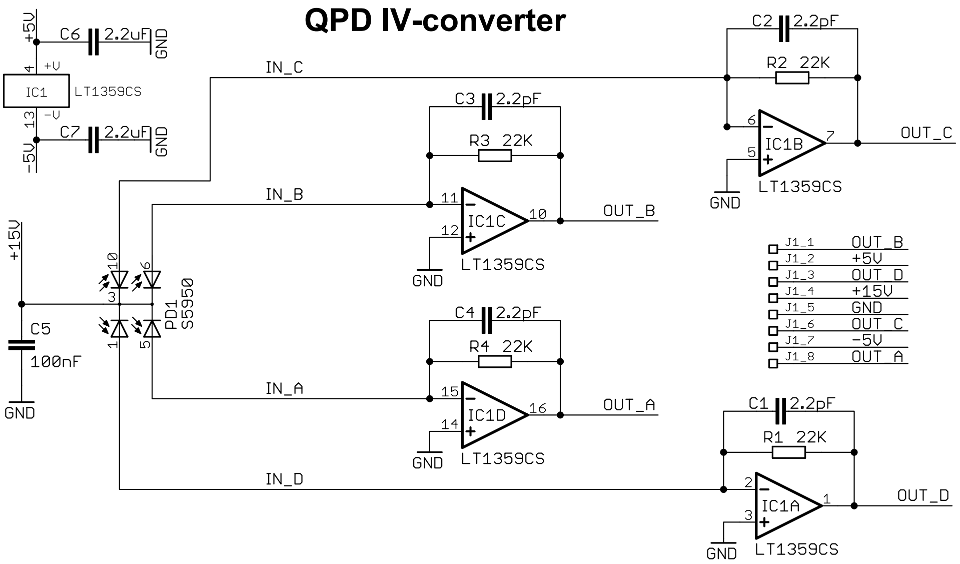

Figure 6.1. Scheme of the QPD with the amplification stage in UHV.

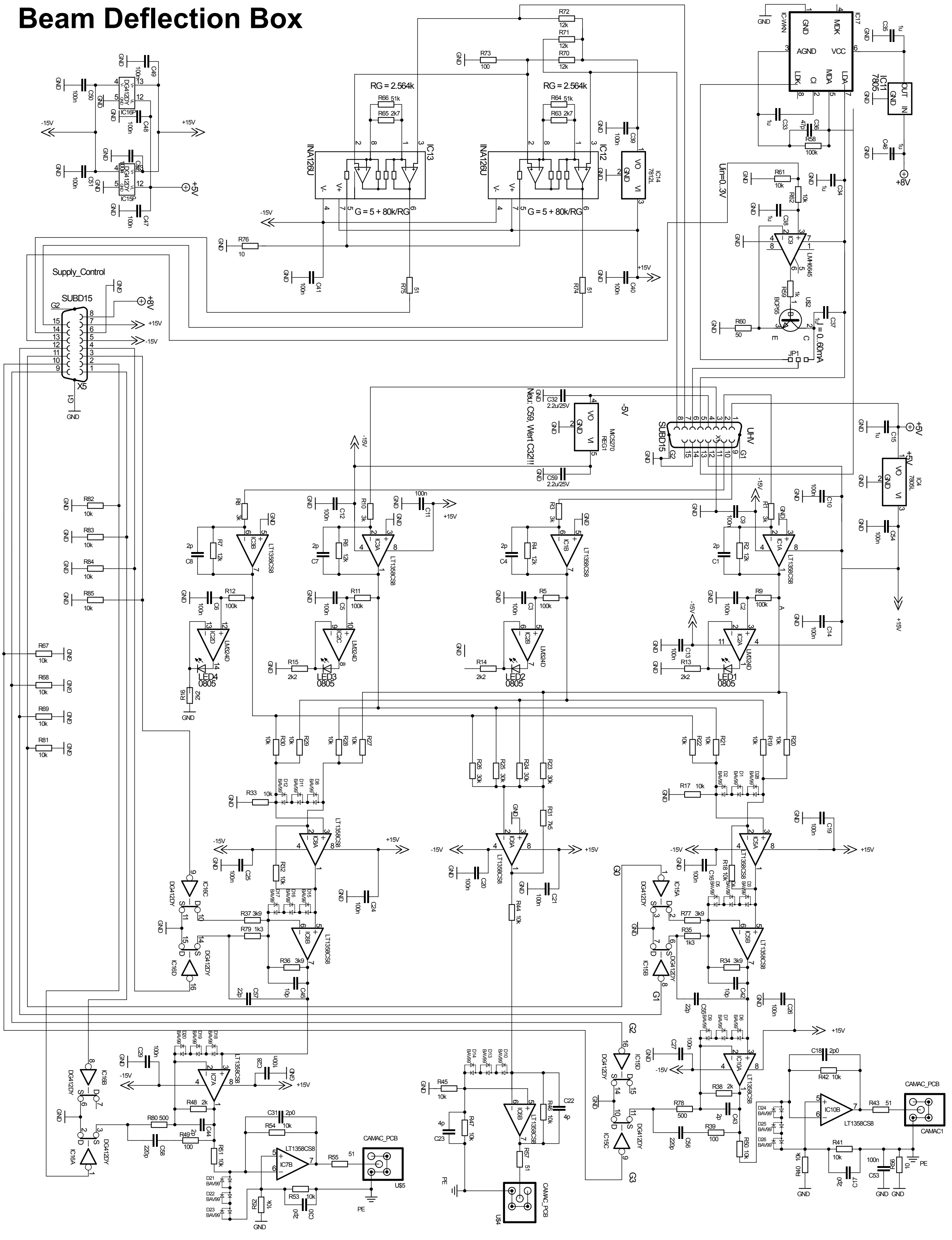

Figure 6.2. Complete scheme of the electronics at the D-Sub 15 feedthrough with the electronics for the beam deflection signal conditioning, a laser driver and the readout for two PT100 temperature sensors.

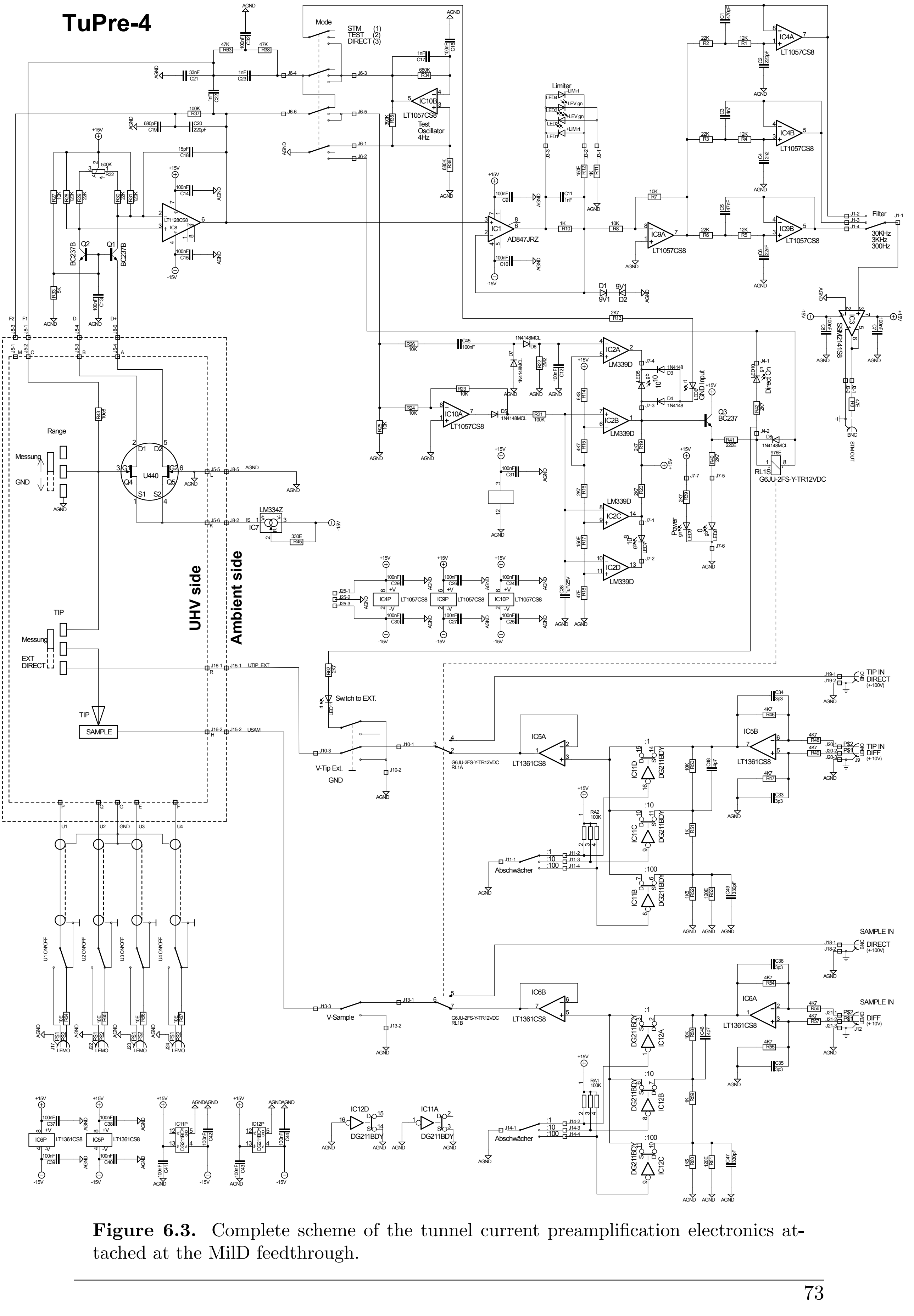

Figure 6.3. Complete scheme of the tunnel current preamplification electronics attached at the MilD feedthrough.

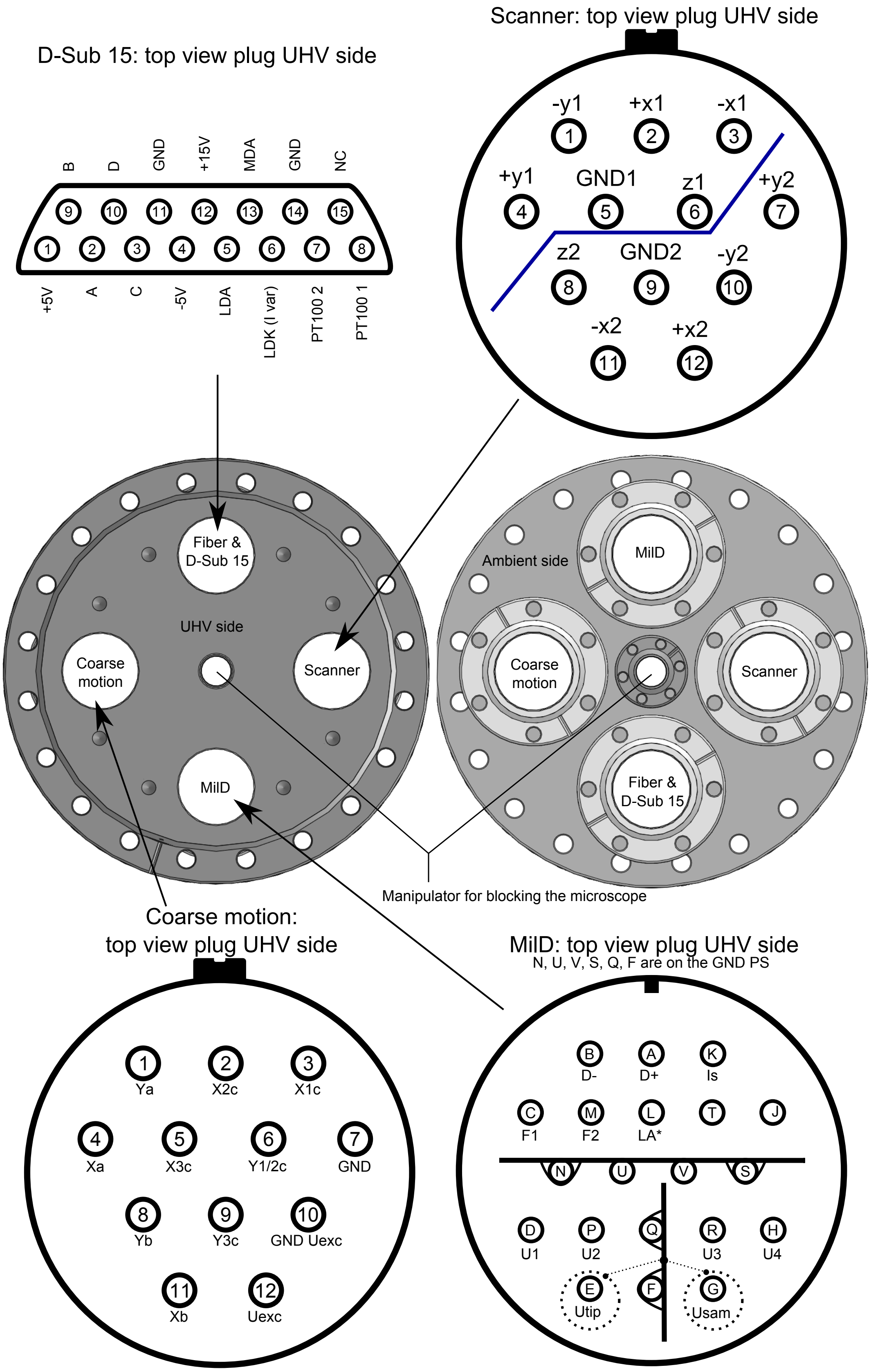

Figure 6.4. Scheme of the connectors linking the electronics with the feedthrough at the cluster flange.

Acknowledgements

First of all, I would like to thank Ernst Meyer for giving me the opportunity to work in his group. Beside the very agreeable and relaxed atmosphere you are providing within the group, it was a big pleasure for me to get the responsibility for assembling the new microscope. It was a big challenge for me, from which I could gain a lot of new knowledge and skills. This task would not have been possible to achieve without all the extremely capable persons from the workshop and electronic lab. Big thanks to Stephan Messmer who made most of the parts of the microscope, Yves Pellemont who is the master of piezo driven devices, Andreas Tonin and Roberto Maffiolini as the experts from the electronic workshop, but also all the other persons from the workshop who helped. A source of very valuable experiences for the construction of an AFM were Thilo Glatzel, Urs Gysin and Shigeki Kawai. Many discussions about various details of the system made it possible to make a device which can compete with the old microscope.

Thanks a lot also to Raphael Roth who introduced me to the field of AFM and FFM. Your work and the way of doing experiments was very inspiring. For all the help in the lab, I want to thank especially Sascha Koch and Markus Langer for always helping when some additional hands were required and Roland Steiner for always lending something if it was missing in our lab.

For the many organic crystals you provided us and many good discussions, thank you Silvio Decurtins, Tony Keene and Ivan Zimmermann. For the simulations, thanks very much to Ali Sadeghi. It was incredible how fast you always provided me the data I asked for. Thanks for the fruitful discussions with Enrico Gnecco. Thanks to Martin Dienwiebel and Diego Marchetto for the opportunity to do measurements with a tribometer.

Also big thanks to my masterstudents Matthias Wasem (It was good to have another person in the group who knows the latest weather forecast) and Mathias Schulzendorf. I was happy to see, that you both started a PhD afterwards in our group. Thanks also to Baran Eren for effectively pushing the graphene experiments, to Remy Pawlak for your nice accent and always cheering me up, Marcin Kisiel for the polish vodka, Sweetlana Fremy, Antoine Hinaut, Alexis Baratoff, Laurent Marot and all the other persons from the team for the friendly and warm atmosphere. This

made it much easier bearable to spend all the weeks locked away from the sunlight in the basement at the nanolino lab.
Last but not least, thanks for the financial support of the European Science Foundation (ESF) and the Swiss National Science Foundation (SNF).

Bibliography

[1] E. Meyer, R. Overney, K. Dransfeld, and T. Gyalog, *Nanoscience - Friction and Rheology on the Nanometer Scale*, World Scientific, 1998.

[2] B. N. J. Persson, *Sliding Friction*, Springer, 2000.

[3] C. A. Coulomb, *Mém. Math. Phys.* **161** (1785).

[4] G. Amontons, **A**, 257 (1706).

[5] F. Bowden and D. Tabor, *Oxford University Press* , 337 (1950).

[6] E. Meyer, R. Lüthi, L. Howald, M. Bammerlin, M. Guggisberg, and H.-J. Güntherodt, Site-specific friction force spectroscopy, in *J. Vac. Sci. Technol. B*, volume 14, pp. 1285–1288, AVS, 1996.

[7] U. D. Schwarz, O. Zwörner, P. Köster, and R. Wiesendanger, *Physical Review B* **56**, 6997 (1997).

[8] L. Landau and E. Lifshitz, *Theroy of Elasticity*, Elsevier, 1986.

[9] K. L. Johnson, K. Kendall, and A. D. Roberts, *Proceedings of the Royal Society of London. A. Mathematical and Physical Sciences* **324**, 301 (1971).

[10] B. Derjaguin, V. Muller, and Y. Toporov, *Journal of Colloid and Interface Science* **53**, 314 (1975).

[11] D. Maugis, *Journal of Colloid and Interface Science* **150**, 243 (1992).

[12] G. Tomlinson, *Philosophical Magazine* **7**, 905 (1929).

[13] E. Gnecco, R. Bennewitz, T. Gyalog, and E. Meyer, *Journal of Physics: Condensed Matter* **13**, R619 (2001).

[14] A. Socoliuc, R. Bennewitz, E. Gnecco, and E. Meyer, *Physical Review Letters* **92**, 134301 (2004).

[15] P. Langevin, *Les Comptes rendus de l'Académie des sciences* **146**, 530 (1908).

[16] Y. Sang, M. Dub, and M. Grant, *Physical Review B* **87**, 174301 (2001).

[17] P. Reimann and M. Evstigneev, *New Journal of Physics* **7**, 25 (2005).

[18] M. Allen and D. Tildesley, *Computer Simulations of Liquids*, Oxford Univeristy Press, 1991.

[19] D. L. Ermak and H. Buckholz, *Journal of Computational Physics* **35**, 169 (1980).

[20] M. Dienwiebel, N. Pradeep, G. S. Verhoeven, H. W. Zandbergen, and J. W. M. Frenken, *Surface Science* **576**, 197 (2005).

[21] T. Zijlstra, J. A. Heimberg, E. van der Drift, D. G. van Loon, M. Dienwiebel, L. E. M. de Groot, and J. W. M. Frenken, *Sensors and Actuators A: Physical* **84**, 18 (2000).

[22] G. Verhoeven, M. Dienwiebel, and J. Frenken, *Physical Review B* **92**, 126101 (2004).

[23] J. Y. Park, D. F. Ogletree, M. Salmeron, R. A. Ribeiro, P. C. Canfield, C. J. Jenks, and P. A. Thiel, *Science* **309**, 1354 (2005).

[24] A. E. Filippov, A. Vanossi, and M. Urbakh, *Physical Review Letters* **104**, 074302 (2010).

[25] Y. Namai and H. Shindo, *Japanese Journal of Applied Physics* **39**, 4497 (2000).

[26] P. Steiner, R. Roth, E. Gnecco, A. Baratoff, and E. Meyer, *Physical Review B* **82**, 205417 (2010).

[27] E. Gnecco, O. Y. Fajardo, C. M. Pina, and J. J. Mazo, *Tribology Letters* **48**, 33 (2012).

[28] M. Liley, D. Gourdon, D. Stamou, U. Meseth, T. M. Fischer, C. Lautz, H. Stahlberg, H. Vogel, N. A. Burnham, and C. Duschl, *Science* **280**, 273 (1998).

[29] R. Carpick, D. Sasaki, and A. Burns, *Tribology Letters* **7**, 79 (1999).

[30] M. Campione and E. Fumagalli, *Physical Review Letters* **105**, 166103 (2010).

[31] V. Kalihari, G. Haugstad, and C. D. Frisbie, *Physical Review Letters* **104**, 086102 (2010).

[32] M. Campione, S. Trabattoni, and M. Moret, *Tribology Letters* **45**, 219 (2012).

[33] G. Fessler, I. Zimmermann, T. Glatzel, E. Gnecco, P. Steiner, R. Roth, T. D. Keene, S.-X. Liu, S. Decurtins, and E. Meyer, *Applied Physics Letters* **98**, 083119 (2011).

[34] C. M. Pina, R. Miranda, and E. Gnecco, *Physical Review B* **85**, 073402 (2012).

[35] D. Sarid, *Scanning force microscopy*, Oxford University Press, 1991.

[36] M. Nonnenmacher, J. Greschner, O. Wolter, and R. Kassing, Scanning force microscopy with micromachined silicon sensors, in *J. Vac. Sci. Technol. B*, volume 9, pp. 1358–1362, Boston, Massachusetts (USA), 1991, AVS.

[37] J. Cleveland, S. Manne, D. Bocek, and P. Hansma, *Review of Scientific Instruments* **64**, 403 (1993).

[38] J. E. Sader, J. W. M. Chon, and P. Mulvaney, *Review of Scientific Instruments* **70**, 3967 (1999).

[39] C. P. Green, H. Lioe, J. P. Cleveland, R. Proksch, P. Mulvaney, and J. E. Sader, *Review of Scientific Instruments* **75**, 1988 (2004).

[40] J. E. Sader, *Journal of Applied Physics* **84**, 64 (1998).

[41] G. Binnig, H. Rohrer, C. Gerber, and E. Weibel, *Physical Review Letters* **50**, 120 (1983).

[42] http://www.specs.com/.

[43] L. Howald, E. Meyer, R. Lüthi, H. Haefke, R. Overney, H. Rudin, and H.-J. Güntherodt, *Applied Physics Letters* **63**, 117 (1993).

[44] http://www.omicron.de.

[45] S. Torbrügge, J. Lübbe, L. Troger, M. Cranney, T. Eguchi, Y. Hasegawa, and M. Reichling, *Review of Scientific Instruments* **79**, 083701 (2008).

[46] S. Maier, Y. Sang, T. Filleter, M. Grant, R. Bennewitz, E. Gnecco, and E. Meyer, *Physical Review B* **72**, 245418 (2005).

[47] P. Steiner, R. Roth, E. Gnecco, T. Glatzel, A. Baratoff, and E. Meyer, *Nanotechnology* **20**, 495701 (6pp) (2009).

[48] S. Kawai, T. Glatzel, S. Koch, B. Such, A. Baratoff, and E. Meyer, *Physical Review Letters* **103**, 220801 (2009).

[49] S. Kawai, T. Glatzel, S. Koch, A. Baratoff, and E. Meyer, *Physical Review B* **83**, 035421 (2011).

[50] S. Kawai, S. Hafizovic, T. Glatzel, A. Baratoff, and E. Meyer, *Physical Review B* **85**, 165426 (2012).

[51] S. Koch, M. Langer, S. Kawai, E. Meyer, and T. Glatzel, *Journal of Physics: Condensed Matter* **24**, 314212 (2012).

[52] A. Labuda and P. H. Grütter, *Review of Scientific Instruments* **82**, 013704 (2011).

[53] L. Howald, *Raster-Kraftmikroskopie an Silizium und Ionenkristallen im Ultrahochvakuum*, PhD thesis, Philosophisch-Naturwissenschaftliche Fakultt der Universitt Basel, 1994.

[54] L. Howald, H. Rudin, and H.-J. Güntherodt, *Review of Scientific Instruments* **63**, 3909 (1992).

[55] A. Wetzel, A. Socoliuc, E. Meyer, R. Bennewitz, E. Gnecco, and C. Gerber, *Review of Scientific Instruments* **76**, 103701 (2005).

[56] F. Mohn, L. Gross, N. Moll, and G. Meyer, *Nat Nano* **7**, 227 (2012).

[57] D. Gourdon, N. Burnham, A. Kulik, E. Dupas, F. Oulevey, G. Gremaud, D. Stamou, M. Liley, Z. Dienes, H. Vogel, and C. Duschl, *Tribology Letters* **3**, 317 (1997).

[58] R. Luthi, E. Meyer, M. Bammerlin, L. Howald, H. Haefke, T. Lehmann, C. Loppacher, H.-J. Güntherodt, T. Gyalog, and H. Thomas, Friction on the atomic scale: An ultrahigh vacuum atomic force microscopy study on ionic crystals, in *J. Vac. Sci. Technol. B*, volume 14, pp. 1280–1284, AVS, 1996.

[59] U. D. Schwarz, O. Zwrner, P. Kster, and R. Wiesendanger, *Physical Review B* **56**, 6987 (1997).

[60] A. Schirmeisen, D. Weiner, and H. Fuchs, *Physical Review Letters* **97**, 136101 (2006).

[61] L. Genovese, A. Neelov, S. Goedecker, T. Deutsch, S. A. Ghasemi, A. Willand, D. Caliste, O. Zilberberg, M. Rayson, A. Bergman, et al., *Journal of Chemical Physics* **129**, 014109 (2008).

[62] C. Hartwigsen, S. Gœdecker, and J. Hutter, *Physical Review B* **58**, 3641 (1998).

[63] M. Lantz, R. Hoffmann, A. Foster, A. Baratoff, H. Hug, H. Hidber, and H.-J. Güntherodt, *Physical Review B* **74**, 245426 (2006).

[64] P. Steiner, R. Roth, E. Gnecco, A. Baratoff, S. Maier, T. Glatzel, and E. Meyer, *Physical Review B* **79**, 045414 (2009).

[65] A. J. Weymouth, D. Meuer, P. Mutombo, T. Wutscher, M. Ondracek, P. Jelinek, and F. J. Giessibl, *Physical Review Letters* **111**, 126103 (2013).

[66] S. Decurtins, H. W. Schmalle, R. Pellaux, P. Fischer, and A. Hauser, *Mol. Cryst. Liq. Cryst. Sci. Technol., Sect. A* **305**, 227 (1997).

[67] D. R. Bloomquist, J. J. Hansen, C. P. Landee, R. D. Willett, and R. Buder, *Inorg. Chem.* **20**, 3308 (1981).

[68] T. D. Keene, I. Zimmermann, A. Neels, O. Sereda, J. Hauser, S.-X. Liu, and S. Decurtins, *Crystal Growth & Design* **10**, 1854 (2010).

[69] S. Fremy, S. Kawai, R. Pawlak, T. Glatzel, A. Baratoff, and E. Meyer, *Nanotechnology* **23**, 055401 (2012).

[70] J. E. Sader and S. P. Jarvis, *Applied Physics Letters* **84**, 1801 (2004).

[71] S. Kawai, T. Glatzel, S. Koch, B. Such, A. Baratoff, and E. Meyer, *Physical Review B* **81**, 085420 (2010).

[72] L. Gross, F. Mohn, N. Moll, P. Liljeroth, and G. Meyer, *Science* **325**, 1110 (2009).

[73] R. Pawlak, S. Kawai, S. Fremy, T. Glatzel, and E. Meyer, *Journal of Physics: Condensed Matter* **24**, 084005 (2012).

[74] M. Schulzendrof, Simulated Force Spectroscopy on Organic Layer Crystals, Master's thesis, University of Basel, 2012.

[75] N. Bhushan, *Principles and applications of tribology*, New York:Wiley, 1999.

[76] K.-S. Kim, H.-J. Lee, C. Lee, S.-K. Lee, H. Jang, J.-H. Ahn, J.-H. Kim, and H.-J. Lee, *ACS Nano* **5**, 5107 (2011).

[77] W. A. de Heer, *MRS Bulletin* **36**, 632 (2011).

[78] X. Li, W. Cai, J. An, S. Kim, J. Nah, D. Yang, R. Piner, A. Velamakanni, I. Jung, E. Tutuc, S. K. Banerjee, L. Colombo, and R. S. Ruoff, *Science* **324**, 1312 (2009).

[79] J. C. Meyer, A. K. Geim, M. I. Katsnelson, K. S. Novoselov, T. J. Booth, and S. Roth, *Nature* **446**, 60 (2007).

[80] R. R. Nair, P. Blake, A. N. Grigorenko, K. S. Novoselov, T. J. Booth, T. Stauber, N. M. R. Peres, and A. K. Geim, *Science* **320**, 1308 (2008).

[81] U. Bangert, M. Gass, R. Zan, and C. T. Pan, *Scanning transmission electron Microscopy and spectroscopy of suspended Graphene, physics and applications of graphene - experiments, S. Mikhailov (Ed.)*, ISBN: 978-953-307-217-3, InTech, doi:10.5772/14569, 2011.

[82] R. S. Pantelic, J. C. Meyer, U. Kaiser, and H. Stahlberg, *Solid State Communications* **152**, 1375 (2012).

[83] H. Park, P. R. Brown, V. Bulovic, and J. Kong, *Nano Letters* **12**, 133 (2011).

[84] C. R. Dean, A. F. Young, I. Meric, C. Lee, L. Wang, S. Sorgenfrei, K. Watanabe, T. Taniguchi, P. Kim, and K. L. S. J. Hone, *Nat Nano* **5**, 722 (2010).

[85] Z. Cheng, Q. Zhou, C. Wang, Q. Li, C. Wang, and Y. Fang, *Nano Letters* **11**, 767 (2011).

[86] A. Nourbakhsh, M. Cantoro, A. Klekachev, F. Clemente, B. Sorëe, M. H. van der Veen, T. Vosch, A. Stesmans, B. Sels, and S. De Gendt, *J. Phys. Chem. C* **114**, 6894 (2010).

[87] H. E. Romero, N. Shen, P. Joshi, H. R. Gutierrez, S. A. Tadigadapa, J. O. Sofo, and P. C. Eklund, *ACS Nano* **2**, 2037 (2008).

[88] B. Eren, T. Glatzel, M. Kisiel, W. Fu, R. Pawlak, U. Gysin, C. Nef, L. Marot, M. Calame, C. Schonenberger, and E. Meyer, *Applied Physics Letters* **102**, 071602 (2013).

[89] H. S. Song, S. L. Li, H. Miyazaki, S. Sato, K. Hayashi, A. Yamada, N. Yokoyama, and K. Tsukagoshi, *Scientific Reports* **2**, (2012).

[90] A. M. Goossens, V. E. Calado, A. Barreiro, K. Watanabe, T. Taniguchi, and L. M. K. Vandersypen, *Applied Physics Letters* **100**, 073110 (2012).

[91] N. Lindvall, A. Kalabukhov, and A. Yurgens, *Journal of Applied Physics* **111**, 064904 (2012).

[92] J. O. Sofo, A. S. Chaudhari, and G. D. Barber, *Physical Review B* **75**, 153401 (2007).

[93] W. Fu, C. Nef, O. Knopfmacher, A. Tasarov, M. Weiss, M. Calame, and C. Schönenberger, *Nano Letters* **11**, 3597 (2011).

[94] Y. G. Zhou, X. T. Zu, F. Gao, J. L. Nie, and H. Y. Xiao, *Journal of Applied Physics* **105**, 014309 (2009).

[95] J. Bohdansky, J. Roth, and H. L. Bay, *Journal of Applied Physics* **51**, 2861 (1980).

[96] B. Eren, D. Hug, L. Marot, R. Pawlak, M. Kisiel, R. Steiner, D. M. Zumbühl, and E. Meyer, *Beilstein Journal of Nanotechnology* **3**, 852 (2012).

[97] T. Filleter, J. L. McChesney, A. Bostwick, E. Rotenberg, K. V. Emtsev, T. Seyller, K. Horn, and R. Bennewitz, *Physical Review Letters* **102**, 086102 (2009).

[98] C. Lee, Q. Li, W. Kalb, X.-Z. Liu, H. Berger, R. W. Carpick, and J. Hone, *Science* **328**, 76 (2010).

[99] X. Feng, S. Kwon, J. Y. Park, and M. Salmeron, *ACS Nano* **7**, 1718 (2013).

[100] F. Tuinstra and J. L. Koenig, *Journal of Chemical Physics* **53**, 1126 (1970).

[101] A. C. Ferrari and J. Robertson, *Physical Review B* **61**, 14095 (2000).

[102] A. C. Ferrari, J. C. Meyer, V. Scardaci, C. Casiraghi, M. Lazzeri, F. Mauri, S. Piscanec, D. Jiang, K. S. Novoselov, S. Roth, and A. K. Geim, *Physical Review Letters* **97**, 187401 (2006).

[103] A. C. Ferrari, *Solid State Communications* **143**, 47 (2007).

[104] Y. Wang, X. Xu, J. Lu, M. Lin, Q. Bao, B. Özyilmaz, and K. P. Loh, *ACS Nano* **4**, 6146 (2010).

[105] Z. Luo, T. Yu, Z. Ni, S. Lim, H. Hu, J. Shang, L. Liu, Z. Shen, and J. Lin, *J. Phys. Chem. C* **115**, 1422 (2011).

[106] D. Dietzel, M. Feldmann, C. Herding, U. Schwarz, and A. Schirmeisen, *Tribology Letters* **39**, 273 (2010).

[107] D. Martinez-Martin, R. Longuinhos, J. G. Izquierdo, A. Marele, S. S. Alexandre, M. Jaafar, J. M. Gomez-Rodriguez, L. Bañares, J. M. Soler, and J. Gomez-Herrero, *Carbon* **61**, 33 (2013).

[108] W. H. Lee, J. Park, S. H. Sim, S. Lim, K. S. Kim, B. H. Hong, and K. Cho, *J. Am. Chem. Soc.* **133**, 4447 (2011).

[109] J. Götzen, D. Käfer, C. Wöll, and G. Witte, *Physical Review B* **81**, 085440 (2010).

[110] B. H. Kim, S. J. Hong, S. J. Baek, H. Y. Jeong, N. Park, M. Lee, S. W. Lee, M. Park, S. W. Chu, H. S. Shin, J. Lim, J. C. Lee, Y. Jun, and Y. W. Park, *Scientific Reports* **2**, (2012).

[111] S. Kawai, F. F. Canova, T. Glatzel, A. S. Foster, and E. Meyer, *Phys. Rev. B* **84**, 115415 (2011).

[112] M. Kisiel, E. Gnecco, U. Gysin, L. Marot, S. Rast, and E. Meyer, *Nat Mater* **10**, 119 (2011).

List of Publications

1. G. Fessler, I. Zimmermann, P. Steiner, E. Gnecco, T. Glatzel, T. D. Keene, S. Liu, S. Decurtins, and E. Meyer *Orientation dependent molecular friction on organic layer compound crystals*, Applied Physics Letters, **98**, 083119, (2011).
2. S. Kawai, C. M. Pina, A. Bubendorf, G. Fessler, T. Glatzel, E. Gnecco, E. Meyer *Systematic study of the dolomite (104) surface by bimodal dynamic force microscopy in ultra-high vacuum*, Nanotechnology, **24**, 055702, (2013).
3. G.Fessler, B. Eren, T. Glatzel, E. Meyer *Friction force microscopy studies on* SiO_2 *supported pristine and hydrogenated graphene,* submitted to Applied Physics Letters, (2013)